SISTEMA UNIVERSITARIO ESTATAL SUE CARIBE
UNIVERSIDAD DE CARTAGENA
MAESTRÍA EN CIENCIAS FÍSICAS

# STRUCTURAL OPTIMIZATION IN ATOMIC SYSTEMS WITH FEW DEGREES OF FREEDOM

**Beatriz Helena Cogollo Olivo**

| Thesis submitted for the degree of Master in Physical Sciences | Advisor<br>Javier Antonio Montoya Martínez, Ph. D. |
|---|---|

Cartagena de Indias, D. T. y C.
2014

MAESTRÍA EN CIENCIAS FÍSICAS

Universidad
de Cartagena
Fundada en 1827

# STRUCTURAL OPTIMIZATION IN ATOMIC SYSTEMS WITH FEW DEGREES OF FREEDOM

**BEATRIZ HELENA COGOLLO OLIVO**

**UNIVERSITY OF CARTAGENA**
**MASTER IN PHYSICAL SCIENCES SUE – CARIBE**
**CARTAGENA DE INDIAS, D. T. Y C.**
**COLOMBIA**
**2014**

MAESTRÍA EN CIENCIAS FÍSICAS

Universidad
de Cartagena
Fundada en 1827

# STRUCTURAL OPTIMIZATION IN ATOMIC SYSTEMS WITH FEW DEGREES OF FREEDOM

Thesis submitted for the degree of Master in Physical Sciences

**BEATRIZ HELENA COGOLLO OLIVO**

**ADVISOR**
**Javier Antonio Montoya Martínez, Ph.D.**

**UNIVERSITY OF CARTAGENA**
**MASTER IN PHYSICAL SCIENCES SUE-CARIBE**
**CARTAGENA DE INDIAS, D. T. Y C.**
**COLOMBIA**
**2014**

Cartagena de Indias, 9 de Diciembre de 2014

Señores Miembros
**Comité Curricular de la Maestría en Ciencias Físicas**
SUE Caribe

Estimados Señores Miembros del Comité,

Tengo el agrado de dirigirme a ustedes a fin de solicitarles sea evaluada el Trabajo de Grado de Maestría, titulada **"STRUCTURAL OPTIMIZATION IN ATOMIC SYSTEMS WITH FEW DEGREES OF FREEDOM"**, de la cual adjunto dos (2) copias impresas y una (1) en formato electrónico CD.

Saluda a ustedes, muy atentamente.

**BEATRIZ HELENA COGOLLO OLIVO**

Estudiante
Programa de Maestría en Ciencias Físicas
SUE- Caribe

Visto Bueno:

**JAVIER ANTONIO MONTOYA MARTÍNEZ**
Docente – Facultad de Ciencias Exactas y Naturales
Universidad de Cartagena

Visto Bueno:

**LUIS EDUARDO CORTÉS RODRÍGUEZ**
Coordinador Institucional
Maestría en Ciencias Físicas
Universidad de Cartagena

# AKNOWLEDGEMENTS

This is one more step of a journey called life. Today I'm writing these lines because several people believed and supported me and this work is for them.

First, I want to thank deeply my advisor, Prof. Javier Montoya. He's the reason for me to be here, growing not only as a scientist but also as a person. I'm completely grateful to him for encouraging me to pursue a path of excellence and I'm very proud to count on him not only as a tutor, but also as a friend and role model.

I was, and still am, very lucky to have such a supportive family: Morales, mom, dad and "Pre", thanks a lot for all your efforts! Thank you for being there and for supporting me in this new path, even when some of you don't have a very clear idea of why the world needs physicists.

Thanks to my dearest friend Melisa, we were able to contemplate and enjoy the beauty of nature, and she made me realize every time we talked about what I was doing, that I finally found my passion. Through my words she saw a glimpse of the marvelous of our universe and I fell in love with science again and again.

And finally to all those that I haven't mention, professors and research group colleagues, I'm sure that your ideas, comments or discussions at some point of this M. Sc. program helped me to reach to this point, thank you all.

Beatriz
December, 2014

*“(…) take the point of a pencil and magnify it. One reaches the point where a stunning realization strikes home: The pencil is not solid; it is composed of atoms which whirl and revolve like a trillion demon planets. What seems solid to us is actually only a loose net held together by gravitation.”*

*Stephen King.*
*The Dark Tower Series – Book 1: The Gunslinger*

# CONTENTS

p.

List of Tables i

List of Figures ii

List of Annexes v

**Abstract** vi

**CHAPTER 1: THEORETICAL FOUNDATION**

CRYSTAL STRUCTURE PREDICTION PROBLEM 1

METHODS OF CRYSTAL STRUCTURE PREDICTION 4

- Random Sampling 6
- Simulated Annealing 7
- Molecular Dynamics 8
- Metadynamics 10
- Evolutionary Algorithms 11

THE ELECTRONIC PROBLEM 12

- Born – Oppenheimer Approximation 13
- Hartree and Hartree – Fock Approximations 15
- Thomas – Fermi Theory 19
- Hohenberg – Kohn Theorems 21
- Kohn – Sham Method 24
- Exchange and Correlation in DFT 27
  - *Local Density Approximation – LDA* 28
  - *Generalized Gradient Approximation – GGA* 29
- Pseudopotentials and Basis Sets 31
  - *Pseudopotentials* 32
  - *Basis Sets* 34

REFERENCES 35

**CHAPTER 2: STUDY CASE: SOLID OXYGEN AT HIGH PRESSURE**

STATE OF THE ART 41
    Phases of solid oxygen in equilibrium with vapor 42
    High – pressure phases of solid oxygen 43
METHODOLOGY 47
TECHNICAL DETAILS 48
RESULTS 51
    Molecular Solid Oxygen 51
    Monoatomic Oxygen (Special Case) 64
DISCUSSION AND CONCLUSIONS 66
REFERENCES 69

**CHAPTER 3: STUDY CASE: COPPER CLUSTERS IN VACUUM**

OVERVIEW ON CLUSTERS 74
TRANSITION METAL CLUSTERS 75
    Shell effects and magic numbers 75
    Clusters Band Gap 76
STATE OF THE ART 77
    Isomers 78
METHDOLOGY 81
TECHNICAL DETAILS 82
RESULTS 84
DISCUSSION AND CONCLUSIONS 89
    Geometry of ground state and isomers structures 89
    Binding Energies 90
    HOMO – LUMO Gap 92
REFERENCES 93

**Closing Remarks** 97

**APPENDIX A. DIRAC'S NOTATION AND SECOND QUANTIZATION** 99

# LIST OF TABLES

p.

Table 1.1. Microscopic properties of crystal materials. 2

Table 1.2. Several algorithms used in Molecular Dynamics. 9

Table 1.3. Expressions used to calculate the exchange-correlation energy in LDA. 29

Table 1.4. Summary of several GGA functionals. 31

Table 2.1. Parameters used in the Quantum ESPRESSO input files for oxygen structural search. 50

Table 2.2. $O_2$ structures that converged into a local minima. 52

Table 2.3. $O_4$ structures that converged into a local minima. 53

Table 2.4. Cell parameters for equivalent structures for $O_2$ at pressures from 0.35 to 3.5 TPa. 54

Table 2.4. Cell parameters for equivalent structures for $O_2$ at pressures from 0.35 to 3.5 TPa. (Cont.) 55

Table 2.5. Cell parameters for equivalent structures for $O_4$ at pressures from 0.5 to 3.5 TPa. 55

Table 2.5. Cell parameters for equivalent structures for O4 at pressures from 0.5 to 3.5 TPa. (Cont.) 56

Table 2.5. Enthalpy values for several monoatomic oxygen structures from 1TPa to 8TPa. 61

Table 3.1 Classification of clusters according to size. N is the number of atoms, D is the diameter (for a cluster of sodium atoms) and $F_S$ is the fraction of surface atoms. 74

Table 3.2. Symmetry group of Cun clusters (n = 3 – 7) 79

Table 3.2. Symmetry group of Cun clusters (n = 3 – 7). (Cont.) 80

Table 3.3. Binding energy in [eV/atom] of Cun clusters (n = 3 – 7). 81

Table 3.4. Parameters used in the Quantum ESPRESSO input files for copper clusters structural search. 84

Table 3.5. Binding energy (BE) and difference in binding energy (ΔE) of ground state an isomers of Cun (n = 3 – 7). 89

# LIST OF FIGURES

p.

Figure 1.1. Proposed methods for solving the crystal structure prediction problem. 4

Figure 1.2. Energy landscape. It contains kinetics traps and energy barrels. 6

Figure 1.3. Simplified version of a Random Sampling algorithm. 7

Figure 1.4. Schematic representation of simulated annealing. 8

Figure 1.5. Particle trajectory in Molecular Dynamics simulation. 9

Figure 1.6. Schematic representation of the progressive filling of the underlying potential (thick line) by means of the Gaussians deposited along the trajectory. The sum of the underlying potential and of the metadynamics bias is shown at different times (thin lines). 11

Figure 1.7. Self-Consistent Field (SCF) algorithm. 18

Figure 1.8. The Fermi sphere with an infinitesimal volume of d$\mathbf{p}^3$ in the real space, or $(2\pi/L)^3$ in the K-space. 19

Figure 1.9. Schematic representation of Hohenberg-Kohn Theorem. 21

Figure 1.10. Schematic illustration of all-electron (solid lines) and pseudoelectron (dashed lines) potentials and their corresponding wave functions. The radius at which all-electron and pseudoelectron values match is designated $r_c$. 33

Figure 1.11. Flow chart describing the construction of an ionic pseudopotential for an atom. 34

Figure 2.1. Phase diagram of solid oxygen. 42

Figure 2.2. Structure of solid oxygen at a) $\alpha$-phase; $\beta$-phase in b-i) rhombohedral axes and b-ii) monoclinic axes; c) $\gamma$-phase, where circles represent the orientational disorder of the molecules. 43

Figure 2.3. Structure of $\delta$-oxygen. 43

Figure 2.4. A possible arrangement of molecules at the bc face of the A2/m unit cell of $\varepsilon$-$O_2$. 44

Figure 2.5. Proposed structural model of $\varepsilon$-$O_2$ at 11.4 GPa viewed along a) the c and b) the b axes. 45

Figure 2.6. Proposed new phase diagram of oxygen. 46

Figure 2.7. Energy convergence for an $O_2$ structure at 3500GPa. Varying a) k-points grid and b) plane wave kinetic cutoff. 49

Figure 2.8. Energy convergence for an $O_4$ structure at 3500GPa. Varying a) k-points grid and b) plane wave kinetic cutoff. 50

Figure 2.9. Enthalpy variation for $O_2$ at pressures from 0.35 to 3.5 TPa. For each pressure, the circle size is proportional to the number of initial structures that converged to the marked enthalpy. 52

Figure 2.10. Enthalpy variation for $O_4$ at pressures from 0.5 to 3.5 TPa. For each pressure, the circle size is proportional to the number of initial structures that converged to the marked enthalpy. 53

Figure 2.11. Equivalent structures for $O_2$ at pressures from 0.35 to 3.5 TPa. 56

Figure 2.11. Equivalent structures for $O_2$ at pressures from 0.35 to 3.5 TPa. (Cont.) 57

Figure 2.11. Equivalent structures for $O_2$ at pressures from 0.35 to 3.5 TPa. (Cont.) 58

Figure 2.11. Equivalent structures for $O_2$ at pressures from 0.35 to 3.5 TPa. (Cont.) 59

Figure 2.12. Equivalent structures for $O_4$ at pressures from 0.5 to 3.5 TPa. 59

Figure 2.12. Equivalent structures for $O_4$ at pressures from 0.5 to 3.5 TPa. (Cont.) 60

Figure 2.12. Equivalent structures for $O_4$ at pressures from 0.5 to 3.5 TPa. (Cont.) 61

Figure 2.13. Volume evolution while pressure increases. a) $O_2$ system. b) $O_4$ system. 62

Figure 2.14. Evolution of first (blue), second (orange) and third (green) neighbors distances while pressure increases. a) $O_2$ system structures: P-1 (triangles), C2/m (squares) and Cmcm (circles). b) $O_4$ system structures: Cmma (rhombus) and Cmcm (circles). 63

Figure 2.15. Enthalpy difference for several monoatomic oxygen structures from 1TPa to 8 TPa. Fmmm structure is the reference. 65

Figure 2.16. Zigzag chains for a) $O_2$ and b) $O_4$. 66

Figure 2.17. Enthalpy per atom of the most stables structures of $O_2$ and $O_4$ systems from 0.35 to 1.50 TPa. The symmetry groups are labeled as: Cmma (squares), P-1 (rhombus), C2-m (triangles), and Cmcm (circles). 67

Figure 2.18. Layered structure for a) $O_2$ and b) $O_4$. 68

Figure 3.1. Schematic comparison between band gaps of different sizes of copper clusters (blue tones) and several semiconductors (orange bars). 76

Figure 3.2. Total energy convergence for a $Cu_3$ cluster. Varying a) k-points grid, b) plane wave kinetic cutoff and c) cubic unit-cell edge length. 83

Figure 3.3. Energy evolution of: a) $Cu_3$ (red line), b) $Cu_4$ (blue line). For each size, the first region is the ground state structure, and the subsequent represent a cluster isomer. 85

Figure 3.3. Energy evolution of: c) $Cu_5$ (orange line), d) $Cu_6$ (green line. For each size, the first region is the ground state structure, and the subsequent represent a cluster isomer. (Cont.) 86

Figure 3.3. Energy evolution of: e) $Cu_7$ (yellow line). For each size, the first region is the ground state structure, and the subsequent represent a cluster isomer. (Cont.) 87

Figure 3.4. Structures found for $Cu_3$, $Cu_4$, $Cu_5$, $Cu_6$ and $Cu_7$. 88

Figure 3.5. Comparison of binding energy per atom as a function of cluster size, among: our results using DF-GGA (red), DF-LDA [23] (blue), TB [25] (green), Real Space Pseudopotential [27] (yellow), MD [28] (orange) and two CID experiments [21] [22] (dashed lines grey and violet). 91

Figure 3.6. Evolution of the highest occupied – lowest occupied (HOMO – LUMO) gap energy as the cluster size increases. 92

# LIST OF APPENDIXES

p.
Appendix A. Dirac’s Notation and Second Quatization 99

# Chapter 1

## THEORETICAL FOUNDATION

### CRYSTAL STRUCTURE PREDICTION PROBLEM

The crystal structure prediction (CSP) is a problem that has attracted the scientific community's attention since the establishment of the first set of Pauling's Rules in 1929. This problem can be resumed as follows: given only the chemical composition of any material there exist an infinite amount of atomic arrangements that can be obtained, each one of them with a certain total energy inside the configurational energy landscape. Therefore, the crystal structure prediction problem consists in finding, for some external conditions, e.g. a given applied pressure and/or temperature, the most stable structure i.e. the one with the lowest free energy, starting only from the knowledge of the chemical composition of the system [1].

Almost sixty years later, in 1988, there were very few advances for the solution of this problem; the famous editorial by John Maddox [2] resumes the situation at that time:

> *"One of the continuing scandals in the physical sciences is that it remains in general impossible to predict the structure of even the simplest crystalline solids from a knowledge of their chemical composition"*

Then, it is natural to ask ourselves why it is so important to determine the crystal structure of a crystalline system. The answer is quite simple: the crystal structure is perhaps the most important source of information of a material, something like its DNA, because with it we can determine directly or indirectly almost all the physical properties of that material, and this is true even if that material has not yet been synthesized! Some useful microscopic properties of crystalline materials are displayed in table 1.1.

**Table 1.1.** Microscopic properties of crystal materials. Taken from [**3**].

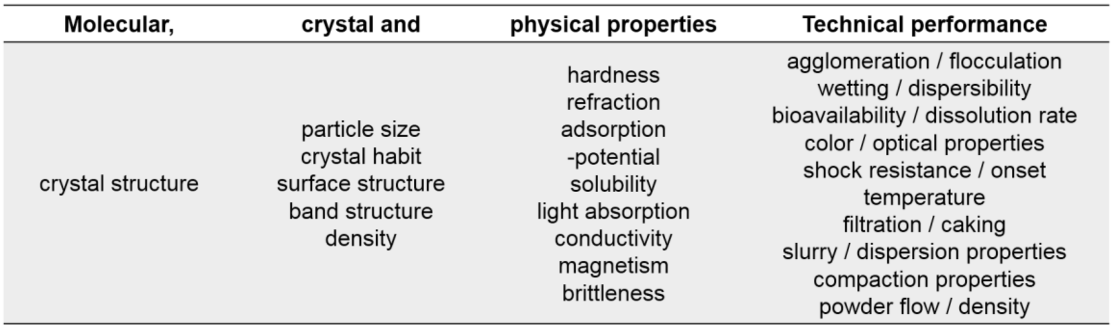

| Molecular, | crystal and | physical properties | Technical performance |
|---|---|---|---|
| crystal structure | particle size<br>crystal habit<br>surface structure<br>band structure<br>density | hardness<br>refraction<br>adsorption<br>-potential<br>solubility<br>light absorption<br>conductivity<br>magnetism<br>brittleness | agglomeration / flocculation<br>wetting / dispersibility<br>bioavailability / dissolution rate<br>color / optical properties<br>shock resistance / onset temperature<br>filtration / caking<br>slurry / dispersion properties<br>compaction properties<br>powder flow / density |

The calculation of crystal structures of solids from first principles, is a problem yet to be solved. Even if sometimes it is possible to have access to experimental data to determine the structure of a certain material, there are some major issues that need to be taken into account [4]:

- Theoretical predictions constitute a very helpful aid to experiments when the studied samples are very small or when a clear understanding of the microscopic mechanisms is desired, e. g. Diamond Anvil Cell (DAC) experiments.
- Theoretical calculations are currently the only way to study matter at conditions that are not available in laboratories, such as ultra-high pressures.
- A reliable crystal structure prediction method can deeply transform the chemical industry, in areas such as pharmaceuticals development and catalysis, and also can lower some costs associated with the research of new chemical compounds.

Now, the task of finding the structure with the lowest energy, and therefore the most stable, is an overwhelming quest [4] [5]:

The search space in these systems is multidimensional and depends on the amount of atoms per unit cell, according to:

$$d = 6 + 3(N - 1) \qquad (1)$$

In detail, it contains the information of the six lattice parameters of the crystal cell and the three spatial coordinates for each of the ***N*** atoms contained in the unit cell, assuming that one of them is fixed at the origin of coordinates (hence the "$N-1$" correction).

The number of possible locally stable structures also depends on the number of atoms per unit cell. In principle, that number is infinite, but as an approximation we could start defining a cubic cell with volume ***V*** and a discretization parameter $\boldsymbol{\delta}$, so that the ***N*** atoms can only be placed in well-defined positions, then an estimation of possible atomic configurations leads to:

$$C = \frac{1}{\left(V/_{\delta^3}\right)} \frac{\left(V/_{\delta^3}\right)!}{\left[\left(V/_{\delta^3}\right) - N\right]!\,N!} \qquad (2)$$

For the sake of illustrating the consequences of this, if we had $\delta$=1Å and V=10Å$^3$, the possible structures for a system of 10 atoms would be $10^{11}$; $10^{25}$ for a system of 20 atoms; and $10^{39}$ for a system of 30 atoms. It is an enormous amount of different possibilities to explore, and it is almost impossible to deal with all of them even for small systems.

Finding the global energy minima is a tough process, because it is extremely sensitive to the small changes that occur in the atomic distances and angles. As a result, the energy landscape of the system is rough with several peaks and valleys that produce the local energy minima and in consequence, metastable structures.

Finally, one would like to use total energy calculations with ab-initio accuracy, in order to be able to compare different competing structures with some reliability, but this requires an enormous amount of computational resources. Continuing with the previous example, the estimated CPU time would be 1000 years for a system of 10 atoms; $10^{17}$ years for a system of 20 atoms; and $10^{31}$ years for a system of 30 atoms.

It is clear that calculating the energy for every possible structural configuration is an impossible task[1]. So the first step is to develop a strategy in order to overcome the difficulties shown here.

---

[1] The age of the Universe is set up in approximately 1.38 x $10^{10}$ years.

## METHODS OF CRYSTAL STRUCTURE PREDICTION

Several approaches have been proposed to attack and solve this problem, and they are gathered in figure 1.1. Early in the previous century, the first attempts tried to relate the underlying chemistry of the materials with the modern physical theories, such as Quantum Mechanics. For example, the amount of experimental results from x-ray diffraction, diffraction of electron waves, the interpretation of band spectra, Raman spectra, among others; and the model of chemical bonding proposed by Gilbert N. Lewis in 1916 [6], were the inspiration for Linus Pauling to propose, in 1929, the first set of rules [7] that described the structure of inorganic compounds.

A similar approach was The Bond Valence Model [8] [9], developed mostly by I. David Brown. This was an advance in Pauling's rules. With the inclusion of new rules in this model, many properties of the inorganic compounds, such as bond length and coordination number, were finally understood.

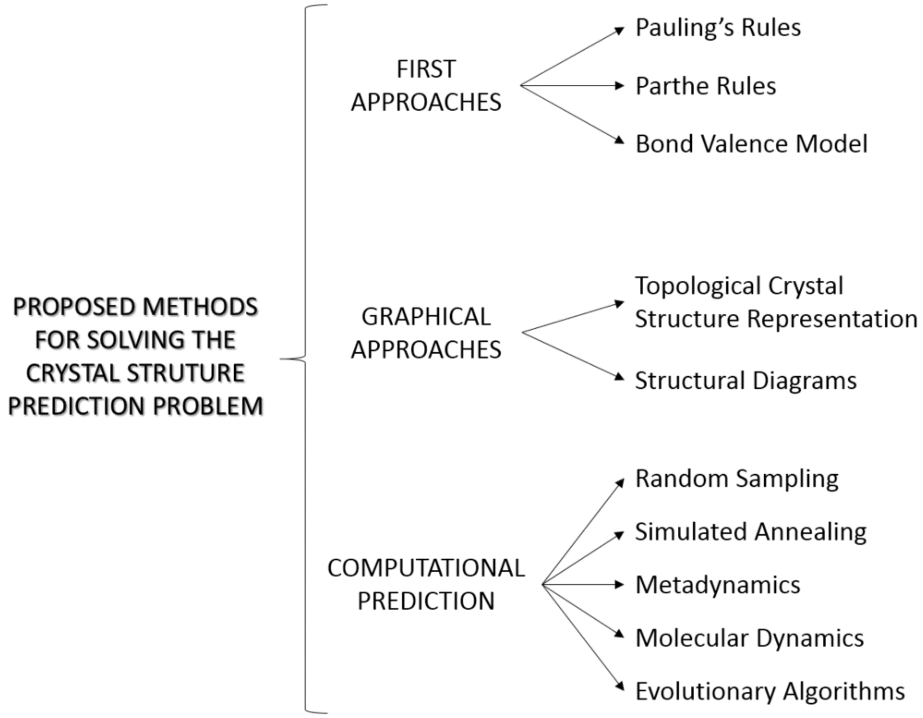
PROPOSED METHODS FOR SOLVING THE CRYSTAL STRUTURE PREDICTION PROBLEM
FIRST APPROACHES
Pauling's Rules
Parthe Rules
Bond Valence Model
GRAPHICAL APPROACHES
Topological Crystal Structure Representation
Structural Diagrams
COMPUTATIONAL PREDICTION
Random Sampling
Simulated Annealing
Metadynamics
Molecular Dynamics
Evolutionary Algorithms

**Figure 1.1.** Proposed methods for solving the crystal structure prediction problem.

Topological approaches are based on a priori chemical knowledge of the system and its symmetry. This method was developed at the beginning by Wells [10] [11] [12] [13] and it is still used to define networks that correspond to real or hypothetical crystal structures. However, selecting the most reasonable crystal structure among all the possible topologies, which depends strongly on the interatomic interaction considered and the structure groups taken into account, is not easy. Using the concept of *topological crystal structure representation*, it is possible to consider all possible topologies and subsequently reach to those that might correspond to the given crystal structure. The analysis starts from a complete representation of the crystal structure, where all atoms and all possible interatomic interactions, even the weakest, are considered as nodes and edges on a graph, respectively. It is assumed that this representation contains all the information on the crystal. For a particular system, a three-step method for simplification is proposed to reach the desired *partial* representation [14].

Although the above methods have proven their usefulness and are still used, in one way or another, their use is conditioned to a previous knowledge of the system symmetry and empirical results. In order to obtain more unbiased results in the prediction of crystal structures, the ab-initio computational approach has been fundamental, essentially because of the following two reasons among others [1]:

- The computational approach allows to calculate explicitly the physical quantity desired (e. g. the energy)
- Given the fact that no empirical information is used, the searching techniques can explore the whole energy landscape with virtually no bias and eventually provide unexpected results such as previously unknown crystal structures.

The computational techniques developed so far consider the crystal structure prediction as an optimization problem, in which the aim is to find the energy landscape's global minimum. To do that, these techniques seek deformations inside the energy landscape and follow them, trying to find the low energy regions, which are associated with dynamically stable structures. These low energy regions are usually close to each other, and they form *energy funnels* of different sizes and shapes, as shown in figure 1.2.

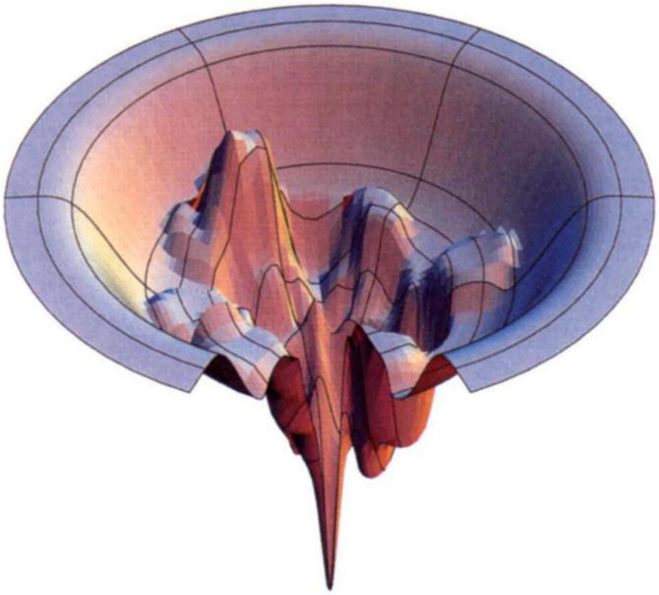

**Figure 1.2.** Energy landscape. It contains kinetics traps and energy barriers. Taken from [15].

Taking into account that in real chemical systems, there are only a few (sometimes even one) energy funnel, the efficiency of the searching can be significantly improved. Some of the techniques that use this fact are: Random Sampling, Simulated Annealing, Metadynamics, Molecular Dynamics and Evolutionary Algorithms. In the following sections we present and overview of these methods one by one.

## RANDOM SAMPLING

Random sampling is a stochastic method used to explore the energy surface of a system [16]. Eventually this technique was refined [17] [18] [19] [20] until it reached a wide accepted general procedure: given certain details of the system, e. g. the stoichiometry of a crystal or a protein sequence, the algorithm generates randomly the structure of the system, and by applying some local optimization algorithms, the total energy of a local minimum is calculated. This procedure is carried out until a satisfactory solution is achieved [21], as shown in figure 1.3

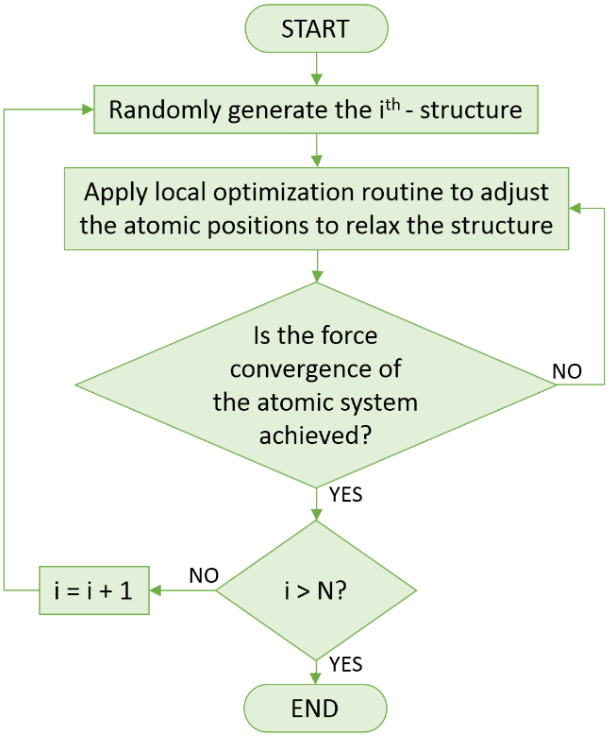
START
Randomly generate the ith - structure
Apply local optimization routine to adjust the atomic positions to relax the structure
Is the force convergence of the atomic system achieved?
NO
YES
i > N?
NO
i = i + 1
YES
END

**Figure 1.3.** Simplified version of a Random Sampling algorithm.

Chris J. Pickard and Richard Needs have applied widely this technique in several crystal molecular systems and semiconductors using DFT, such as: $SiH_4$ [22], $CaC_6$ [23], $AlH_3$ [24], $H_2O$ [25], hydrogen [26], nitrogen [27], iron [28] and lithium [29]. Some of these systems have up to 24 atoms per cell, but most of them contain less than 12 atoms per cell.

Some studies have combined this technique with others [30] [31] [32]. Also, Random Sampling has been applied for study small organic molecules for comparative effects [33] [34].

## SIMULATED ANNEALING

The simulated annealing algorithm is mostly based on Monte Carlo Metropolis algorithm, which describes a random path at constant temperature, using an acceptance criterion. When the temperature is no longer constant in the algorithm, the simulated annealing method is obtained [35] [36]. While the temperature is decreasing, the variation in the random path will be, in average, lower due to the constant decrease of energy. At the end of the process, the system is expected to reach the global energy minimum, but this depends on a well set up cooling process [37].

A simple way to understand the fundamentals of this algorithm is to imagine a hermetic box that contains an irregular surface inside and a sphere that is located at any point on that surface, as shown in figure 1.4.

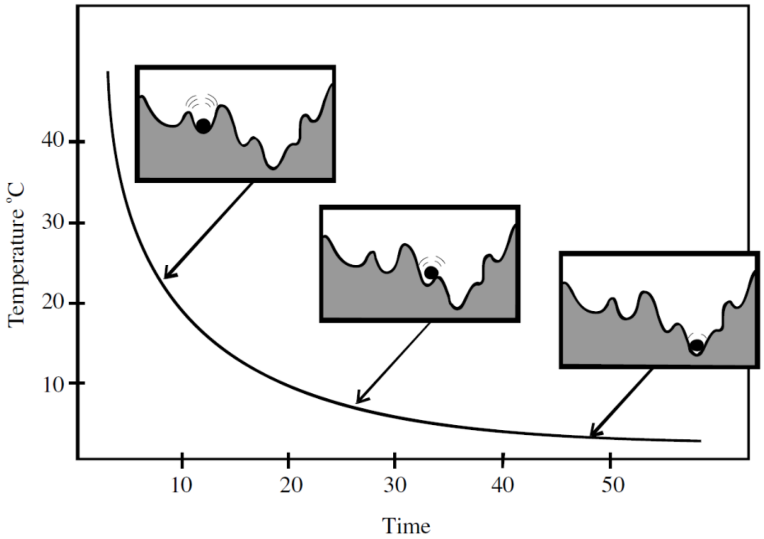

**Figure 1.4.** Schematic representation of simulated annealing. Taken from [38].

The goal is to move the sphere to the lowest point of the surface inside the box. At the beginning of the process the system temperature is high and some perturbations are applied to make the sphere get the energy to jump easily the peaks of the surface. While the temperature is decreasing, the sphere finds harder to jump those peaks, so it is expected that at the end of the process the sphere will be located at the lowest point of the surface, or in a worse-case scenario in a region near to the lowest point [38].

## MOLECULAR DYNAMICS

Molecular dynamics is a technique that aims to calculate the equilibrium dynamical properties of an N body physical system at a given set of temperatures. Although the behavior of all the particles could be described by Quantum Mechanics, Molecular Dynamics assumes, in principle, that atomic nuclei obey the Classical Mechanics laws, In fact, it doesn't take into account relativity or Quantum Mechanics for the nuclei [39] and this approximation has worked properly for several materials [40]. However, when it's necessary, semi-classical corrections can be applied to the desired system [41].

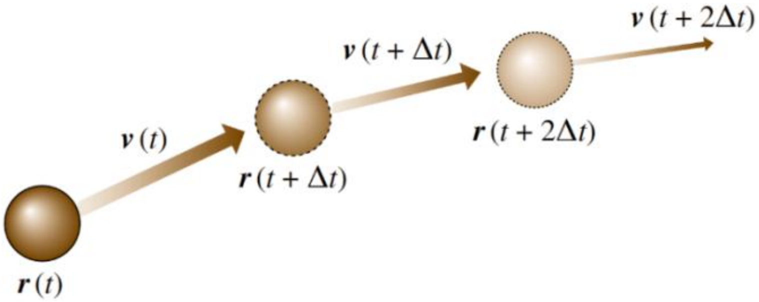
$\boldsymbol{v}(t+2\Delta t)$
$\boldsymbol{v}(t+\Delta t)$
$\boldsymbol{r}(t+2\Delta t)$
$\boldsymbol{v}(t)$
$\boldsymbol{r}(t+\Delta t)$
$\boldsymbol{r}(t)$

**Figure 1.5.** Particle trajectory in Molecular Dynamics simulation. Taken from [42].

Molecular Dynamics is based on determining the movement of the particles of the system resolving Newton's laws of motion. To achieve this, numerical integration is used on every particle, step by step, during certain period of time. The description of the particle trajectory, as shown in figure 1.5, has been described using several algorithms [43], which are detailed in table 1.2.

**Table 1.2.** Several algorithms used in Molecular Dynamics.

| ALGORITHM | EQUATIONS OF MOVEMENT |
|---|---|
| Verlet | $r(t+\Delta t) = 2r(t) - r(t-\Delta t) + \Delta t^2 a(t)$<br>$v(t) = \frac{r(t+\Delta t) - r(t-\Delta t)}{2}$ |
| Leap-frog Verlet | $r(t+\Delta t) = r(t) + \Delta t v\left(t + \frac{1}{2}\Delta t\right)$<br>$v\left(t+\frac{1}{2}\Delta t\right) = v\left(t - \frac{1}{2}\Delta t\right) + \Delta t a(t)$ |
| Velocity Verlet | $r(t+\Delta t) = r(t) + \Delta t v(t) + \frac{1}{2}\Delta t^2 a(t)$<br>$v(t+\Delta t) = v(t) + \frac{\Delta t[a(t) + a(t+\Delta t)]}{2}$ |
| Beeman | $r(t+\Delta t) = r(t) + \Delta t v(t) + \frac{2}{3}\Delta t^2 a(t) - \frac{1}{6}\Delta t^2 a(t-\Delta t)$<br>$v(t+\Delta t) = v(t) + \frac{1}{3}\Delta t a(t+\Delta t) + \frac{5}{6}\Delta t a(t) - \frac{1}{6}\Delta t a(t-\Delta t)$ |
| Gear Predictor-Corrector | $\tilde{q}(t+\Delta t) = Gq(t) \qquad q(t) = \begin{pmatrix} r(t) \\ \Delta t r'(t) \\ \frac{\Delta t^2 r''(t)}{2!} \\ \frac{\Delta t^3 r'''(t)}{3!} \\ \vdots \end{pmatrix}$<br>$q(t+\Delta t) = \tilde{q}(t+\Delta t) + A\Delta t^2 \times \frac{[F(t+\Delta t) - \hat{x}(t+\Delta t)]}{2}$ |
| Rahman | $r^P(t+\Delta t) = r(t-\Delta t) + 2\Delta t v(t)$<br>$v(t+\Delta t) = v(t) + \frac{\Delta t[a(t) + a(t+\Delta t)]}{2}$<br>$r(t+\Delta t) = r(t) + \frac{\Delta t[v(t) + v(t+\Delta t)]}{2}$ |

*Ab-initio* Molecular Dynamics has been widely developed by Michele Parrinello and Roberto Car, who made possible an efficient unification of this technique with Density Functional Theory, creating the Car – Parrinello algorithm [44] [45].

## METADYNAMICS

Metadynamics is an improvement on Molecular Dynamics which aims to reconstruct the free energy of complex systems using artificial dynamics. Taking into account that the free energy surface has many local minima separated by high barriers, the spontaneous transition from one local minimum to another is not easy to achieve. The algorithm first defines the dynamic variables (also called degrees of freedom) of the system inside a vector:

$$\widetilde{\boldsymbol{h}} = (h_{11},\ h_{22}, h_{33}, h_{44}, h_{55}, h_{66})^T \quad (3)$$

Following the generic metadynamic algorithm [46][26], the discrete dynamic of the system is defined:

$$\widetilde{\boldsymbol{h}}^{t+1} = \widetilde{\boldsymbol{h}}^{t} + \delta h \frac{\boldsymbol{\phi}^t}{|\boldsymbol{\phi}^t|} \qquad where\colon \boldsymbol{\phi}^t = -\frac{\partial G^t}{\partial \widetilde{\boldsymbol{h}}} \quad (4)$$

$$G^t(\widetilde{\boldsymbol{h}}) = G(\widetilde{\boldsymbol{h}}) + \sum_{t'<t} W e^{-\frac{\left|\widetilde{\boldsymbol{h}}-\widetilde{\boldsymbol{h}}^{t'}\right|^2}{2\delta h^2}} \quad (5)$$

The Gibbs potential, $G^t(\widetilde{\boldsymbol{h}})$ includes a Gaussian term that is added to each new point $\widetilde{\boldsymbol{h}}^{t'}$ in order to mark the points inside the free energy surface that have been already visited and avoid them in future iterations, by doing this the system is forced to leave one energy minimum while the simulation is going forward, due to the Gaussian contributions to the energy that are progressively filling the low potential regions allowing the system to go to other local minima and eventually covering the entire free energy surface. This process is shown in figure 1.6.

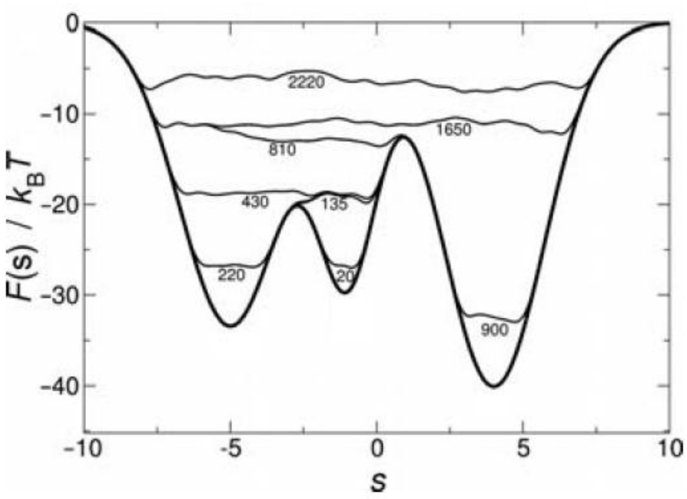

**Figure 1.6.** Schematic representation of the progressive filling of the underlying potential (thick line) by means of the Gaussian contributions deposited along the trajectory. The sum of the underlying potential and of the metadynamics bias is shown at different times (thin lines). Taken from [47].

## EVOLUTIONARY ALGORITHMS

This type of algorithm uses mechanisms inspired on biological evolution, such as reproduction, mutation, recombination and selection [48]. The possible solutions of the optimization problem are treated as individuals inside a population that evolves under the terms mentioned earlier and the quantity of individuals that will survive is determined by a *fitness solution*.

The algorithm itself can be implemented as follows [4] [5]: first of all, an accurate representation of the problem must be chosen. The quality of this representation has a direct impact in the effectiveness of the algorithm. Once the representation is set up, the first generation is created and the quality of life of each individual is determined by the fitness function. The best individuals of this generation are selected as parents of the next generation. The offspring will be ruled by the same fitness function, and the best individuals will create the third generation. These steps will be repeated until the convergence criteria is achieved.

## THE ELECTRONIC PROBLEM

Matter can be described (in very simplistic terms) as a set of atoms that interact with each other, sometimes under the influence of an external field. This arrangement of particles may be in the gas or in a condensed phase, which in turn can be a solid, liquid or amorphous phase. Despite the multiple ensembles that can be formed, all these systems can be described as a set of atomic nuclei and electrons that interact among themselves under the influence of electrostatic forces. Therefore the Hamiltonian of such system can be expressed as:

$$\hat{\mathcal{H}} = -\sum_{I=1}^{P}\frac{\hbar^2}{2M_I}\nabla_I^2 - \sum_{i=1}^{N}\frac{\hbar^2}{2m}\nabla_i^2 + \frac{e^2}{2}\sum_{I=1}^{P}\sum_{J\neq I}^{P}\frac{Z_I Z_J}{|\boldsymbol{R}_I - \boldsymbol{R}_J|} + \frac{e^2}{2}\sum_{i=1}^{N}\sum_{j\neq i}^{N}\frac{1}{|\boldsymbol{r}_i - \boldsymbol{r}_j|}$$
$$- e^2\sum_{I=1}^{P}\sum_{i=1}^{N}\frac{Z_I}{|\boldsymbol{R}_I - \boldsymbol{r}_i|} \qquad (6)$$

Where $\boldsymbol{R} = \{\boldsymbol{R}_I,\ I = 1 \ldots P\}$ and $\boldsymbol{r} = \{\boldsymbol{r}_i,\ i = 1 \ldots N\}$ are a set of *P* nuclear coordinates and *N* electronic coordinates. $Z_I$ and $M_I$ are the nuclear charges and masses respectively. The first and second term represent the kinetic energy of the *P* nuclei and the *N* electrons of the system. The third term represents the interaction between nuclei; this potential can be reduced to an additive constant when an approximation is used in order to resolve the electronic problem. The last two terms correspond to the interaction between electrons and the interaction between nuclei and electrons, respectively.

Before continuing, there are some considerations about the Hamiltonian expressed in equation (6) that have to be taken into account:

- The kinetic energy calculated in the first and second terms, and the motion of nuclei and electrons, are treated strictly in a non-relativistic way.
- The definition of each term of the Hamiltonian implies that the nuclei are treated as point particles, characterized only by their mass, charge and magnetic moment.
- The interaction between charged particles, calculated in the last three terms, is given by the instantaneous and spin-independent Coulomb interaction.

- The equation (6) shows a free-field system Hamiltonian. However, an electromagnetic field can be indicated when necessary, and this field can be either static or time-dependent.

In principle, all the properties of this system can be derived by solving the time-independent Schrödinger equation:

$$\hat{\mathcal{H}}\psi_n(\boldsymbol{R},\boldsymbol{r}) = \varepsilon_n\psi_n(\boldsymbol{R},\boldsymbol{r}) \quad (7)$$

Where $\varepsilon_n$ are the energy eigenvalues and $\psi_n(\boldsymbol{R},\boldsymbol{r})$ are the eigenstates, or wave functions. Since the electrons are fermions, the wave function must be antisymmetric with respect to the exchange of the electronic coordinates ***r***, and symmetric or antisymmetric with respect to the exchange of the nuclear coordinates ***R***, having into account that different nuclear species are distinguishable but the statistics used for systems made only of one type of atom depends on the nuclear spin of it.

However, in general this problem is practically impossible to solve analytically within the full quantum mechanics formalism: the system is a many-body system, where each particle position is described by three spatial coordinates. In addition, the Coulomb interaction is the result of pair-wise terms, so the Schrödinger equation cannot be separated. As a result of this limitation, we have to deal in principle with a 3(P+N) degrees of freedom problem. Nevertheless, several approximations have been proposed and refined in order to reduce the complexity of the electronic problem, one such approximation is the Born-Oppenheimer Approximation.

## BORN – OPPENHEIMER APPROXIMATION

The first step towards the solution of equation (6) is to partially decouple the electronic and the nuclear motion. This can be achieved due to the difference between the electrons' and nuclei's time-scales.

Inside the classical scheme and under typical conditions, the velocity of an electron is much larger than the proton's, because the mass of the proton is approximately 1836 times larger than the electron's. Taking that into account, Max Born and J. Robert Oppenheimer proposed in 1927 a way to separate the nuclear motion from the electronic motion [49].

Every time the nuclei move, the electrons adjust their positions very fast; therefore their wave function is always adjusted to the nuclear wave function almost instantaneously. Then the equation (7) can be solved with a factorized wave function that contains a nuclear component and an electronic component of the form:

$$\psi(\boldsymbol{R},\boldsymbol{r},t)=\sum_{n}\Theta_n(\boldsymbol{R},t)\Phi_n(\boldsymbol{R},\boldsymbol{r}) \quad (8)$$

Where $\Theta_n(\boldsymbol{R},t)$ are the wave functions that describe the evolution of the nuclear movement and $\Phi_n(\boldsymbol{R},\boldsymbol{r})$ are the electronic eigenstates. These terms satisfy the time-independent Schrödinger equation:

$$\hat{h}_e\Phi_n(\boldsymbol{R},\boldsymbol{r})=E_n(\boldsymbol{R})\Phi_n(\boldsymbol{R},\boldsymbol{r}) \quad (9)$$

This equation represents a stationary eigenvalue problem for a given set of parameters ***R***, which corresponds to the 3P nuclear coordinates and acts as a parameter of the equation. Therefore, the electronic problem has to be solved for a set of electronic positions ***r*** that depend on a particular nuclear configuration. Finally, the electronic Hamiltonian, according to the equation (6), is defined as follows:

$$\hat{h}_e=\hat{\mathcal{H}}+\sum_{I=1}^{P}\frac{\hbar^2}{2M_I}\nabla_I^2-\frac{e^2}{2}\sum_{I=1}^{P}\sum_{J\neq I}^{P}\frac{Z_IZ_J}{|\boldsymbol{R}_I-\boldsymbol{R}_J|}$$

$$\hat{h}_e=\hat{\mathcal{H}}-\hat{T}_n-\hat{V}_{nn}=\hat{T}+\hat{U}_{ee}+\hat{V}_{en} \quad (10)$$

Solving the time-independent Schrödinger equation will provide the key for understanding matter. However, in order to study the structure of matter, most of the time we only care about the ground electronic states. This does not imply that excited states are less important[2], but the complexity of the solution is higher than the one for ground states.

## HARTREE AND HARTREE – FOCK APPROXIMATIONS

Finding the ground state in an inhomogeneous system composed by N particles such as electrons, is one of the most important problems in the quantum many–body theory. Using the Dirac's Notation[3] and the electronic Hamiltonian defined in the equation (10), the ground state energy is given by:

$$E = \left\langle \Phi \middle| \hat{T} + \hat{V}_{ext} + \hat{U}_{ee} \middle| \Phi \right\rangle = \left\langle \Phi \middle| \hat{T} \middle| \Phi \right\rangle + \left\langle \Phi \middle| \hat{V}_{ext} \middle| \Phi \right\rangle + \left\langle \Phi \middle| \hat{U}_{ee} \middle| \Phi \right\rangle \quad (11)$$

Where $|\Phi\rangle$ is the N-electron ground state wave function, $\hat{T}$ is the kinetic energy operator, $\hat{V}_{ext}$ is a generalized form of the term $\hat{V}_{en}$ (electron–nucleus interaction defined in equation (10)), that corresponds to the interaction with fields that are external to the electronic system, and $\hat{U}_{ee}$ is the electron-electron interaction. These terms can be written as follows:

$$T = \left\langle \Phi \middle| \hat{T} \middle| \Phi \right\rangle = \left\langle \Phi \middle| \textstyle\sum_{i=1}^{N} \frac{-\hbar^2}{2m} \nabla_i^2 \middle| \Phi \right\rangle = \frac{-\hbar^2}{2m} \sum_{i=1}^{N} \langle \Phi | \nabla_i^2 | \Phi \rangle$$

$$T = \frac{-\hbar^2}{2m} \int [\nabla_i^2 \rho_1(\boldsymbol{r}, \boldsymbol{r}')]_{r=r'} d\boldsymbol{r} \quad (12)$$

$$V_{ext} = \left\langle \Phi \middle| \hat{V}_{ext} \middle| \Phi \right\rangle = \langle \Phi | \textstyle\sum_{i=1}^{N} v_{ext}(\boldsymbol{r}_i) \, | \Phi \rangle = \displaystyle\sum_{i=1}^{N} \langle \Phi | v_{ext}(\boldsymbol{r}_i) | \Phi \rangle$$

$$= \int [v_{ext}(\boldsymbol{r}) \rho_1(\boldsymbol{r}, \boldsymbol{r}')]_{r=r'} d\boldsymbol{r}$$

$$V_{ext} = \int v_{ext}(\boldsymbol{r}) \rho(\boldsymbol{r}) d\boldsymbol{r} \quad (13)$$

---

[2] Excited electronic states allow the study of phenomena like electronic transport, optical properties and photo-dissociation.

[3] For more detailed information on Dirac's Notation and Second Quantization, please remit to Appendix A.

$$U_{ee} = \langle \Phi | \widehat{U}_{ee} | \Phi \rangle = \left\langle \Phi \middle| \sum_{i=1}^{N} \sum_{j\neq i}^{N} \frac{1}{2} \frac{1}{|\boldsymbol{r}_i - \boldsymbol{r}_j|} \middle| \Phi \right\rangle = \frac{1}{2} \sum_{i=1}^{N} \sum_{j\neq i}^{N} \left\langle \Phi \middle| \frac{1}{|\boldsymbol{r}_i - \boldsymbol{r}_j|} \middle| \Phi \right\rangle$$

$$U_{ee} = \frac{1}{2} \iint \frac{\rho(\boldsymbol{r})\rho(\boldsymbol{r}')}{|\boldsymbol{r} - \boldsymbol{r}'|} d\boldsymbol{r} d\boldsymbol{r}' \quad (14)$$

Introducing the two-body direct correlation, $g(\boldsymbol{r}, \boldsymbol{r}')$, as:

$$\rho_2(\boldsymbol{r}, \boldsymbol{r}') = \rho(\boldsymbol{r})\rho(\boldsymbol{r}')g(\boldsymbol{r}, \boldsymbol{r}') \quad (15)$$

We have that for an uncorrelated system $g(\boldsymbol{r}, \boldsymbol{r}') = 1$, therefore the electron-electron interaction can be re-written as:

$$U_{ee} = \frac{1}{2} \iint \frac{\rho_2(\boldsymbol{r}, \boldsymbol{r}')}{|\boldsymbol{r} - \boldsymbol{r}'|} d\boldsymbol{r} d\boldsymbol{r}' \quad (16)$$

In this term the two-body interaction is reduced to a classical electrostatic interaction. This is known as the Hartree Approximation.

In order to build a more realistic model, the effect of the repulsion force produced by two electrons that are located at positions r and r', respectively, and are close to each other, has to be taken into account. This can be solved adding a term that includes both exchange and correlation effects:

$$U_{ee} = \frac{1}{2} \iint \frac{\rho_2(\boldsymbol{r}, \boldsymbol{r}')}{|\boldsymbol{r} - \boldsymbol{r}'|} d\boldsymbol{r} d\boldsymbol{r}' + \frac{1}{2} \iint \frac{\rho_2(\boldsymbol{r}, \boldsymbol{r}')}{|\boldsymbol{r} - \boldsymbol{r}'|} [g(\boldsymbol{r}, \boldsymbol{r}') - 1] d\boldsymbol{r} d\boldsymbol{r}' \quad (17)$$

In the Hartree approximation the electrons are treated as distinguishable particles. However, electrons are indistinguishable spin-1/2 fermions, so, their many-body wave function has to be anti-symmetric in order to obey Pauli's Exclusion Principle, but Hartree's approximation doesn't take this into account, as a consequence, the model that describes the electronic part of the atomic system is incomplete.

Pauli's Exclusion Principle can be easily introduced by proposing an anti-symmetrized many-body wave function in the form of a Slater determinant. Once we have done this, we are in the Hartree-Fock scheme:

$$\Phi_{HF}(\boldsymbol{x}_1, \boldsymbol{x}_2, \dots, \boldsymbol{x}_N) = \frac{1}{\sqrt{N!}}\begin{bmatrix} \varphi_1(1) & \varphi_2(1) & \cdots & \varphi_N(1) \\ \varphi_1(2) & \varphi_2(2) & \cdots & \varphi_N(2) \\ \vdots & \vdots & \ddots & \vdots \\ \varphi_1(N) & \varphi_2(N) & \cdots & \varphi_N(N) \end{bmatrix} \quad (18)$$

Where $\varphi_i(j)$ is the *i*-th one-electron spin orbital, which is composed of spatial and spin components that are condensed in a single variable ($\boldsymbol{x}_j = (\boldsymbol{r}_j, \sigma_j)$ and is the result of Hartree's assumption that the many-electron wave function can be expressed as a product of one-electron orbitals:

$$\Phi(\boldsymbol{r}) = \prod_{i=1}^{N} \varphi_i(\boldsymbol{r}_i) \quad (19)$$

Once we have set the wave function, we are able to determine the Hartree-Fock energy by calculating the one-electron contribution:

$$E^{(1)} = \int \Phi^*(\boldsymbol{r})\left(\sum_{i=1}^{N} \hat{h}_i(i)\right)\Phi(\boldsymbol{r})d\boldsymbol{r} = \sum_{i=1}^{N} E_{ii} \quad (20)$$

$$where: \hat{h}_i(i) = -\frac{\hbar^2}{2m}\nabla^2_{\boldsymbol{r}_i} + v_{ext}(\boldsymbol{R}, \boldsymbol{r}_i) \quad (21)$$

And the two-electron contribution to the energy:

$$E^{(2)} = \int \Phi^*(\boldsymbol{r})\left(\frac{1}{2}\sum_{i=1}^{N}\sum_{j\neq i}^{N} \hat{v}_2(i,j)\right)\Phi(\boldsymbol{r})d\boldsymbol{r} = \frac{1}{2}\sum_{i=1}^{N}\sum_{j\neq i}^{N}\left(J_{ij} - K_{ij}\right) \quad (22)$$

$$where: \hat{v}_2(i,j) = \frac{1}{\left|\boldsymbol{r}_i - \boldsymbol{r}'_j\right|} \quad (23)$$

Where the Coulomb and exchange integrals are defined as:

$$J_{ij} = \iint \varphi^*(i)\varphi^*(j)\hat{v}_2(i,j)\varphi(i)\varphi(j)d\boldsymbol{x}_i d\boldsymbol{x}_j \quad (24)$$

$$K_{ij} = \iint \varphi^*(i)\varphi^*(j)\hat{v}_2(i,j)\varphi(j)\varphi(i)d\boldsymbol{x}_i d\boldsymbol{x}_j \quad (25)$$

Finally the Hartree-Fock energy is:

$$E_{HF} = E^{(1)} + E^{(2)} = \sum_{i=1}^{N} E_{ii} + \frac{1}{2}\sum_{i=1}^{N}\sum_{j\neq i}^{N}\left(J_{ij} - K_{ij}\right) \quad (26)$$

The Hartree-Fock approximation, or Self-Consistent Field (SCF), is described in the following algorithm:

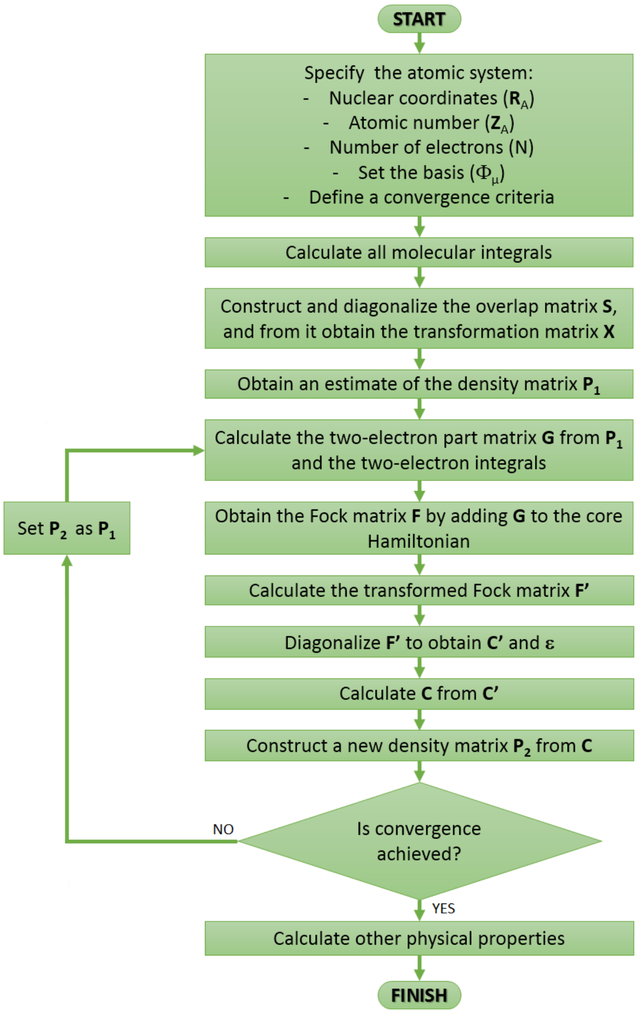
START
Specify the atomic system:
- Nuclear coordinates (**R**$_A$)
- Atomic number (**Z**$_A$)
- Number of electrons (N)
- Set the basis ($\Phi_\mu$)
- Define a convergence criteria
Calculate all molecular integrals
Construct and diagonalize the overlap matrix **S**, and from it obtain the transformation matrix **X**
Obtain an estimate of the density matrix **P**$_1$
Calculate the two-electron part matrix **G** from **P**$_1$ and the two-electron integrals
Obtain the Fock matrix **F** by adding **G** to the core Hamiltonian
Calculate the transformed Fock matrix **F'**
Diagonalize **F'** to obtain **C'** and ε
Calculate **C** from **C'**
Construct a new density matrix **P**$_2$ from **C**
Is convergence achieved?
NO
Set **P**$_2$ as **P**$_1$
YES
Calculate other physical properties
FINISH

**Figure 1.7.** Self-Consistent Field (SCF) algorithm. Adapted from [50].

Even when the determinant satisfies Pauli's Exclusion Principle, the wave function doesn't contain the correlation term that results from the interaction between electrons, or Coulomb interaction, but this can be solved by constructing the wave function $\Phi_{HF}(\boldsymbol{x}_1, \boldsymbol{x}_2, \dots, \boldsymbol{x}_N)$ with more than one determinant in what is known as a Configuration Interaction (CI) scheme.

## THOMAS – FERMI THEORY

By the same time when Hartree and Fock proposed their approach, L.H. Thomas and Enrico Fermi proposed a method for calculating the energy of an electronic system that depended only on the electronic density.

Fermi said that in the ground state of a gas of N free electrons, $|\Phi_0\rangle$, the particle states with wave number up to $k_F$ were occupied and lied within the Fermi sphere, as showed in figure 1.8. The zero temperature expectation value of the particle number operator in the momentum space is determined as:

$$n_{\boldsymbol{p},\sigma} = \langle\Phi_0|a^{\dagger}_{\boldsymbol{p},\sigma}a_{\boldsymbol{p},\sigma}|\Phi_0\rangle = \begin{cases} 1, & |\boldsymbol{p}| \le k_F \\ 0, & |\boldsymbol{p}| > k_F \end{cases} \qquad (27)$$

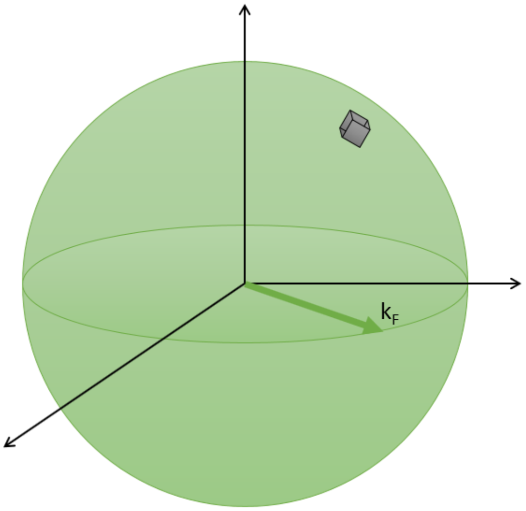

**Figure 1.8.** The Fermi sphere with an infinitesimal volume of $d\boldsymbol{p}^3$ in the real space, or $\left(\frac{2\pi}{L}\right)^3$ in the K-space.

The total particle number can be calculated as:

$$N = \sum_{\boldsymbol{p},\sigma} n_{\boldsymbol{p},\sigma} = 2\sum_{\boldsymbol{p}\leq k_F} 1 = 2\int_0^{k_F} \frac{d\boldsymbol{p}^3}{(2\pi/L)^3} = \frac{L^3}{4\pi^3}\int_0^{k_F} d\boldsymbol{p}^3 = \frac{V}{4\pi^3}\frac{4\pi {k_F}^3}{3} = \frac{V{k_F}^3}{3\pi^2} \quad (28)$$

Then, the mean particle density is:

$$\rho = \frac{N}{V} = \frac{{k_F}^3}{3\pi^2} \quad (29)$$

Where $k_F$ is the Fermi wave vector, the Fermi momentum is defined as $p_F = \hbar k_F$, and the Fermi energy, that is the energy of the top-most filled level in the ground state of the N free-electron system, is defined as $\epsilon_F = \frac{(\hbar k_F)^2}{2m}$. Now, the mean particle density $\rho$ in terms of the Fermi energy is:

$$\rho = \frac{1}{3\pi^2}\left(\frac{2m}{\hbar}\right)^{3/2} {\epsilon_F}^{3/2} \quad (30)$$

Fermi proposed an expression for the total electronic energy for an inhomogeneous system from the definition of kinetic, exchange and correlation contributions in the homogeneous gas:

$$E_\alpha[\rho] = \int \rho(\boldsymbol{r})\varepsilon_\alpha[\rho(\boldsymbol{r})]d\boldsymbol{r} \quad (31)$$

Where $\varepsilon_\alpha$ contains the kinetic, exchange and correlation energy density contributions, calculated locally at every point in space. This was the first attempt to obtain a Local Density Approximation (LDA) to the electronic problem.

As a remark, in the original Thomas-Fermi method, they neglected the exchange and correlation between electrons. The local approximation for exchange was introduced later by Dirac. Therefore, with the inclusion of that term the theory is now called Thomas-Fermi-Dirac. Then, the energy functional for an electron in an external potential $v_{ext}(\boldsymbol{r})$ is defined as:

$$E_{TFD}[\rho] = C_1 \int \rho(\boldsymbol{r})^{5/3} d\boldsymbol{r} + \int \rho(\boldsymbol{r}) v_{ext}(\boldsymbol{r}) d\boldsymbol{r} + \frac{1}{2} \iint \frac{\rho(\boldsymbol{r})\rho(\boldsymbol{r}')}{|\boldsymbol{r}-\boldsymbol{r}'|} d\boldsymbol{r} d\boldsymbol{r}' + C_2 \int \rho(\boldsymbol{r})^{4/3} d\boldsymbol{r} + E_C[\rho] \quad (32)$$

The first term is the LDA kinetic energy with $C_1 = \frac{3}{10}(3\pi^2)^{2/3} = 2.871a.u.$; the fourth term is the local exchange with $C_2 = -\frac{3}{4}\left(\frac{3}{\pi}\right)^{1/3} = 0.739a.u.$; and the last term is the correlation:

$$E_C[\rho] = -0.056 \int \frac{\rho(\boldsymbol{r})}{0.079 + \rho(\boldsymbol{r})^{1/3}} d\boldsymbol{r} \quad (33)$$

It is easy to realize that equation (32) only depends on the electronic density, that's the reason why it is said that this is a functional of the density. Nevertheless, the formal mathematical framework for this type of functional was developed by Hohenberg and Kohn more than thirty years after Thomas, Fermi and Dirac developed their idea of a density functional.

## HOHENBERG – KOHN THEOREMS

The approach of Hohenberg and Kohn was to formulate the density functional theory as an exact theory of many-body systems. Their theorems can be applied to any system of interacting particles in an external potential $v_{ext}(\boldsymbol{r})$. They also established a set of relations that are represented as:

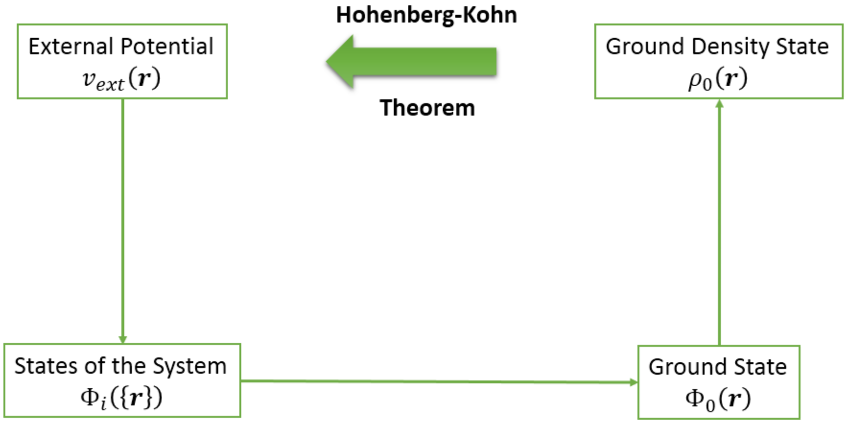
External Potential
$v_{ext}(\boldsymbol{r})$
Hohenberg-Kohn
Theorem
Ground Density State
$\rho_0(\boldsymbol{r})$
States of the System
$\Phi_i(\{\boldsymbol{r}\})$
Ground State
$\Phi_0(\boldsymbol{r})$

**Figure 1.9.** Schematic representation of Hohenberg-Kohn Theorem. Adapted from [51].

Where the thin arrows represent the usual solution of the Schrödinger equation, where the potential $v_{ext}(\boldsymbol{r})$ determines all the states of the system $\Phi_i(\{\boldsymbol{r}\})$, including the ground state $\Phi_0(\boldsymbol{r})$ and the density ground state $\rho_0(\boldsymbol{r})$. The Hohenberg-Kohn theorems complete the cycle. The following two theorems [51] are the foundation of the Density Functional Theory:

Theorem I: For any system of interacting particles in an external potential $v_{ext}(\boldsymbol{r})$, the potential $v_{ext}(\boldsymbol{r})$ is determined uniquely, except for a constant, by the ground state particle density $\rho_0(\boldsymbol{r})$.

**Proof:**

Suppose that we have two different external potentials $v_{ext}^1(\boldsymbol{r})$ and $v_{ext}^2(\boldsymbol{r})$, which differ by more than a constant. Each potential leads to a different Hamiltonian $\widehat{H}^1$ and $\widehat{H}^2$, which have different ground state wave function $\Phi^1$ and $\Phi^2$, which are hypothesized to have the same ground state density $\rho_0(\boldsymbol{r})$. Since $\Phi^2$ is not the ground state of $\widehat{H}^1$, we have:

$$E^1 = \langle \Phi^1 | \widehat{H}^1 | \Phi^1 \rangle < \langle \Phi^2 | \widehat{H}^1 | \Phi^2 \rangle$$

$\langle \Phi^2 | \widehat{H}^1 | \Phi^2 \rangle$ can be rewritten as:

$$\begin{aligned} \langle \Phi^2 | \widehat{H}^1 | \Phi^2 \rangle &= \langle \Phi^2 | \widehat{H}^2 | \Phi^2 \rangle + \langle \Phi^2 | \widehat{H}^1 - \widehat{H}^2 | \Phi^2 \rangle \\ &= E^2 + \int \rho_0(\boldsymbol{r})[v_{ext}^1(\boldsymbol{r}) - v_{ext}^2(\boldsymbol{r})]d\boldsymbol{r} \end{aligned}$$

Replacing:

$$E^1 < E^2 + \int \rho_0(\boldsymbol{r})[v_{ext}^1(\boldsymbol{r}) - v_{ext}^2(\boldsymbol{r})]d\boldsymbol{r}$$

Making the same procedure for $E^2$ we have:

$$E^2 < E^1 + \int \rho_0(\boldsymbol{r})[v_{ext}^2(\boldsymbol{r}) - v_{ext}^1(\boldsymbol{r})]d\boldsymbol{r}$$

$$= E^1 - \int \rho_0(\boldsymbol{r})[v_{ext}^1(\boldsymbol{r}) - v_{ext}^2(\boldsymbol{r})]d\boldsymbol{r}$$

Adding the two inequalities:

$$E^1 + E^2 < E^1 + E^2$$

This result is absurd, therefore is not possible that two different potentials can lead to the same ground density.

Corollary I: Since the Hamiltonian is thus fully determined, except for a constant shift of the energy, it follows that the many-body wave functions for all states (ground and excited) are determined. Therefore, all the properties of the system are completely determined given only the ground state density $\rho_0(\boldsymbol{r})$.

Theorem II: An universal functional for the energy $E[\rho]$ in terms of the density $\rho(\boldsymbol{r})$ can be defined, valid for any external potential $v_{ext}(\boldsymbol{r})$. For any particular $v_{ext}(\boldsymbol{r})$, the exact ground state energy of the system is the global minimum value of this functional and the density $\rho(\boldsymbol{r})$ that minimizes the functional is the exact ground state $\rho_0(\boldsymbol{r})$.

**Proof:**

Since all properties of the system are uniquely determined if $\rho(\boldsymbol{r})$ is specified, then the total energy functional can be expressed as:

$$E_{HK}[\rho] = T[\rho] + U_{ee}[\rho] + \int \rho(\boldsymbol{r})v_{ext}(\boldsymbol{r})d\boldsymbol{r} = F_{HK}[\rho] + \int \rho(\boldsymbol{r})v_{ext}(\boldsymbol{r})d\boldsymbol{r}$$

Let's consider a system with ground state density $\rho_0^1(\boldsymbol{r})$, which corresponds to the potential $v_{ext}^1(\boldsymbol{r})$. The Hohenberg-Kohn functional ($F_{HK}[\rho]$) is equal to the expectation value of the Hamiltonian in the unique ground state which has wave function $\Phi^1$.

$$E^1 = \langle \Phi^1 | \hat{H}^1 | \Phi^1 \rangle$$

Now, let's consider a different density $\rho_0^2(\boldsymbol{r})$ which corresponds to a different wave function $\Phi^2$. Then:

$$E^2 = \langle \Phi^2 | \hat{H}^1 | \Phi^2 \rangle > \langle \Phi^1 | \hat{H}^1 | \Phi^1 \rangle = E^1$$

Therefore the energy evaluated by $F_{HK}[\rho]$ is greater for any $\rho(\boldsymbol{r})$ different from the ground state density $\rho_0(\boldsymbol{r})$.

Corollary II: The functional $E[\rho]$ alone is sufficient to determine the exact ground state energy and density. In general, excited states of the electrons must be determined by other means.

In conclusion, $F_{HK}[\rho]$ is an universal functional which does not depend explicitly on the external potential, it depends only on the electronic density, and by knowing it we can know the solution of the full many-body Schrödinger equation.

## KOHN – SHAM METHOD

Nowadays, Density Functional Theory is one of the most used techniques for electronic structure calculations. This is because of the practical approach proposed by Kohn and Sham [52].

One good strategy, in order to solve the electronic problem, is to separate the different energy contributions. For instance, as discussed before, the separation of the Hartree term from the exchange and correlation contributions. Therefore, the electron-electron interaction is divided into three terms: Hartree, exchange, and correlation. The Hartree term is just the classical electrostatic energy, which is exact. The exchange term can be calculated exactly inside the Hartree-Fock scheme, however, due to computational reasons most of the time it is an approximate term. Finally, the correlation term, the smallest contribution to the energy, contains all of the unknowns about the many body problem.

The Kohn-Sham method reuses the idea of separation of elements: they replace the original many-body problem with a different auxiliary system that is easier to solve. The key of their idea is to assume that the ground state density of the interacting system is equal to the density of some chosen non-interacting system. As a consequence, a new set of particle-independent equations is defined for the non-interacting system and once they are solved we can find the ground state density and energy of the original system, with an error margin reduced to the approximation used in the exchange-correlation functional.

At this point, the main problem is with the kinetic energy term $T = \langle\Phi|\hat{T}|\Phi\rangle$, because its explicit expression in terms of the electronic density is unknown. In the Thomas-Fermi scheme, the kinetic energy is calculated locally, but this approach introduces an error into the model, given the non-local nature of this operator.

Kohn and Sham realized that a system of non-interacting electrons is exactly described by an anti-symmetrized wave function of the Slater determinant type, made of one-electron orbitals. Then, the ground state density matrix $\rho_1(\boldsymbol{r},\boldsymbol{r}')$ is given by:

$$\rho_1(\boldsymbol{r},\boldsymbol{r}') = \sum_{i=1}^{\infty} f_i \varphi_i(\boldsymbol{r}) \varphi_i^*(\boldsymbol{r}') \qquad (34)$$

Where $\varphi_i(\boldsymbol{r})$ are the one-electron orbitals and $f_i$ are the occupation numbers corresponding to those orbitals. Then, the exact expression of the kinetic energy of non-interacting electrons can be set as:

$$T = -\frac{\hbar^2}{2m} \sum_{i=1}^{\infty} f_i \langle\varphi_i|\nabla^2|\varphi_i\rangle \qquad (35)$$

Nevertheless, this expression is not the exact kinetic energy of the interacting system. The missing part is due to fact that the true many-body wave function is not a Slater determinant, therefore there is a correlation contribution to the kinetic energy that is not taken into account and must be included in the correlation term.

For now on, the equations defined here are in the equivalent non-interacting scheme. The non-interacting system made of N electrons and density $\rho(\boldsymbol{r})$ is described by the Hamiltonian:

$$\widehat{\mathcal{H}}_R = \sum_{i=1}^{N}\left[-\frac{\hbar^2}{2m}\nabla_i^2 + v_R\,(\boldsymbol{r}_i)\right] \quad (36)$$

Where $v_R\,(\boldsymbol{r})$ is the reference potential in which the ground state density of $\widehat{\mathcal{H}}_R$ equals $\rho(\boldsymbol{r})$. If that's so, the equivalence between the ground state energy and the energy of the interacting system is ensured by Hohenberg-Kohn's Theorem.

Given the nature of the electrons, the occupation number of each orbital is 2, where the total number of electrons is $N = N^{\uparrow} + N^{\downarrow}$ and $N_S = {}^{N}\!/_{2}$ is the number of orbitals with double occupancy. With these considerations, the density reads:

$$\rho(\boldsymbol{r}) = \sum_{\sigma}\sum_{i=1}^{N_S}|\varphi_i^{\sigma}(\boldsymbol{r})|^2 \quad (37)$$

The kinetic energy term is:

$$T_R[\rho] = -\frac{\hbar^2}{2m}\sum_{\sigma}\sum_{i=1}^{N_S}\langle\varphi_i^{\sigma}|\nabla^2|\varphi_i^{\sigma}\rangle = -\frac{\hbar^2}{2m}\sum_{\sigma}\sum_{i=1}^{N_S}|\nabla^2\varphi_i^{\sigma}(\boldsymbol{r})|^2 \quad (38)$$

And the Hartree term can be expressed as:

$$E_{Hartree}[\rho] = \frac{1}{2}\iint\frac{\rho(\boldsymbol{r})\rho(\boldsymbol{r}')}{|\boldsymbol{r}-\boldsymbol{r}'|}d\boldsymbol{r}d\boldsymbol{r}' \quad (39)$$

Now, the universal density functional can be rewritten as:

$$F[\rho] = T_R[\rho] + E_{Hartree}[\rho] + \tilde{E}_{XC}[\rho]$$

$$F[\rho] = -\frac{\hbar^2}{2m}\sum_{\sigma}\sum_{i=1}^{N_S}|\nabla^2\varphi_i^{\sigma}(\boldsymbol{r})|^2 + \frac{1}{2}\iint\frac{\rho(\boldsymbol{r})\rho(\boldsymbol{r}')}{|\boldsymbol{r}-\boldsymbol{r}'|}d\boldsymbol{r}d\boldsymbol{r}' + \tilde{E}_{XC}[\rho] \quad (40)$$

The term $\tilde{E}_{XC}[\rho]$ does not only contain the exchange and correlation energy defined in equation 17, but also takes into account the kinetic correlation ignored in $T_R[\rho]$. Finally, we get the total energy functional:

$$\begin{aligned} E_v[\rho] = E_{KS}[\rho] = F[\rho] + \int \rho(\boldsymbol{r})v_{ext}(\boldsymbol{r})d\boldsymbol{r} \\ = T_R[\rho] + E_{Hartree}[\rho] + \tilde{E}_{XC}[\rho] + \int \rho(\boldsymbol{r})v_{ext}(\boldsymbol{r})d\boldsymbol{r} \quad (41) \end{aligned}$$

If the universal $\tilde{E}_{XC}[\rho]$ was known, then the exact ground state energy and density of the many-body problem could be found by solving the Kohn-Sham equations for a non-interacting system.

## EXCHANGE AND CORRELATION IN DFT

In order to solve the electronic problem, the strategy used was to separate the total energy into a number of different contributions:

$$E[\rho] = T_R + v_{ext} + E_H + E_X + \tilde{E}_C \quad (42)$$

In order of appearance there are: non-interacting kinetic energy, the interaction of the electrons with an external field, the classical electron-electron interaction, the exchange energy, and the coupling constant averaged correlation term.

This correlation energy is the central query. For instance, the exchange energy, as defined in equation 25 is very accurate: this calculation demands a lot of computer resources and usually several approximations are used in order to estimate its value, even when some error is introduced in the calculation. However, there isn't an expression for the correlation energy with a level of accuracy comparable to that of the exchange energy. One way to address this issue is to consider the exchange and the correlation energy contributions, not independently, but as a sum of both terms $E_X + \tilde{E}_C$.

The idea is now to find an approximation for both exchange and correlation, where they can be treated in a similar way. As seen before, one of the starting points for these approaches is the homogeneous gas and some approximations have been developed so far [53] [54] [55].

## *Local Density Approximation – LDA*

Local Density Approximation (LDA) was first formally introduced by Kohn and Sham [52], however the idea was used by Thomas, Fermi and Dirac in their theory.

Basically LDA approach is to consider the inhomogeneous electronic system as a local homogeneous electron gas in which the exchange-correlation hole for this system is very accurate. The local energy is calculated at every point **r** with electronic density $\rho(\boldsymbol{r})$. Therefore, the exchange-correlation energy can be written in terms of the average energy density $\tilde{\epsilon}_{XC}^{LDA}[\rho]$:

$$\tilde{E}_{XC}^{LDA}[\rho] = \int \rho(\boldsymbol{r})\tilde{\epsilon}_{XC}^{LDA}[\rho(\boldsymbol{r})]d\boldsymbol{r} \qquad (43)$$

With

$$\tilde{\epsilon}_{XC}^{LDA}[\rho(\boldsymbol{r})] = \frac{1}{2}\int \frac{\tilde{\rho}_{XC}^{LDA}(\boldsymbol{r},\boldsymbol{r}')}{|\boldsymbol{r}-\boldsymbol{r}'|}d\boldsymbol{r}' \qquad (44)$$

Where $\tilde{\rho}_{XC}^{LDA}(\boldsymbol{r},\boldsymbol{r}')$ is the exchange-correlation hole and is defined as:

$$\tilde{\rho}_{XC}^{LDA}(\boldsymbol{r},\boldsymbol{r}') = \rho(\boldsymbol{r})\{\tilde{g}^h[|\boldsymbol{r}-\boldsymbol{r}'|,\rho(\boldsymbol{r})\,]-1\} \quad (45)$$

With $\tilde{g}^h[|\boldsymbol{r}-\boldsymbol{r}'|,\rho(\boldsymbol{r})\,]$ as the pair correlation function of the homogeneous gas. In practice the exchange-correlation energy is calculated according to equation 43 but using $\tilde{\epsilon}_{XC}^{LDA}[\rho] = \epsilon_X^{LDA}[\rho] + \tilde{\epsilon}_C^{LDA}[\rho]$ as illustrated in table 1.3.

**Table 1.3.** Expressions used to calculate the exchange-correlation energy in LDA. Adapted from **[56]**.

<table>
<tr><th colspan="5">$\tilde{\boldsymbol{\epsilon}}_{\boldsymbol{XC}}^{\boldsymbol{LDA}}[\boldsymbol{\rho}] = \boldsymbol{\epsilon}_{\boldsymbol{X}}^{\boldsymbol{LDA}}[\boldsymbol{\rho}]+\tilde{\boldsymbol{\epsilon}}_{\boldsymbol{C}}^{\boldsymbol{LDA}}[\boldsymbol{\rho}]$</th></tr>
<tr><th>$\boldsymbol{\epsilon}_{\boldsymbol{X}}^{\boldsymbol{LDA}}[\boldsymbol{\rho}]$</th><th colspan="4">$\tilde{\boldsymbol{\epsilon}}_{\boldsymbol{C}}^{\boldsymbol{LDA}}[\boldsymbol{\rho}]$</th></tr>
<tr><td rowspan="4">$-\frac{3}{4}\left(\frac{3}{\pi}\right)^{1/3}\rho^{1/3} = -\frac{3}{4}\left(\frac{9}{4\pi^2}\right)^{1/3}\frac{1}{r_s} = -\frac{0,458}{r_s}a.u.$<br>Where $r_s = \left(\frac{3}{4\pi\rho}\right)^{1/3}$ is the mean interelectronic distance in atomic units.</td><td colspan="4">$\begin{cases} A\ln(r_s) + B + C\,r_s\ln(r_s) + D\,r_s, & r_s \le 1 \\ \dfrac{\gamma}{1+\beta_1\sqrt{r_s}+\beta_2 r_s}, & r_s > 1 \end{cases}$</td></tr>
<tr><th colspan="2">Coefficients for spin-unpolarized homogeneous electron gas [57][59]</th><th colspan="2">Coefficients for spin-polarized homogeneous electron gas [58][59]</th></tr>
<tr><td>$A = 0,0311$<br>$B = -0,048$<br>$C = 0,0020$<br>$D = -0,0116$</td><td>$\gamma = -0,1423$<br>$\beta_1 = 1,0529$<br>$\beta_2 = 0,3334$</td><td>$A = 0,01555$<br>$B = -0,0269$<br>$C = 0,0007$<br>$D = -0,0048$</td><td>$\gamma = -0,0843$<br>$\beta_1 = 1,3981$<br>$\beta_2 = 0,2611$</td></tr>
<tr><td colspan="4">$\rho(\boldsymbol{r})\{\tilde{g}^h[|\boldsymbol{r}-\boldsymbol{r}'|,\rho(\boldsymbol{r})]-1\}$</td></tr>
</table>

As a final remark, the main limitations of LDA are [56]:

- The inhomogeneities in the electronic density are not taken into account.
- The self-interaction present in the Hartree term is not completely cancelled by the LDA exchange-correlation term.
- LDA does not include non-local exchange and correlation effects.
- Strong local correlation effects cannot be reproduced.

### ***Generalized Gradient Approximation – GGA***

The Generalized Gradient Approximations (GGAs) were the way to try to solve LDA's issues, especially regarding the inhomogeneities in the electronic densities. These approximations propose an expansion of the density in terms of the gradient and other higher order derivatives, this expansion leads to the following exchange-correlation energy:

$$E_{XC}[\rho] = \int \rho(\boldsymbol{r})\varepsilon_{XC}[\rho(\boldsymbol{r})]F_{XC}[\rho(\boldsymbol{r}), \nabla\rho(\boldsymbol{r}), \nabla^2\rho(\boldsymbol{r}), \dots]\, d\boldsymbol{r} \quad (46)$$

Where $F_{XC}$ is a factor that modifies the LDA expression, according to the variation of the density in the vicinity of one specific point. As a consequence, the energy is not calculated locally, but semi-locally. However, this approach is deficient when non-local effects have to be taken into account.

The second order gradient expansion of the exchange energy correspond to an expression of the type:

$$E_{XC}[\rho] = \int A_{XC}[\rho(\boldsymbol{r})]\rho(\boldsymbol{r})^{4/3}\, d\boldsymbol{r} + \int \frac{C_{XC}[\rho(\boldsymbol{r})]|\nabla\rho(\boldsymbol{r})|^2}{\rho(\boldsymbol{r})^{4/3}}\, d\boldsymbol{r} \quad (47)$$

Nevertheless, each term of the gradient expansion must be addressed very carefully, because some of them tend to violate at least one of the exact conditions required for the exchange and correlation holes, such as the normalization condition, the negativity of the exchange density or the self-interaction cancellation [56]. With these limitations in mind, there are two approaches to obtain GGAs:

- The first one is to obtain the GGA via theoretical methods, where the coefficients are set up in such a way that the exact results of certain known parameters can be reproduced, like sum rules and long-range decay.
- The second method is to fit the parameters in order to reproduce a set of experimental results. Typical parameters are formation energies, thermochemical data and structural parameters.

Several gradient expansions have been proposed, mostly between the 80's and mid 90's. Three of the most used are summarized in table 1.4.

**Table 1.4.** Summary of several GGA functionals. Adapted from [**56**].

| GGA's Functionals | | |
|---|---|---|
| **Langreth – Mehl Functional [60]** | | |
| $\varepsilon_X = \varepsilon_X^{LDA} = a\frac{\lvert\nabla\rho(\boldsymbol{r})\rvert^2}{\rho(\boldsymbol{r})^{4/3}}\left(\frac{7}{9} + 18f^2\right)$<br>$\varepsilon_C = \varepsilon_C^{RPA} + a\frac{\lvert\nabla\rho(\boldsymbol{r})\rvert^2}{\rho(\boldsymbol{r})^{4/3}}(2e^{-F} + 18f^2)$ | $F = b\frac{\lvert\nabla\rho(\boldsymbol{r})\rvert}{\rho(\boldsymbol{r})^{7/6}}$<br>$b = (9\pi)^{1/6}f$ | $a = \frac{\pi}{16(3\pi^2)^{4/3}}$<br>$f = 0{,}15$ |
| **BLYP Functional [61][62]** | | |
| $\varepsilon_X = \varepsilon_X^{LDA} = \left(1 - \frac{\beta}{2^{1/3}A_x}\frac{x^2}{1 + 6\beta x \sinh^{-1}(x)}\right)$<br>$\varepsilon_C = -\frac{a}{1 + d\rho^{-1/3}}\left\{\rho + b\rho^{-2/3}\left[C_F\rho^{5/3} - 2tw + \frac{1}{9}\left(tw + \frac{1}{2}\nabla^2\right)\right]e^{-c\rho^{-1/3}}\right\}$<br>$Where{:}\ tw = \frac{1}{8}\left(\frac{\lvert\nabla\rho\rvert^2}{\rho} - \nabla^2\rho\right)$ | $x = \frac{2^{1/3}\lvert\nabla\rho(\boldsymbol{r})\rvert}{\rho(\boldsymbol{r})^{4/3}}$<br>$A_x = \frac{3}{4}\left(\frac{3}{\pi}\right)^{1/3}$<br>$\beta = 0{,}0042$ | $C_F = \frac{3}{10}\frac{1}{(3\pi^2)^{2/3}}$<br>$a = 0{,}04918$<br>$b = 0{,}132$<br>$c = 0{,}2533$<br>$d = 349$ |
| **PBE Functional [63]** | | |
| $E_{XC}[\rho] = \int \rho(\boldsymbol{r})\varepsilon_{XC}[\rho(\boldsymbol{r})]F_{XC}[\rho(\boldsymbol{r}), \nabla\rho(\boldsymbol{r}), \nabla^2\rho(\boldsymbol{r})]\, d\boldsymbol{r}$<br>$Where{:}\ F_{XC}(s) = 1 + \kappa - \frac{\kappa}{1 + {\mu s^2}/{\kappa}}$<br>$E_C^{GGA} = \int \rho(\boldsymbol{r})\left[\varepsilon_C^{LDA}(\rho, \zeta) + H[\rho, \zeta, t]\right] d\boldsymbol{r}$<br>$Where{:}\ H[\rho, \zeta, t] = \left(\frac{e^2}{a_0}\right)\gamma\phi^3 \ln\left[1 + \frac{\beta}{\gamma}t^2\left(\frac{1 + At^2}{1 + At^2 + A^2t^4}\right)\right]$ | $\phi(\zeta) = \frac{(1 + \zeta)^{2/3} + (1 - \zeta)^{2/3}}{2}$<br>$t = \frac{\lvert\nabla\rho(\boldsymbol{r})\rvert}{2\phi\kappa_s\rho}$<br>$A = \frac{\beta}{\gamma}\left[e^{\frac{-\varepsilon_C^{LDA}[\rho]}{\gamma\phi^3 e^2/a_0}} - 1\right]^{-1}$ | $\beta = 0{,}066725$<br>$\gamma = \frac{1 - \ln(2)}{\pi^2} = 0{,}031091$<br>$\mu = \beta\left(\frac{\pi^2}{3}\right) = 0{,}21951$ |

The development of several GGAs marked an improvement over LDA in different aspects such as binding energies, atomic energies, bond lengths and angles. However, there are some other features that need to be enhanced [56]:

- LDA describes better semiconductors than GGA.
- The improvement of GGA over LDA for 4d – 5d transition metals and the gap energy is either not clear or not substantial in several cases.
- GGA does not satisfy some known asymptotic behaviors, e. g. isolated atoms.
- GGA functionals still do not compensate satisfactorily the self-interaction present in the Hartree term.

## PSEUDOPOTENTIALS AND BASIS SETS

Since the early stages of quantum mechanics, the solution of the many-body quantum problem is the main mathematical problem in electronic structure theory. The two main methodologies proposed to address this problem, Hartree-Fock and Kohn-Sham, provide a tractable way to deal with this problem, but they are approximates schemes.

The solution either of the Hartree-Fock or Kohn-Sham equations, regardless their approximated nature, requires two important choices [56]:

- How to treat the electron-nuclear interaction.
- Find a mathematical way to represent the single particle orbitals.

### ***Pseudopotentials***

The electron-nuclear interaction is given by the Coulomb potential defined as:

$$v_{ext}(\boldsymbol{r}) = -e^2 \sum_{I=1}^{P} \sum_{i=1}^{N} \frac{Z_I}{|\boldsymbol{R}_I - \boldsymbol{r}_i|} \quad (48)$$

However, and as a manner of speak, there's exist a distinction between three different classes of electrons[4]:

*Core electrons:* they are tightly bound to the nuclei and are not involved in chemical bonding. Also they can be treated as frozen orbitals.

*Valence electrons:* they are extended and participate actively in chemical bonding.

*Semi-core electrons:* usually, they do not contribute directly to chemical bonding, due to their localized nature. However, they are close enough in energy to the valence states to feel the presence of the environment, therefore they cannot be treated as frozen orbitals.

Since the core electrons are not fundamental for the description of the chemical bonding, it is possible to replace the charge of the atomic nuclei, which is treated point-like, with an effective nucleus charge of:

$$Z_v = Z - Z_{core} \quad (49)$$

---

[4] All electrons are the same, but this language abuse is used to indicate single-particle electronic states rather than electrons themselves.

Where $Z_{core}$ is the charge associated to the core electrons. This effective core potential, or pseudopotential, represents the nucleus with its core electrons and it reduces significantly the number of degrees of freedom of the electron gas because the number of electrons treated explicitly is smaller, thus the number of required electronic states and the size of the basis set is also reduced.

When the valence wave functions inside the core region can be neglected, these can be replaced with a smooth, nodeless pseudo-wave function as shown in figure 1.10:

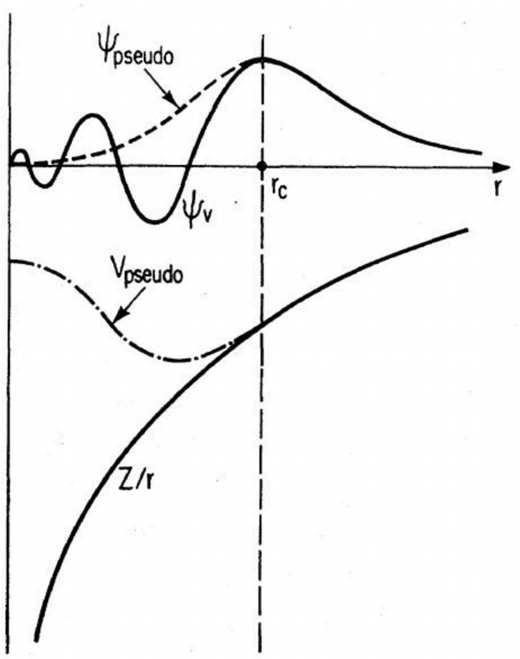

**Figure 1.10.** Schematic illustration of all-electron (solid lines) and pseudoelectron (dashed lines) potentials and their corresponding wave functions. The radius at which all-electron and pseudoelectron values match is designated $r_c$. Taken from [64].

The pseudopotentials have to be constructed very carefully in order to reproduce accurately the bonding properties of the all-electron potential, but maintaining the nodeless shape inside the core radius $r_s$, and the construction is described in figure 1.11.

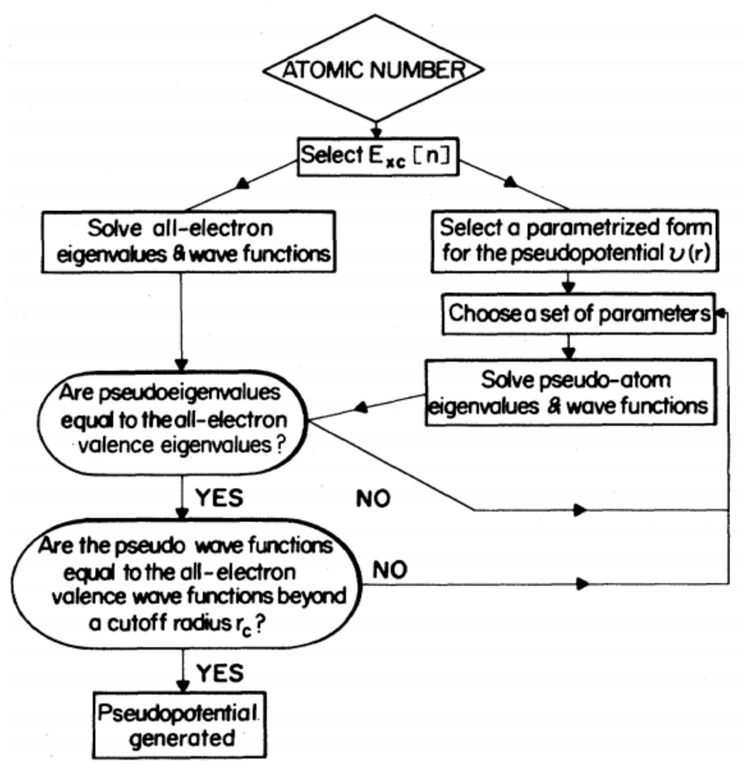
ATOMIC NUMBER
Select $E_{xc}[n]$
Solve all-electron eigenvalues & wave functions
Select a parametrized form for the pseudopotential $\upsilon(r)$
Choose a set of parameters
Solve pseudo-atom eigenvalues & wave functions
Are pseudoeigenvalues equal to the all-electron valence eigenvalues?
YES
NO
Are the pseudo wave functions equal to the all-electron valence wave functions beyond a cutoff radius $r_c$?
NO
YES
Pseudopotential generated

**Figure 1.11.** Flow chart describing the construction of an ionic pseudopotential for an atom. Taken from [64].

Finally, the most used pseudopotentials are non-conserving [65] [66] [67] [68] [69] and ultra-soft [70].

## ***Basis Sets***

In order to solve the electronic problem in practice, it is necessary to find a mathematical representation for the one-electron orbitals. One possibility is to represent them in real space using a three-dimensional grid and then solve the partial differential equations using finite differences.

Since the beginning of quantum mechanics, several basis sets have been developed for the Hilbert space based on the general characteristics and specific features of the system under study. Nowadays, the representation of the Kohn-Sham orbitals can be classified into four groups [56]:

- *Extended basis sets:* they are delocalized basis functions, either centered at the nuclear position or independent of them. Their most important feature is that they cover the whole space, therefore they are mostly used for condensed phases like solids and liquids.
- *Localized basis sets:* as the name says, they are localized mainly at the atomic positions, but they can be centered in bonds. They are mostly used for molecular systems.
- *Mixed basis sets:* they combine features from the extended and localized basis sets. However, their weakest point is the amount of technical issues when implemented.
- *Augmented basis sets:* they are atomic like wave functions that augment and extended or localized basis set in spherical regions around the nuclei. The main feature is their high level of accuracy, but, from the technical point of view, they are much more complicated to implement.

In this work we will be dealing mainly with a basis set of the extended type, i.e. plane waves.

## REFERENCES

[1] A. Oganov, «Introduction: Crystal Structure Prediction, a Formidable Problem,» from *Modern Methods of Crystal Structure Prediction*, New York, WILEY-VCH Verlag & Co. KGaA, 2011, pp. xi - xxi.

[2] J. Maddox, «Crystals from first principles,» *Nature,* vol. 335, n° 6187, p. 201, 1988.

[3] P. Erk, «Crystal Design,» de *Crystal Engineering: From Molecules and Crystals to Materials*, Springer Netherlands, 1999, pp. 143 - 161.

[4] A. R. Oganov and C. Glass, «Crystal structure prediction using ab initio evolutionary techniques: Principles and applications,» *Journal of Chemical Physics,* vol. 124, n° 24, p. 244704, 2006.

[5] C. W. Glass, A. R. Oganov and N. Hansen, «USPEX—Evolutionary crystal structure prediction. Computer Physics Communications,» *Computer Physics Communications,* vol. 175, n° 11 - 12, pp. 713 - 720, 2006.

[6] G. N. Lewis, «The atom and the molecule,» *Journal of the American Chemical Society,* vol. 38, n° 4, pp. 762 - 785, 1916.

[7] L. Pauling, «The Principles Determining the Structure of Complex Ionic Crystals,» *Journal of the American Chemical Society,* vol. 51, n° 4, pp. 10010 - 1026, 1929.

[8] I. D. Brown, «Bond valences—a simple structural model for inorganic chemistry,» *Chemical Society Reviews,* vol. 7, n° 3, pp. 359 - 376, 1978.

[9] I. D. Brown, The Chemical Bond in Inorganic Chemistry: The Bond Valence Model, New York: OUP Oxford, 2006.

[10] A. F. Wells, «The geometrical basis of crystal chemistry. Part 1,» *Acta Crystallographica,* vol. 7, n° 8 - 9, pp. 535 -544, 1954.

[11] A. F. Wells, «The geometrical basis of crystal chemistry. Part 2,» *Acta Crystallographica,* vol. 7, n° 8 - 9, pp. 545 - 554, 1954.

[12] A. F. Wells, «The geometrical basis of crystal chemistry. Part 3,» *Acta Crystallographica,* vol. 7, n° 12, pp. 842 - 848, 1954.

[13] A. F. Wells, «The geometrical basis of crystal chemistry. Part 4,» *Acta Crystallographica,* vol. 7, n° 12, pp. 849 - 853, 1954.

[14] V. A. Blatov, «A method for hierarchical comparative analysis of crystal structures,» *Acta Crystallographica Section A,* vol. 62, n° 5, pp. 356 - 364, 2006.

[15] K. A. Dill and H. S. Chan, «From Levinthal to pathways to funnels,» *Nature Structural Biology,* vol. 4, n° 1, pp. 10 - 19, 1997.

[16] R. L. Anderson, «Recent Advances in Finding Best Operating Conditions,» *Journal of the American Statistical Association,* vol. 48, n° 264, pp. 789 - 798, 1953.

[17] L. A. Rastrigin, «The convergence of the random search method in the extremal control of a many parameter system,» *Automation and Remote Control,* vol. 24, n° 11, pp. 1337 - 1342, 1963.

[18] D. C. Karnopp, «Random search techniques for optimization problems,» *Automatica,* vol. 1, n° 2 - 3, pp. 111 - 121, 1963.

[19] J. C. Spall, Introduction to Stochastic Search and Optimization, New Jersey: John Wiley & Sons, 2003.

[20] A. Zhigljavsky and A. Zilinskas, Stochastic Global Optimization, New York: Springer, 2008.

[21] W. Tipton and R. Henning, «Random Search Methods,» from *Modern Methods of Crystal Structure Prediction*, New York, WILEY-VCH Verlag & Co. KGaA, 2011, pp. 55 - 66.

[22] C. J. Pickard and R. J. Needs, «High-Pressure Phases of Silane,» *Physical Review Letters,* vol. 97, n° 4, p. 045504, 2006.

[23] G. Csányi, C. J. Pickard, B. D. Simmons and R. J. Needs, «Graphite intercalation compounds under pressure: A first-principles density functional theory study,» *Physical Review B,* vol. 75, n° 8, p. 085432, 2007.

[24] C. J. Pickard and R. J. Needs, «Metallization of aluminum hydride at high pressures: A first-principles study,» *Physical Review B,* vol. 76, n° 14, p. 144114, 2007.

[25] C. J. Pickard and R. J. Needs, «When is H2O not water?,» *Journal of Chemical Physics,* vol. 127, n° 24, p. 244503, 2007.

[26] C. J. Pickard and R. J. Needs, «Structure of phase III of solid hydrogen,» *Nature,* vol. 3, n° 7, pp. 473 - 476, 2007.

[27] C. J. Pickard and R. J. Needs, «High-Pressure Phases of Nitrogen,» *Physical Review Letters,* vol. 102, n° 12, p. 125702, 2009.

[28] C. J. Pickard and R. J. Needs, «Stable phases of iron at terapascal pressures,» *Journal of Physics: Condensed Matter,* vol. 21, n° 45, p. 452205, 2009.

[29] C. J. Pickard and R. J. Needs, «Dense Low-Coordination Phases of Lithium,» *Physical Review Letters,* vol. 102, n° 14, p. 146401, 2009.

[30] M. S. Bailey, N. T. Wilson, C. Roberts and R. L. Johnson, «Structures, stabilities and ordering in Ni-Al nanoalloy clusters,» *The European Physical Journal D,* vol. 25, n° 1, pp. 41 - 55, 2003.

[31] H. A. Scheraga, «Recent developments in the theory of protein folding: searching for the global energy minimum,» *Biophysical Chemistry,* vol. 59, n° 3, pp. 329 - 339, 1996.

[32] D. J. Wales and H. A. Scheraga, «Global Optimization of Clusters, Crystals, and Biomolecules,» *Science,* vol. 285, n° 5432, pp. 1368 - 1372, 1999.

[33] J. P. Lommerse, W. D. Motherwell, H. L. Ammon, J. D. Dunitz, A. Gavezzotti, D. W. Hofmann, F. J. Leusen, W. T. Mooij, S. L. Price, B. Schweizer, M. U. Schmidt, B. P. Van Eijck, P. Verwer and D. E. Williams, «A test of crystal structure prediction of small organic molecules,» *Acta Crystallographica Section B,* vol. 56, n° 4, pp. 697 - 714, 2000.

[34] W. D. Motherwell, H. L. Ammon, J. D. Dunitz, A. Dzyabchenko, P. Erk, A. Gavezzotti, D. W. Hofmann, F. J. Leusen, J. P. Lommerse, W. T. Mooij, S. L. Price, H. Scheraga, B. Schweizer, M. U. Schmidt, B. P. Van Eijck, P. Verwer and D. E. Williams, «Crystal structure prediction of small organic molecules: a second blind test,» *Acta Crystallographica Section B,* vol. 58, n° 4, pp. 647 - 661, 2002.

[35] S. Kirkpatrick, C. D. Gelatt Jr. and M. P. Vecchi, «Optimization by Simulated Annealing,» *Science,* vol. 220, n° 4598, pp. 671 - 680, 1983.

[36] V. Černý, «Thermodynamical approach to the traveling salesman problem: An efficient simulation algorithm,» *Journal of Optimization Theory and Applications,* vol. 45, n° 1, pp. 41 - 51, 1985.

[37] J. Schön and J. Martin, «Predicting Solid Compounds Using Simulated Annealing,» from *Modern Methods of Crystal Structure Prediction*, New York, WILEY-VCH Verlag & Co. KGaA, 2011, pp. 67 - 105.

[38] S. Ledesma, G. Aviña and R. Sánchez, «Practical Considerations for Simmulated Annealing Implementation,» de *Simulated Annealing*, New York, I-Tech Education, 2008, pp. 401 - 420.

[39] D. Rapaport, The art of molecular dynamics simulation, New York: Cambridge University Press, 2004.

[40] D. Frenkel and B. Smith, Understanding molecular simulation, Amsterdam: Amsterdam Academic Press, 2002.

[41] G. C. Maitland, Intermolecular forces: their origin and determination, Michigan: Clarendon Press, 1981.

[42] H. Czichos, T. Saiato and L. Smith, Springer Handbook of Materials Mesaurement Methods, Würzburg: Springer, 2006.

[43] M. P. Allen and D. J. Tildesley, Computer Simulation of Liquids, New York: Oxford University Press, 1991.

[44] R. Car and M. Parrinello, «Unified Approach for Molecular Dynamics and Density-Functional Theory,» *Physical Review Letters,* vol. 55, n° 22, pp. 2471 - 2474, 1985.

[45] R. Car and M. Parrinello, «The unified approach to density functional and molecular dynamics in real space,» *Solid State Communications,* vol. 55, n° 6, pp. 403 - 405, 1987.

[46] A. Laio and M. Parrinello, «Escaping free-energy minima,» *Proceedings of the National Academy of Sciences of the United States of America,* vol. 99, n° 20, pp. 12562 - 12566, 2002.

[47] A. Barducci, M. Bonomi and M. Parrinello, «Metadynamics,» *WIREs Computational Molecular Science,* vol. 1, n° 5, pp. 826 - 843, 2011.

[48] A. Lyakhov, A. Oganov and M. Valle, «Crystal Structure Prediction using Evolutionary Approach,» de *Modern Methods of Crystal Structure Prediction*, New York, WILEY-VCH Verlag & Co. KGaA, 2011, pp. 147 - 180.

[49] M. Born and J. R. Oppenheimer, «On the Quatum Theory of Molecules,» *Annalen der Physik,* vol. 20, n° 457 - 484, p. 389, 1927.

[50] A. Szabo and N. Ostlund, Modern Quantum Chemistry: Introduction to Advanced Electronic Structure Theory, Dover Publications, 1996.

[51] R. Martin, Electronic Structure: Basic Theory and Practical Methods, New York: Cambridge University Press, 2004.

[52] W. Kohn and L. J. Sham, «Self-Consistent Equations Including Exchange and Correlation Effects,» *Physical Review,* vol. 140, n° 4A, pp. A1133 - A1138, 1965.

[53] U. Von Barth and L. Hedin, «A local exchange-correlation potential for the spin polarized case. i,» *Journal of Physics* C*,* vol. 5, n° 13, p. 1629, 1972.

[54] S. H. Vosko, L. Wilk and M. Nusair, «Accurate spin-dependent electron liquid correlation energies for local spin density calculations: a critical analysis,» *Canadian Journal of Physics,* vol. 58, n° 8, pp. 1200 - 1211, 1980.

[55] J. P. Perdew and A. Aunger, «Self-interaction correction to density-functional approximations for many-electron systems,» *Physical Review B,* vol. 23, n° 10, pp. 5048 - 5079, 1981.

[56] J. Kohanoff, Electronic Structure Calculations for Solids and Molecules: Theory and Computational Methods, Cambridge: Cambridge University Press, 2006.

[57] M. Gell-Mann and K. A. Brueckner, «Correlation Energy of an Electron Gas at High Density,» *Physical Review,* vol. 106, n° 2, pp. 364 - 368, 1957.

[58] S. Misawa, «Ferromagnetism of an Electron Gas,» *Physical Review,* vol. 140, n° 5A, pp. A1645 - A1648, 1965.

[59] D. M. Ceperley and B. J. Alder, «Ground State of the Electron Gas by a Stochastic Method,» *Physical Review Letters,* vol. 45, n° 7, pp. 566 - 569, 1980.

[60] D. C. Langreth and M. J. Mehl, «Easily Implementable Nonlocal Exchange-Correlation Energy Functional,» *Physical Review Letters,* vol. 47, n° 6, pp. 446 - 450, 1981.

[61] A. D. Becke, «Density-functional exchange-energy approximation with correct asymptotic

behavior,» *Physical Review A,* vol. 38, n° 6, pp. 3098 - 3100, 1988.

[62] C. Lee, W. Yang and R. G. Parr, «Development of the Colle-Salvetti correlation-energy formula into a functional of the electron density,» *Physical Review B,* vol. 37, n° 2, pp. 785 - 789, 1988.

[63] J. P. Perdew, K. Burke and M. Ernzerhof, «Generalized Gradient Approximation Made Simple,» *Physical Review Letters,* vol. 77, n° 18, pp. 3865 - 3868, 996.

[64] M. C. Payne, M. P. Teter, D. C. Allan, T. A. Arias and J. D. Joannopoulos, «Iterative minimization techniques for ab initio total-energy calculations: molecular dynamics and conjugate gradients,» *Reviews of Modern Physics,* vol. 64, n° 4, pp. 1045 - 1097, 1992.

[65] W. C. Topp and J. J. Hopfield, «Chemically Motivated Pseudopotential for Sodium,» *Physical Review B,* vol. 7, n° 4, pp. 1295 - 1303, 1973.

[66] R. W. Shaw Jr. and W. A. Harrison, «Reformulation of the Screened Heine-Abarenkov Model Potential,» *Physical Review,* vol. 163, n° 3, pp. 604 - 611, 1967.

[67] G. B. Bachelet and M. Schlüter, «Relativistic norm-conserving pseudopotentials,» *Physical Review B,* vol. 25, n° 4, pp. 2103 - 2108, 1982.

[68] G. P. Kerker, «Non-singular atomic pseudopotentials for solid state applications,» *Journal of Physics C,* vol. 13, n° 9, p. L189, 1980.

[69] N. Troullier and J. L. Martins, «Efficient pseudopotentials for plane-wave calculations,» *Physical Review B,* vol. 43, n° 3, pp. 1993 - 2006, 1991.

[70] D. Vanderbilt, «Soft self-consistent pseudopotentials in a generalized eigenvalue formalism,» *Physical Review B,* vol. 41, n° 11, pp. 7892 - 7895, 1990.

# Chapter 2

## STUDY CASE: SOLID OXYGEN AT HIGH PRESSURE

### STATE OF THE ART

Oxygen is a very interesting object of study: for instance, among common diatomic molecules ($H_2$, $N_2$, $O_2$, CO, $F_2$, etc.), oxygen is the only element that can carry a magnetic moment [1]. Aside from its abundance in our Universe, its importance for many fundamental biological functions, or its role in the absorption of solar radiation inside Earth's atmosphere, oxygen exhibits a unique combination of characteristics that make it a physical object of great interest for the scientific community. Nowadays, only molecular phases of solid oxygen are known via experimental data, even at the highest pressures currently attainable in hydrostatic compression experiments. Nevertheless, inside the atmospheres of giant planets inside and outside our solar system, non-molecular oxygen could be much more abundant than the molecular phases. This hypothesis has motivated several theoretical and experimental studies aiming to get a better understanding of oxygen under extreme conditions, so that we can have a better comprehension of the processes that occur in planetary interiors.

Up to this date, six solid phases of oxygen have been established unambiguously: half of them ($\alpha$, $\beta$ and $\gamma$) exist under equilibrium vapor pressure, and the other three ($\delta$, $\varepsilon$ and $\zeta$) are obtained in the high pressure regime. Thanks to the diamond anvil cell technique [2], a new set of experimental studies of solid oxygen were performed in a pressure range of up to ~130GPa [3] and temperatures up to ~650K. As a result of those studies, a P-T diagram for solid oxygen that gathers most of their results and which is widely accepted is shown in figure 2.1.

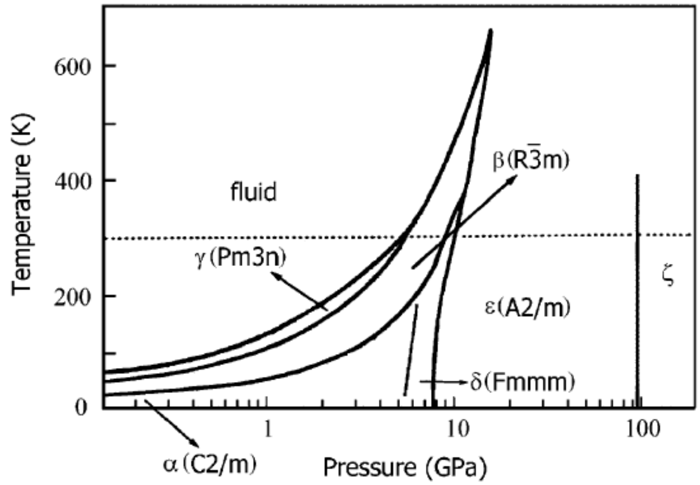

**Figure 2.1.** Phase diagram of solid oxygen. Taken from [1].

## Phases of solid oxygen in equilibrium with vapor

As mentioned, there exist three crystal structures for solid oxygen under equilibrium vapor pressure. These phases were confirmed by neutron diffraction [4], X-Ray diffraction [5] and Raman spectroscopy [6] in studies developed mostly by the middle of the twentieth century.

The $\alpha$ phase of oxygen forms at 1 atm, it is stable a very low temperature and shows an anti-ferromagnetic ordering when the temperature is below 24K [7]. This phase has a monoclinic base-centered structure of symmetry C2/m with 2 molecules per unit cell and the lattice parameters are $a$=5.403Å, $b$=3.429Å, c=5.086Å, and $\beta$=132.53°. When the temperature is increased up to 44K a new transformation of the structure of solid oxygen is carried out, reaching to the $\beta$-phase. $\beta$-oxygen is a non-magnetic element which has a rhombohedral lattice of symmetry R3m [8], its lattice parameters are: $a$=3.307Å and c=11.256Å.

Finally, the $\gamma$-phase emerges when $\beta$-oxygen transforms at 55K. Oxygen in this phase is paramagnetic and it has an eight molecule cubic cell with an orientationally disordered structure of the space group Pm3n. This phase is equivalent to the $\beta$-$N_2$ structure, with $a$=6.83Å. The structures of these three phases are shown in figure 2.2.

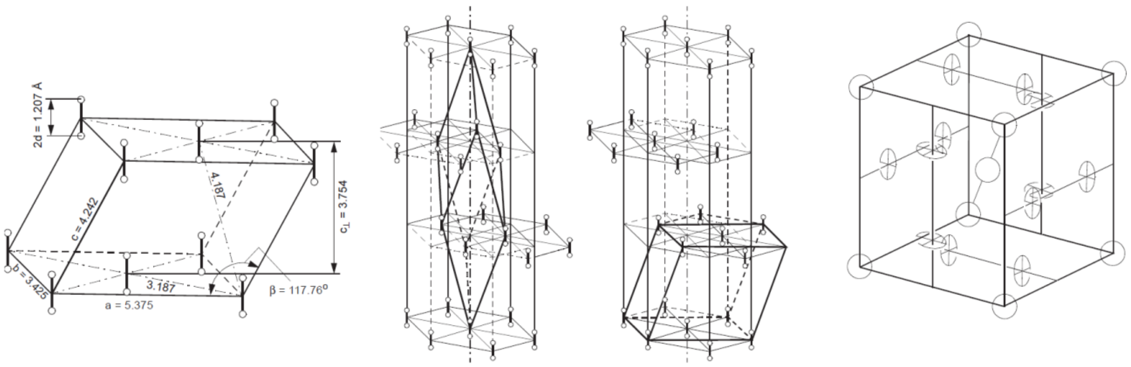

a) b-i) b-ii) c)

**Figure 2.2.** Structure of solid oxygen at a) α-phase; β-phase in b-i) rhombohedral axes and b-ii) monoclinic axes; c) γ-phase, where circles represent the orientational disorder of the molecules. Taken from [1].

## High-pressure phases of solid oxygen

According to figure 2.1, oxygen transformations below 5 or 6 GPa appear mostly as the result of a variation in temperature. From this point on, the subsequent phases of this element are strongly related to the pressure that it is submitted.

The transformation at low temperature takes place from the α-oxygen to the anti-ferromagnetic δ-phase at approximately 6GPa [9] [10] [11]. This phase was discovered by Nicol *et al.* [12] through a high-pressure Raman study, and they found what is called “orange” $O_2$ or δ-oxygen. The orthorhombic structure of this phase was determined by X-ray studies at room temperature [9]: δ-phase belongs to the space group Fmmm, with lattice parameters a=4.2151Å, b=2.9567Å, and c=6.6897Å.

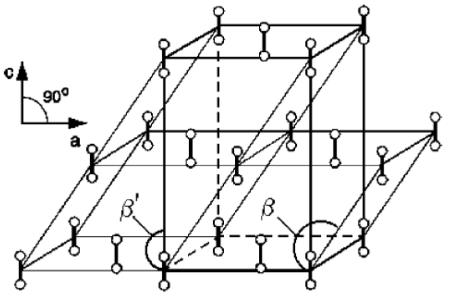

**Figure 2.3.** Structure of δ-oxygen. Taken from [1].

In the same work by Nicol *et al.* [12] another oxygen phase was described: the ε-phase. This phase appeared at 10GPa and 300K and it exhibited a visual change of the sample color from light orange to dark red: this type of change is a particularity of solid oxygen.

Several studies have been carried out in order to define the structure of the ε-phase: optical [13] [14] and X-Ray powder diffraction studies [15] [16] [17] have demonstrated that the ε-phase retains a layered structure with parallel alignment of molecules that is typical for all known oxygen structures except for γ-oxygen. A first attempt to establish the ε-phase structure, was proposed by Johnson *et al.* [18] who suggested a base-centered A2/m monoclinic unit cell made of eight molecules with the following lattice parameters: *a*=3.642Å, *b*=5.491Å, c=7.705Å, and β=116.2°. However, they were not able to determine the atomic positional and thermal parameters of the crystal structure, but according to experimental data a possible arrangement of molecules is shown in figure 4 with the separation between nearest neighbors as follows:

$$l_1 = \frac{1}{8}\sqrt{b^2 + 4c^2 + 4bc\cos\beta}\,; \qquad l_2 = \frac{1}{8}\sqrt{9b^2 + 4c^2 - 12bc\cos\beta}\,; \qquad l_3 = \frac{b}{2}$$

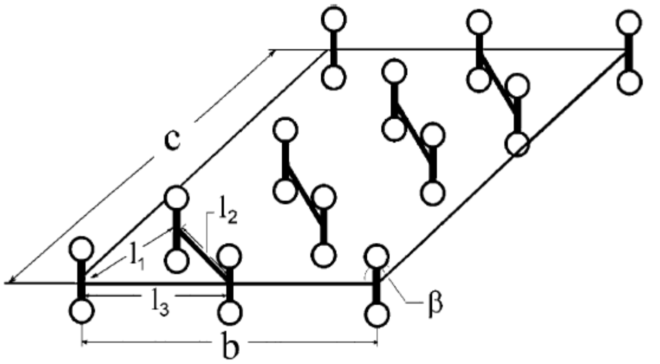

**Figure 2.4.** A possible arrangement of molecules at the bc face of the A2/m unit cell of ε-$O_2$. Taken from [1].

Later on, Gorelli *et al.* [19] suggested that ε-oxygen is not an $O_2$ molecule, but a cluster of molecules. This assumption was confirmed by X-Ray diffraction [20] [21]: ε-oxygen is an arrangement of four $O_2$ molecules that form a monoclinic C2/m structure. The ε-phase has been widely studied using different DFT functionals and it has been demonstrated that for pressures above 30GPa, DFT methods have a very good agreement with experimental results [22]. For instance, Fujihisha *et al.* [21] proposed a structural model of $\varepsilon$-$O_2$ as shown in figure 5:

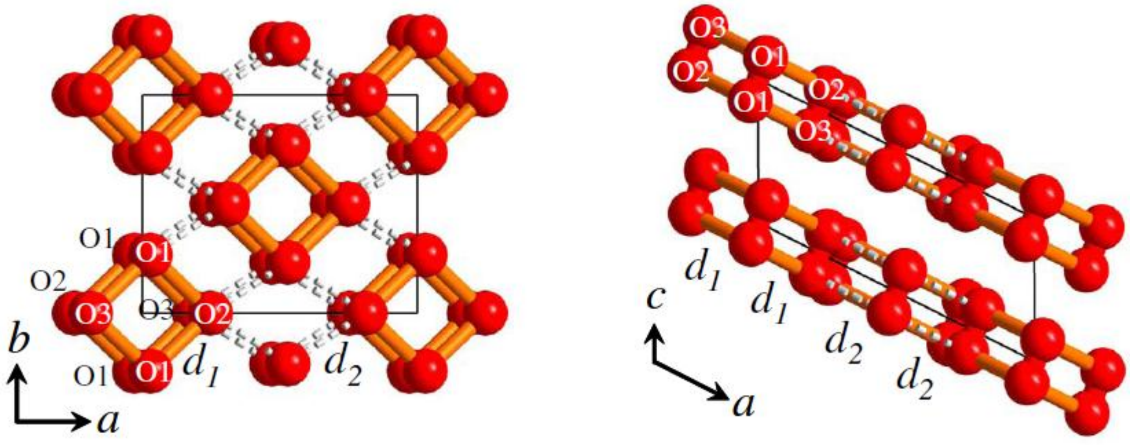

a) b)

**Figure 2.5.** Proposed structural model of $\varepsilon$-$O_2$ at 11.4 GPa viewed along a) the *c* and b) the *b* axes. Taken from [21].

The lattice parameters were defined as $a$=8.141±0.002Å, $b$=5.747±0.00Å, $c$=3.773±0.001Å, and $\beta$=117.07±0.01°, therefore its volume is 157.18±0.04Å$^3$. The atomic Wyckoff positions (O1, O2 and O3) are defined as follows:

- O1: (0.029±0.001, 0.266±0.001, 0.177±0.001)
- O2: (0.247±0.001, 0, 0.177±0.001)
- O3: (0.190±0.001, 0, -0.177±0.001)

By connecting the nearest intermolecular distance $d_1$=2.34Å (solid orange bars in figure 2.5), a cluster made up of 4 molecules emerges. This distance is significantly shorter when it is compared with the intercluster distance, $d_2$=2.34Å (dashed lines in figure 2.5), therefore the arrangement can be interpreted as an $O_8$ cluster, which is consistent with the results with theoretical and optical studies [19] [23] [24] [25].

A more recent study [26] has proposed a new phase diagram for solid oxygen, where the single $\varepsilon$-phase should be replaced with two phases $\varepsilon_1$-$O_2$ and $\varepsilon_2$-$O_2$: the first one is a local singlet spin

1 liquid, while the second one is a regular, Peierls band insulator – separated by a first order phase transition near 20 GPa.

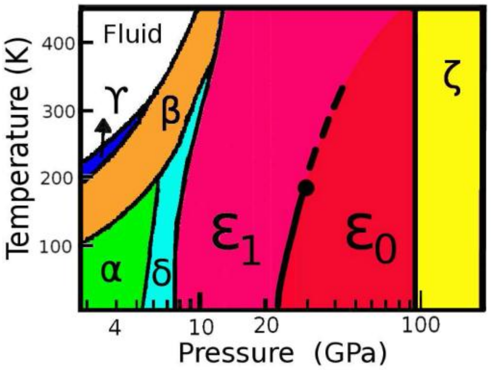

**Figure 2.6.** Proposed new phase diagram of oxygen. Taken from [26].

A room temperature X-Ray study revealed that the ε-phase remains stable up to 96 GPa, when it suffers another transformation and becomes metallic in the ζ-phase [15]. This transition, from insulator to a metallic phase is unique, but to date remains unexplained. The lack of information of the atomic positions inside the unit cell in the ζ phase has made that the ε-ζ phase transition is still a matter of discussion. But this phase is not only metallic: a theoretical study predicted that at 0.6K and 100GPa, the solid oxygen turns into a superconductor [27], and this result was later confirmed experimentally [3].

The scenario for even higher pressures is also intriguing, given the uncertainty regarding the question if the pressure applied to solid oxygen will lead to a molecular dissociation or further association: theoretical studies now suggest that even in the terapascal (TPa) regime oxygen remains molecular [28], while other diatomic molecules have suffered a molecular dissociation at much lower pressures [29] [30] [31] [32] [33]. Regarding the experimental findings mentioned before, until now, the crystal structure of ζ-oxygen is still undetermined: theoretical studies have proposed several candidates such as:

- C2mm [34]
- I41/acd [35]
- 63/mmc-4, C2/m-2, C2/m-8 and R3m [28]. The R3m structure also exhibits a superconductor behavior at 1.8 TPa and 0.6 – 2.1K.

- C2/c and C2/m [27] [36]. This last structure shows a good agreement with the results of X-Ray diffraction experiments [3] [37].

This was the starting point for the present study: we extrapolated what might be a suitable density for solid oxygen structures in a range of pressure starting from 350 GPa going up to 3500 GPa. Then, we performed a structural search looking for post-ζ-oxygen phases, in particular non-molecular. At the time when we started our work we were unaware of the fact that other theoretical studies had already predicted non-molecular phases to appear only above 2000 GPa [28], however, our pressures of interest do not overlap entirely with those in the mentioned study and they can still shed some light about the nature of the molecular oxygen bonding at high pressures.

## METHODOLOGY

With the results reported in several theoretical and experimental studies, we first estimated the initial densities that our samples should have in order to generate initial pressures that were near 350 GPa and higher, up to 3500 GPa. With this information triclinic structures were randomly generated, which had up to four atoms per unit cell. We chose a set of cell lengths and angles generated randomly and later rescaled them with the estimated volume at the target pressure [38], but in order to avoid needle-like or other very distorted shapes, the crystal lattice was generated by initially selecting three random numbers between 0.5 and 1.5 as the "lengths" of the cell-vectors (at this stage we haven´t assigned units to these lengths[1]) and three random cell angles between 40° and 140°, before scaling the size of this cell-shape to a physically meaningful value.

We generated a thousand samples for each pressure, where each sample started with a different random configuration and was later relaxed until it reached a local minimum inside the free-energy landscape. It has been shown several times that by using this method, the stable structures, which are the ones with the lowest enthalpy, can be found and characterized [28] [29] [39] [40] [41] [42] [43] [44] [45].

---

[1] The unit of length will be evident as soon as we scale the randomly generated cell, since its final volume will coincide with a pre-established target volume in $\text{bohr}^3$.

For each of the structures generated randomly, we performed density functional electronic structure calculations using the pw.x code from the Quantum ESPRESSO package [46]. We calculated both energy and forces on the atoms, then the atomic positions and cell parameters were slightly displaced following a direction determined by the forces and the stresses acting on the system. These displacements occurred several times, until a situation where the forces acting on the atoms were very close to zero was reached, meaning that the structure was at equilibrium. Finally we compared the structures in order to find the ones with the lowest enthalpy and construct an equation of state of oxygen at high pressure, piece by piece, showing only the stable structures in their respective regions of stability.

## TECHNICAL DETAILS

For the calculations we used the Perdew-Burke-Ernzerhof (PBE) generalized gradient (GGA) exchange-correlation functional [47], with ultra-soft pseudo-potentials[2] and the Brillouin-Zone integrations were approximated using the method of Monkhorst and Pack [48].

Before starting, we performed some energy convergence tests in order to determine the optimal k-point grid and the plane-wave kinetic energy cutoff. Considering the highest pressure that we reached in this study, both an $O_2$ and an $O_4$ structure at 3500GPa were used as a reference for the energy and k-point convergence tests, because these configurations have the smallest volumes, which in turn become the biggest in the reciprocal space. Therefore, by sampling correctly these structures the same criteria can be extended safely to the structures at lower pressure. The convergence plots for both parameters are shown in figures 2.7 and 2.8. Due to the accuracy of the methods involved we are interested in differences in energy that are higher than 5meV, keeping this in mind we concluded that it was better to use a k-point grid of 8x8x8 and a plane-wave kinetic energy cutoff of 60Ry.

---

[2] We used the pseudopotentials O.pbe-rrkjus.UPF from the Quantum ESPRESSO pseudopotential data base: http://www.quantum-espresso.org/pseudopotentials

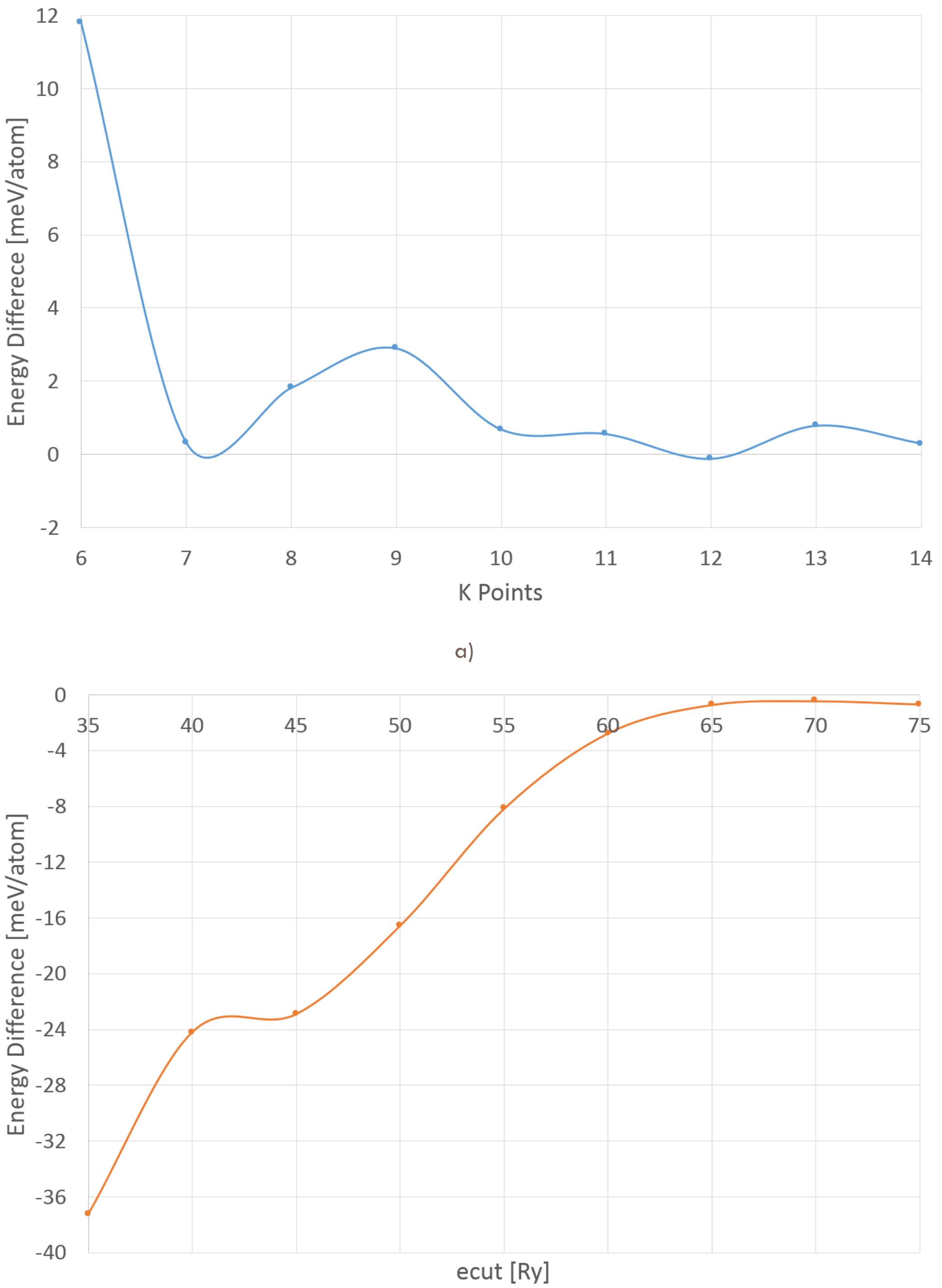

a)

b)

**Figure 2.7.** Energy convergence for an $O_2$ structure at 3500GPa. Varying a) k-points grid and b) plane wave kinetic cutoff.

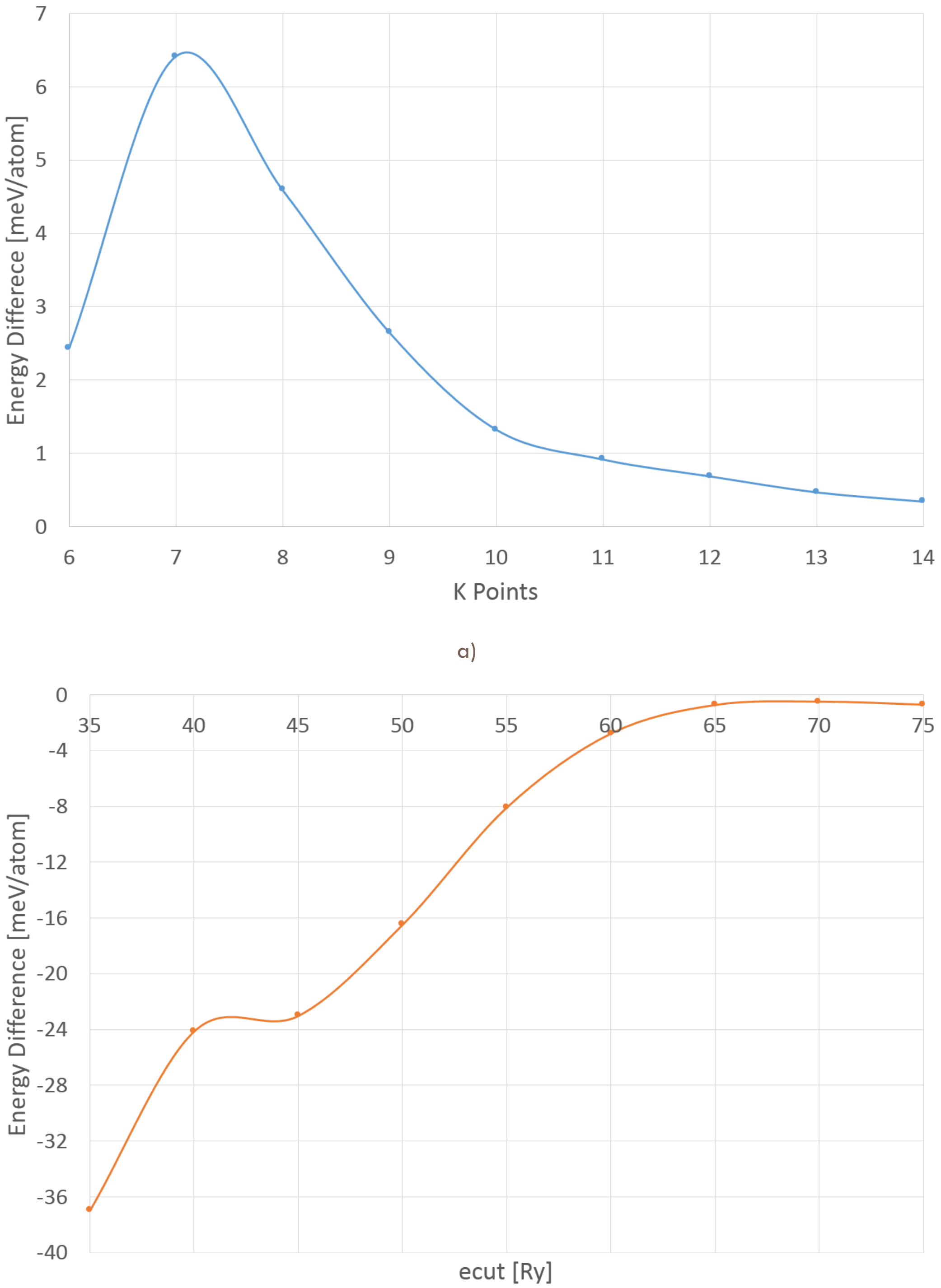

a)

b)

**Figure 2.8.** Energy convergence for an $O_4$ structure at 3500GPa. Varying a) k-points grid and b) plane wave kinetic cutoff.

We performed a calculation for each system generating a thousand of samples at each pressure included in this study. Now, given the stochastic approach of the structural search method being used, we first run a loose calculation in order to obtain a relaxed cell closer to the final one. Once we found this intermediate structure, we performed a second more accurate relaxation according to the results of the energy convergence test shown before. Thus, we generated two input files with the following parameters:

**Table 2.1.** Parameters used in the Quantum ESPRESSO input files for oxygen structural search.

| Parameter | First calculation | Second calculation |
|---|---|---|
| **ecutwfc** | 25 | 60 |
| **conv_thr** | 5D-7 | 1D-10 |
| **mixing_beta** | 0.48D0 | 0.6D0 |
| **trust_radius_ini** | 2D-1 | 5D-2 |
| **trust_radius_max** | 6D-1 | 5D-1 |
| **trust_radius_min** | 1D-8 | 1D-10 |
| **cell_factor** | 3.2 | 1.8 |
| **press_conv_thr** | 0.5 | 1.0 |
| **k_points** | 4 4 4 | 8 8 8 |

## RESULTS

### Molecular Solid Oxygen

Every set of a thousand samples converged into a reduced number of local minima, and according to the high number of repetitions observed we can say with confidence that there are no other energy minima available in each energy landscape studied. However, it can be seen that the reported minima are always slightly less than one thousand due to the fact that some starting configurations did not performed well during the relaxation and the DFT code crashed. Since we are performing a structural search for pressures that are higher than zero, our comparison between structures is not done with the total energy of the systems, but with their enthalpy. The behavior of the enthalpy at different pressures for the $O_2$ and $O_4$ molecules is shown in figures 2.9 and 2.10, and the amount of structures that converged into a local minima are in table 2.2 and 2.3.

**Table 2.2.** $O_2$ structures that converged into a local minima.

| Pressure [TPa] | Lowest Enthalpy | Other local minima | Pressure [TPa] | Lowest Enthalpy | Other local minima | Pressure [TPa] | Lowest Enthalpy | Other local minima |
|---|---|---|---|---|---|---|---|---|
| 0.35 | 220 | 630 | 0.40 | 478 | 465 | 0.45 | 451 | 469 |
| 0.50 | 465 | 469 | 0.55 | 121 | 786 | 0.60 | 143 | 744 |
| 0.65 | 219 | 685 | 0.70 | 388 | 487 | 0.80 | 156 | 565 |
| 0.90 | 186 | 620 | 1.00 | 145 | 669 | 1.10 | 162 | 575 |
| 1.20 | 164 | 642 | 1.40 | 184 | 539 | 1.60 | 141 | 554 |
| 1.80 | 130 | 551 | 2.00 | 160 | 520 | 2.20 | 158 | 610 |
| 2.40 | 138 | 560 | 2.60 | 82 | 627 | 2.80 | 109 | 602 |
| 3.00 | 139 | 545 | 3.20 | 141 | 582 | 3.50 | 142 | 558 |

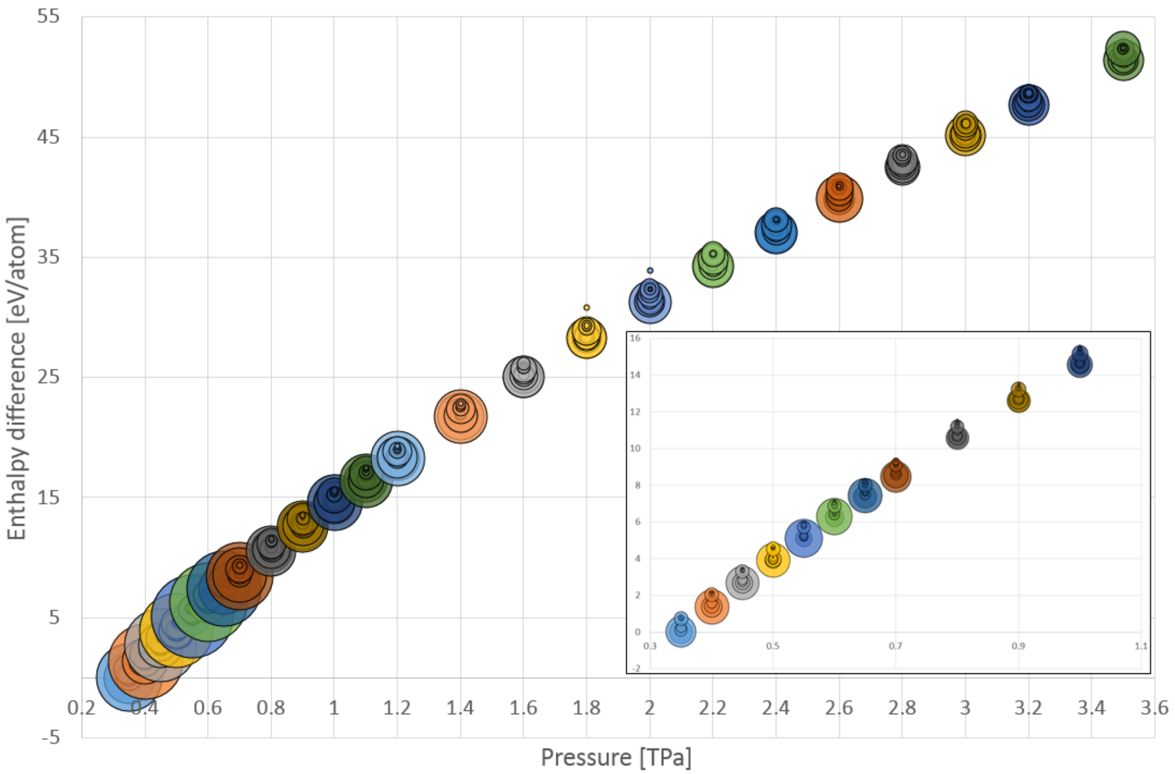

**Figure 2.9.** Enthalpy variation for $O_2$ at pressures from 0.35 to 3.5 TPa. For each pressure, the circle size is proportional to the number of initial structures that converged to the enthalpy at the center of the circle.

**Table 2.3.** $O_4$ structures that converged into a local minima.

| Pressure [TPa] | Lowest Enthalpy | Other local minima |
|---|---|---|
| 0.50 | 153 | 739 |
| 0.70 | 122 | 793 |
| 0.90 | 117 | 757 |
| 1.10 | 32 | 862 |
| 1.30 | 28 | 846 |
| 1.50 | 104 | 741 |
| 1.70 | 88 | 793 |
| 1.90 | 121 | 720 |
| 2.10 | 107 | 690 |
| 2.30 | 153 | 592 |
| 2.50 | 37 | 726 |
| 2.70 | 35 | 638 |
| 2.90 | 181 | 493 |
| 3.10 | 138 | 538 |
| 3.30 | 166 | 534 |
| 3.50 | 137 | 552 |

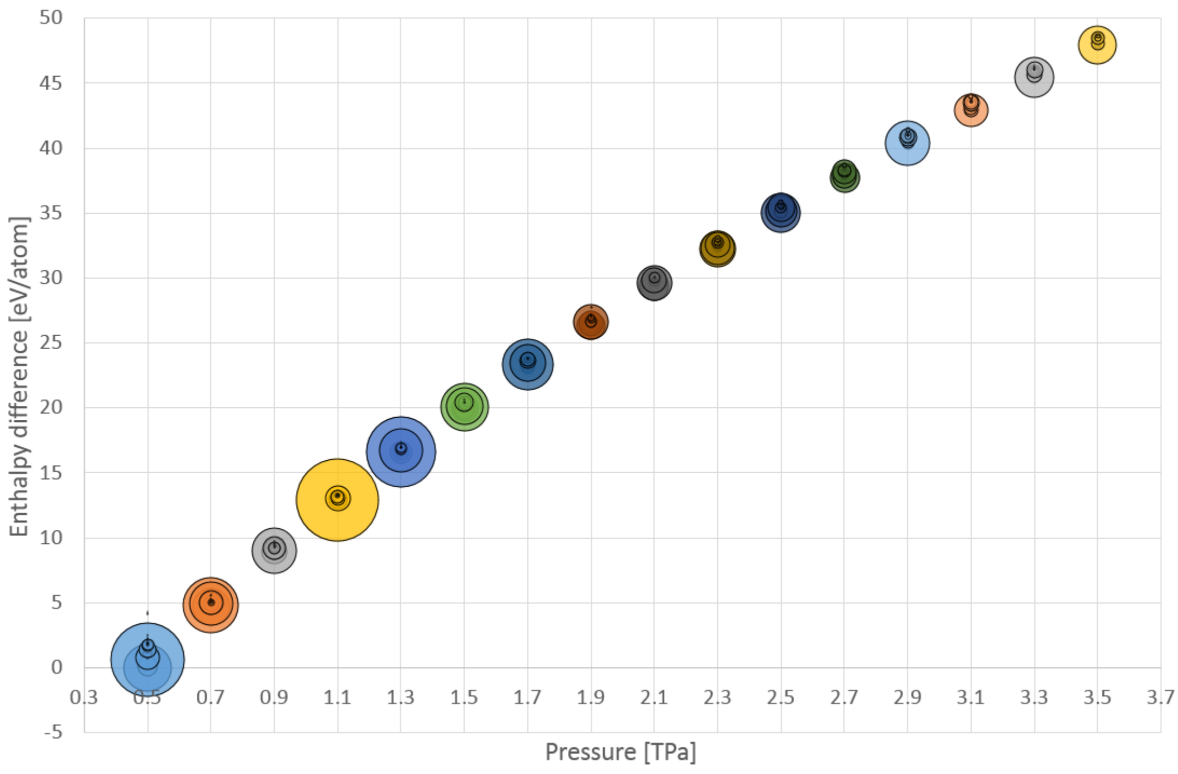

**Figure 2.10.** Enthalpy variation for $O_4$ at pressures from 0.5 to 3.5 TPa. For each pressure, the circle size is proportional to the number of initial structures that converged to the enthalpy at the center of the circle.

Once the global enthalpy was determined, we selected the best crystal structure, i.e. the one with the lowest enthalpy among all, at each pressure studied. However, the final primitive cells were difficult to identify; therefore, we used the package FINDSYM [49] from the ISOTROPY Software Suite in order to find conventional cell equivalents, with higher symmetries that made further analysis easier. We found three different symmetry groups for $O_2$: triclinic (P-1), monoclinic (C2/m) and orthorhombic (Cmcm); for $O_4$ we found orthorhombic (Cmma, Pnma and Cmcm) and monoclinic (C2/m and P2/c). Cell parameters for both systems are detailed in table 2.4 and 2.5, for $O_2$ and $O_4$. The equivalent structures for $O_2$ and $O_4$, are shown in figure 2.11 and 2.12, respectively. Refer to the end of this chapter for the conclusions on these findings.

**Table 2.4.** Cell parameters for the best structures found for $O_2$ at pressures from 0.35 to 3.5 TPa.

| Pressure [TPa] | Space Group | Lattice Parameters [a.u.; °] | Atomic Coordinates (Fractional) |
|---|---|---|---|
| 0.35 | P-1 | a=3.6555 b=3.6681 c=5.5635<br>α=108.875 β=90.889 γ=118.922 | O1 -0.0725 -0.1403 -0.2132<br>Wyckoff letter: i |
| 0.40 | P-1 | a=3.6042 b=3.6168 c=5.4961<br>α=108.774 β=91.007 γ=118.839 | O1 0.0732 0.1409 0.2146<br>Wyckoff letter: i |
| 0.45 | C2/m | a=7.1722 b=3.6901 c=4.1597<br>α=γ=90.000 β=95.534 | O1 0.1061 0.0000 0.2163<br>Wyckoff letter: i |
| 0.50 | C2/m | a=7.0833 b=3.6413 c=4.1262<br>α=γ=90.000 β=95.326 | O1 -0.1060 0.0000 0.2183<br>Wyckoff letter: i |
| 0.55 | Cmcm | a=6.3708 b=4.2501 c=3.7139<br>α=β=γ=90.000 | O1 0.0000 -0.1849 0.0000<br>Wyckoff letter: c |
| 0.60 | Cmcm | a=6.3088 b=4.1897 c=3.7007<br>α=β=γ=90.000 | O1 0.0000 -0.1860 0.0000<br>Wyckoff letter: c |
| 0.65 | Cmcm | a=6.2522 b=4.1333 c=3.6890<br>α=β=γ=90.000 | O1 0.0000 -0.1871 0.0000<br>Wyckoff letter: c |
| 0.70 | Cmcm | a=6.1999 b=4.0817 c=3.6774<br>α=β=γ=90.000 | O1 0.0000 -0.1881 0.0000<br>Wyckoff letter: c |
| 0.80 | Cmcm | a=6.1058 b=3.9935 c=3.6548<br>α=β=γ=90.000 | O1 0.0000 -0.1897 0.0000<br>Wyckoff letter: c |
| 0.90 | Cmcm | a=6.0222 b=3.9148 c=3.6337<br>α=β=γ=90.000 | O1 0.0000 -0.1914 0.0000<br>Wyckoff letter: c |
| 1.00 | Cmcm | a=5.9465 b=3.8463 c=3.6118<br>α=β=γ=90.000 | O1 0.0000 0.1929 0.0000<br>Wyckoff letter: c |
| 1.10 | Cmcm | a=5.8789 b=3.7903 c=3.5908<br>α=β=γ=90.000 | O1 0.0000 -0.1941 0.0000<br>Wyckoff letter: c |

**Table 2.4.** Cell parameters for the best structures found for $O_2$ at pressures from 0.35 to 3.5 TPa. (Cont.)

| Pressure [TPa] | Space Group | Lattice Parameters [a.u.; °] | Atomic Coordinates (Fractional) |
|---|---|---|---|
| 1.20 | Cmcm | a=5.8162 b=3.7376 c=3.5697<br>$\alpha=\beta=\gamma=90.000$ | O1 0.0000 0.1954 0.0000<br>Wyckoff letter: c |
| 1.40 | Cmcm | a=5.7061 b=3.6507 c=3.5301<br>$\alpha=\beta=\gamma=90.000$ | O1 0.0000 0.1975 0.0000<br>Wyckoff letter: c |
| 1.60 | Cmcm | a=5.6108 b=3.5767 c=3.4944<br>$\alpha=\beta=\gamma=90.000$ | O1 0.0000 -0.1995 0.0000<br>Wyckoff letter: c |
| 1.80 | Cmcm | a=5.5271 b=3.5147 c=3.4603<br>$\alpha=\beta=\gamma=90.000$ | O1 0.0000 -0.2013 0.0000<br>Wyckoff letter: c |
| 2.00 | Cmcm | a=5.4526 b=3.4608 c=3.4287<br>$\alpha=\beta=\gamma=90.000$ | O1 0.0000 -0.2030 0.0000<br>Wyckoff letter: c |
| 2.20 | Cmcm | a=5.3851 b=3.4140 c=3.3986<br>$\alpha=\beta=\gamma=90.000$ | O1 0.0000 -0.2046 0.0000<br>Wyckoff letter: c |
| 2.40 | Cmcm | a=5.3239 b=3.3719 c=3.3705<br>$\alpha=\beta=\gamma=90.000$ | O1 0.0000 -0.2060 0.0000<br>Wyckoff letter: c |
| 2.60 | Cmcm | a=5.2674 b=3.3339 c=3.3442<br>$\alpha=\beta=\gamma=90.000$ | O1 0.0000 -0.2073 0.0000<br>Wyckoff letter: c |
| 2.80 | Cmcm | a=5.2155 b=3.2994 c=3.3139<br>$\alpha=\beta=\gamma=90.000$ | O1 0.0000 -0.2087 0.0000<br>Wyckoff letter: c |
| 3.00 | Cmcm | a=5.1673 b=3.275 c=3.2958<br>$\alpha=\beta=\gamma=90.000$ | O1 0.0000 -0.2099 0.0000<br>Wyckoff letter: c |
| 3.20 | Cmcm | a=5.1224 b=3.2382 c=3.2736<br>$\alpha=\beta=\gamma=90.000$ | O1 0.0000 -0.2110 0.0000<br>Wyckoff letter: c |
| 3.50 | Cmcm | a=5.0602 b=3.1981 c=3.2423<br>$\alpha=\beta=\gamma=90.000$ | O1 0.0000 0.2127 0.0000<br>Wyckoff letter: c |

**Table 2.5.** Cell parameters for the best structures found for $O_4$ at pressures from 0.5 to 3.5 TPa.

| Pressure [TPa] | Space Group | Lattice Parameters [a.u.; °] | Atomic Coordinates (Fractional) |
|---|---|---|---|
| 0.50 | Cmma | a=3.9766 b=9.9741 c=5.3771<br>$\alpha=\beta=\gamma=90.000$ | O1 0.0000 -0.3584 -0.2435<br>Wyckoff letter: m |
| 0.70 | Cmma | a=3.7942 b=9.6729 c=5.2284<br>$\alpha=\beta=\gamma=90.000$ | O1 0.0000 -0.3600 -0.2470<br>Wyckoff letter: m |
| 0.90 | Cmma | a=9.4446 b=3.6895 c=5.0773<br>$\alpha=\beta=\gamma=90.000$ | O1 0.3888 0.0000 0.2464<br>Wyckoff letter: n |
| 1.10 | Cmma | a=3.5950 b=9.2593 c=4.9696<br>$\alpha=\beta=\gamma=90.000$ | O1 0.0000 -0.3621 0.2475<br>Wyckoff letter: m |

**Table 2.5.** Cell parameters for the best structures found for $O_4$ at pressures from 0.5 to 3.5 TPa. (Cont.)

| Pressure [TPa] | Space Group | Lattice Parameters [a.u.; ª] | Atomic Coordinates (Fractional) |
|---|---|---|---|
| 1.30 | Cmma | a=3.5205 b=9.1041 c=4.8735<br>$\alpha=\beta=\gamma=90.000$ | O1 0.0000 -0.1371 -0.2485<br>Wyckoff letter: m |
| 1.50 | Cmcm | a=5.6570 b=3.6146 c=3.5119<br>$\alpha=\beta=\gamma=90.000$ | O1 0.0000 -0.1983 0.0000<br>Wyckoff letter: c |
| 1.70 | Cmcm | a=5.5678 b=3.5466 c=3.4772<br>$\alpha=\beta=\gamma=90.000$ | O1 0.0000 -0.2001 0.0000<br>Wyckoff letter: c |
| 1.90 | Cmcm | a=5.4894 b=3.4879 c=3.4447<br>$\alpha=\beta=\gamma=90.000$ | O1 0.0000 -0.2021 0.0000<br>Wyckoff letter: c |
| 2.10 | Cmcm | a=5.4186 b=3.4376 c=3.4138<br>$\alpha=\beta=\gamma=90.000$ | O1 0.0000 0.2037 0.0000<br>Wyckoff letter: c |
| 2.30 | Cmcm | a=5.3545 b=3.3930 c=3.3849<br>$\alpha=\beta=\gamma=90.000$ | O1 0.0000 0.2052 0.0000<br>Wyckoff letter: c |
| 2.50 | Cmcm | a=5.2959 b=3.3530 c=3.3576<br>$\alpha=\beta=\gamma=90.000$ | O1 0.0000 0.2067 0.0000<br>Wyckoff letter: c |
| 2.70 | Cmcm | a=5.2419 b=3.3168 c=3.3320<br>$\alpha=\beta=\gamma=90.000$ | O1 0.0000 0.2080 0.0000<br>Wyckoff letter: c |
| 2.90 | Cmcm | a=5.1919 b=3.2837 c=3.3078<br>$\alpha=\beta=\gamma=90.000$ | O1 0.0000 0.2093 0.0000<br>Wyckoff letter: c |
| 3.10 | Cmcm | a=5.1454 b=3.2531 c=3.2849<br>$\alpha=\beta=\gamma=90.000$ | O1 0.0000 0.2105 0.0000<br>Wyckoff letter: c |
| 3.30 | Cmcm | a=5.1020 b=3.2249 c=3.2633<br>$\alpha=\beta=\gamma=90.000$ | O1 0.0000 -0.2116 0.0000<br>Wyckoff letter: c |
| 3.50 | Cmcm | a=5.0622 b=3.1977 c=3.2423<br>$\alpha=\beta=\gamma=90.000$ | O1 0.0000 0.2128 0.0000<br>Wyckoff letter: c |

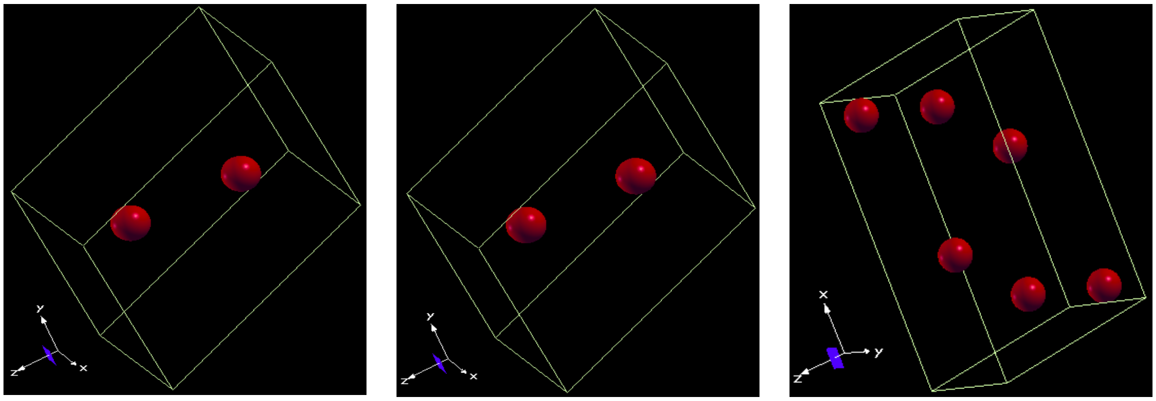

0.35 TPa
0.40 TPa
0.45 TPa

**Figure 2.11.** Best structures for $O_2$ at pressures from 0.35 to 3.5 TPa.

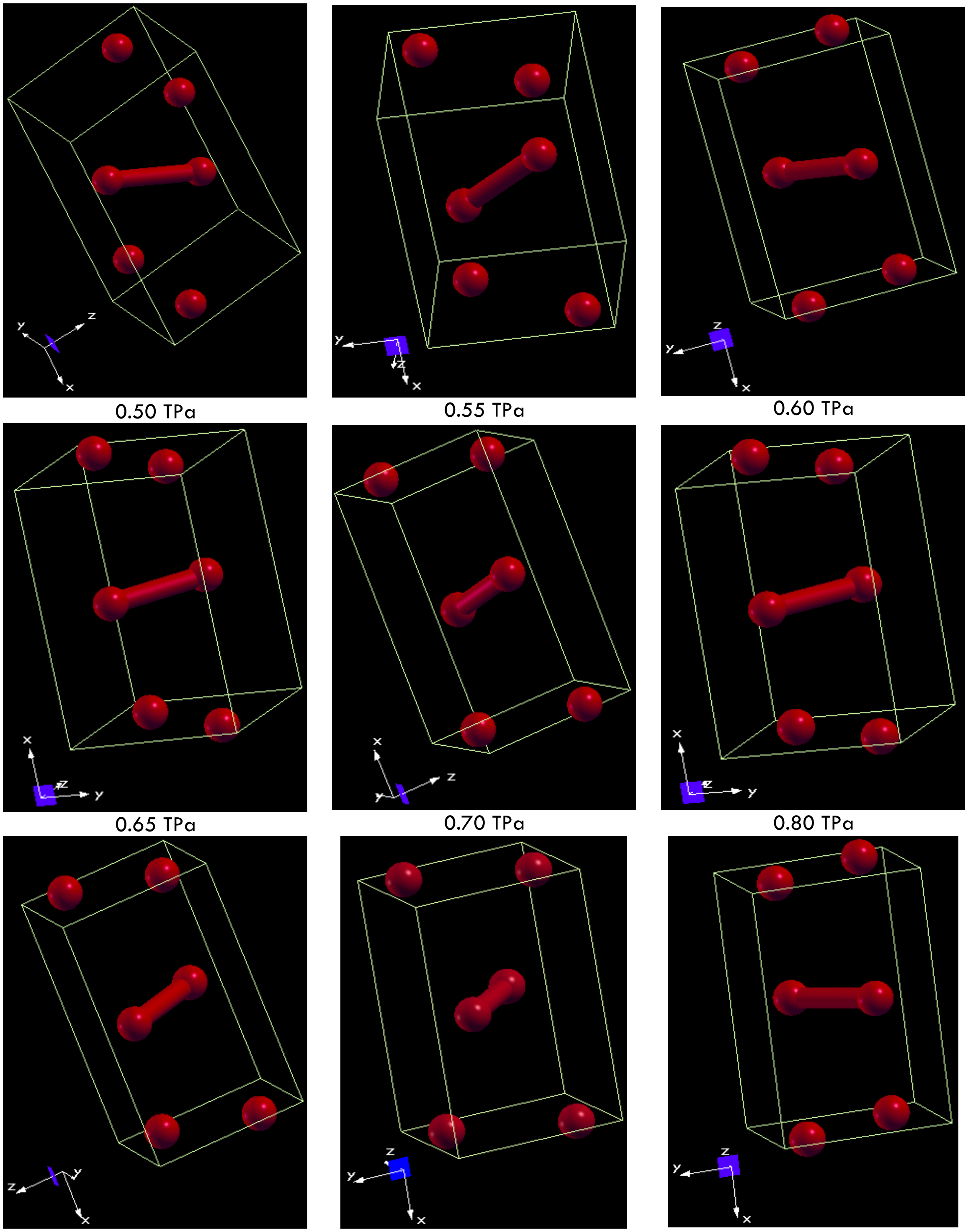

0.50 TPa
0.55 TPa
0.60 TPa
0.65 TPa
0.70 TPa
0.80 TPa
0.90 TPa
1.00 TPa
1.10 TPa

**Figure 2.11.** Best structures for $O_2$ at pressures from 0.35 to 3.5 TPa. (Cont.)

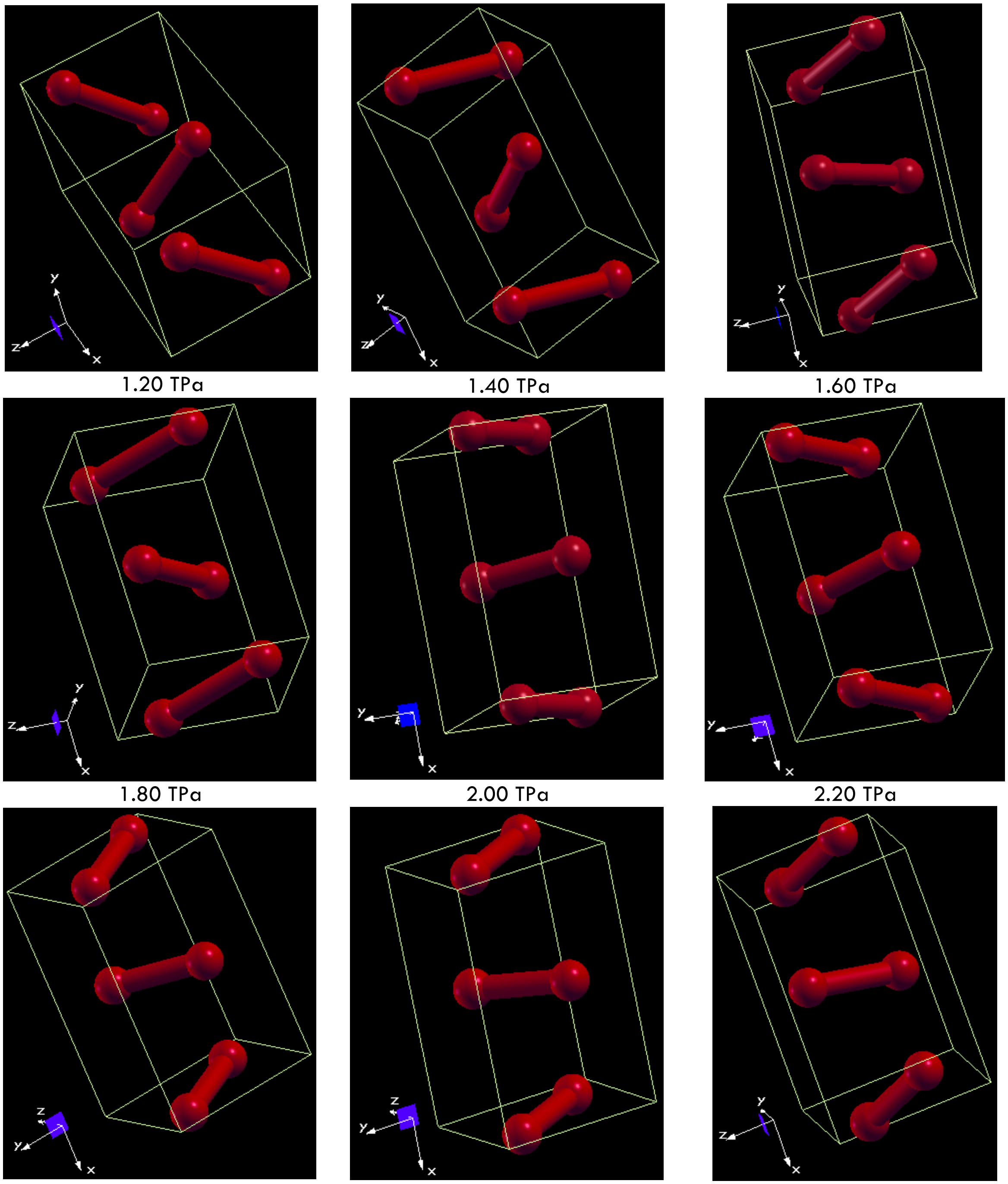

1.20 TPa 1.40 TPa 1.60 TPa

1.80 TPa 2.00 TPa 2.20 TPa

2.40 TPa 2.60 TPa 2.80 TPa

**Figure 2.11.** Best structures for $O_2$ at pressures from 0.35 to 3.5 TPa. (Cont.)

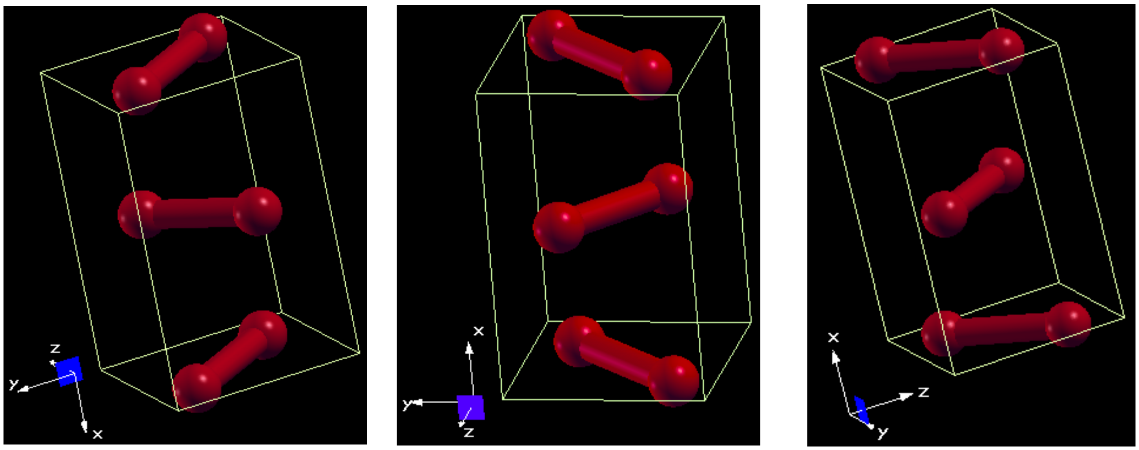

3.00 TPa 3.20 TPa 3.50 TPa

**Figure 2.11.** Best structures for $O_2$ at pressures from 0.35 to 3.5 TPa. (Cont.)

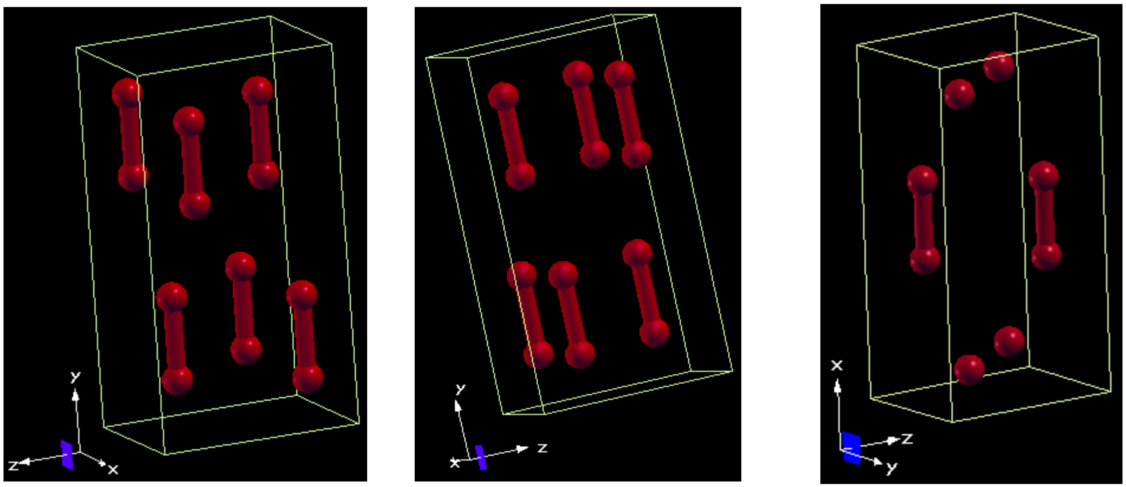

0.50 TPa 0.70 TPa 0.90 TPa

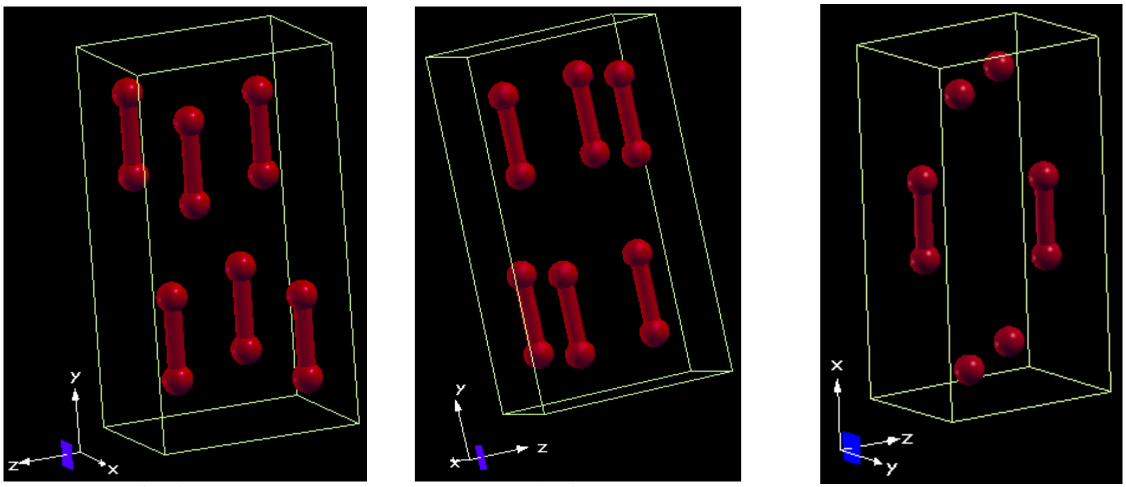

0.50 TPa 0.70 TPa 0.90 TPa

**Figure 2.12.** Best structures for $O_4$ at pressures from 0.5 to 3.5 TPa.

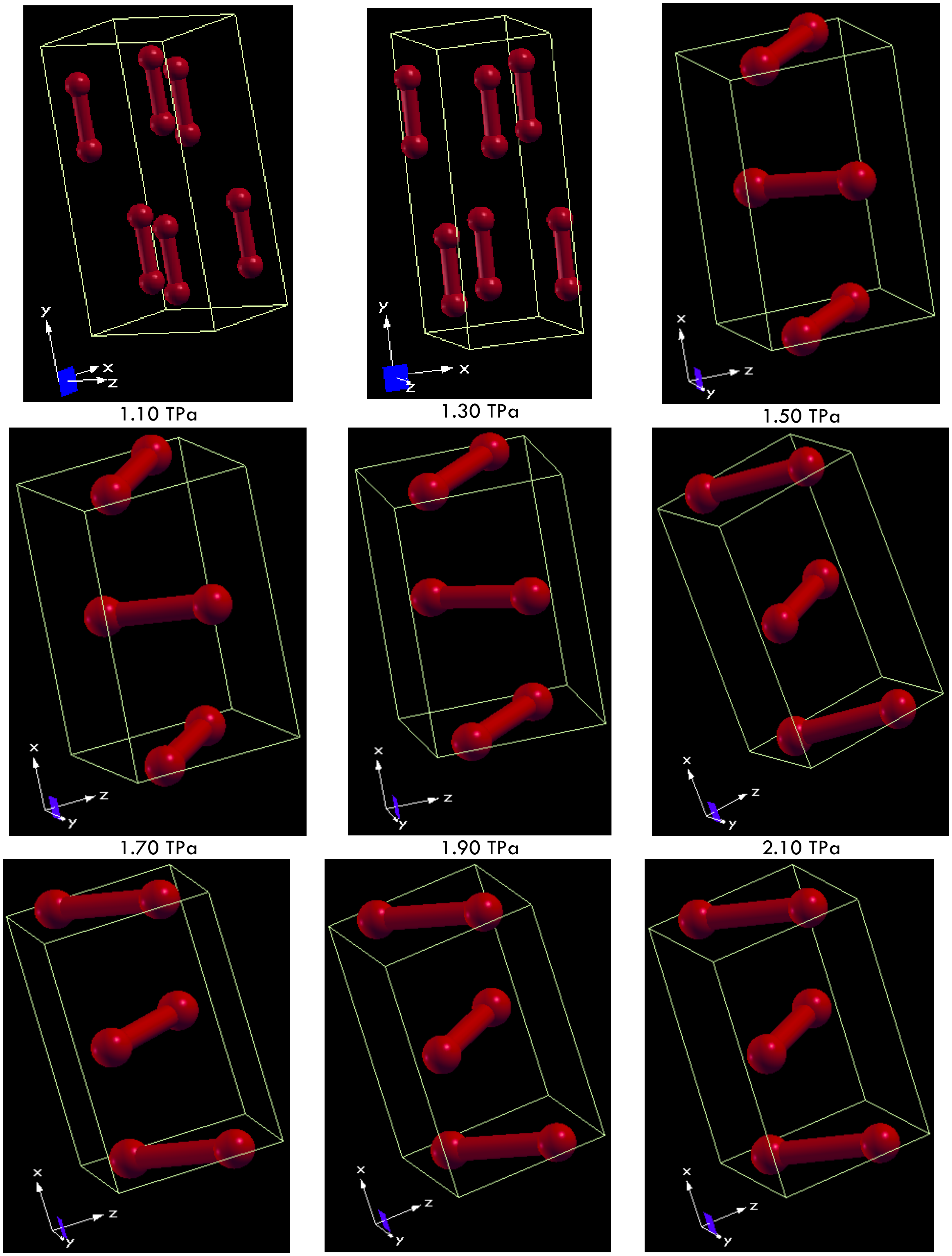

1.10 TPa 1.30 TPa 1.50 TPa

1.70 TPa 1.90 TPa 2.10 TPa

2.30 TPa 2.50 TPa 2.70 TPa

**Figure 2.12.** Best structures for $O_4$ at pressures from 0.5 to 3.5 TPa. (Cont.)

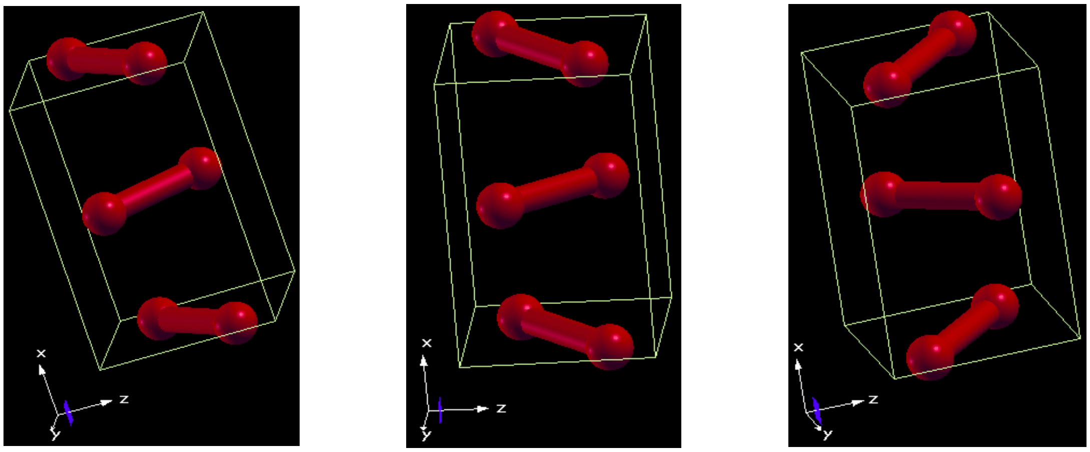

2.90 TPa 3.10 TPa 3.30 TPa

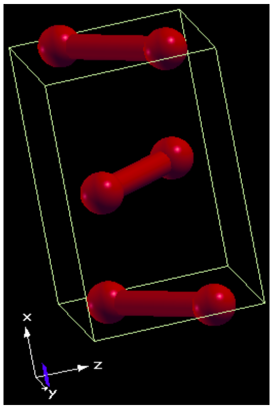

3.50 TPa

**Figure 2.12.** Best structures for $O_4$ at pressures from 0.5 to 3.5 TPa. (Cont.)

With the results obtained we found that as the pressure applied on the system increases, the unit-cell volume decreases but each time the reduction of the volume becomes more difficult, as expected. This evolution is shown in figure 2.13.

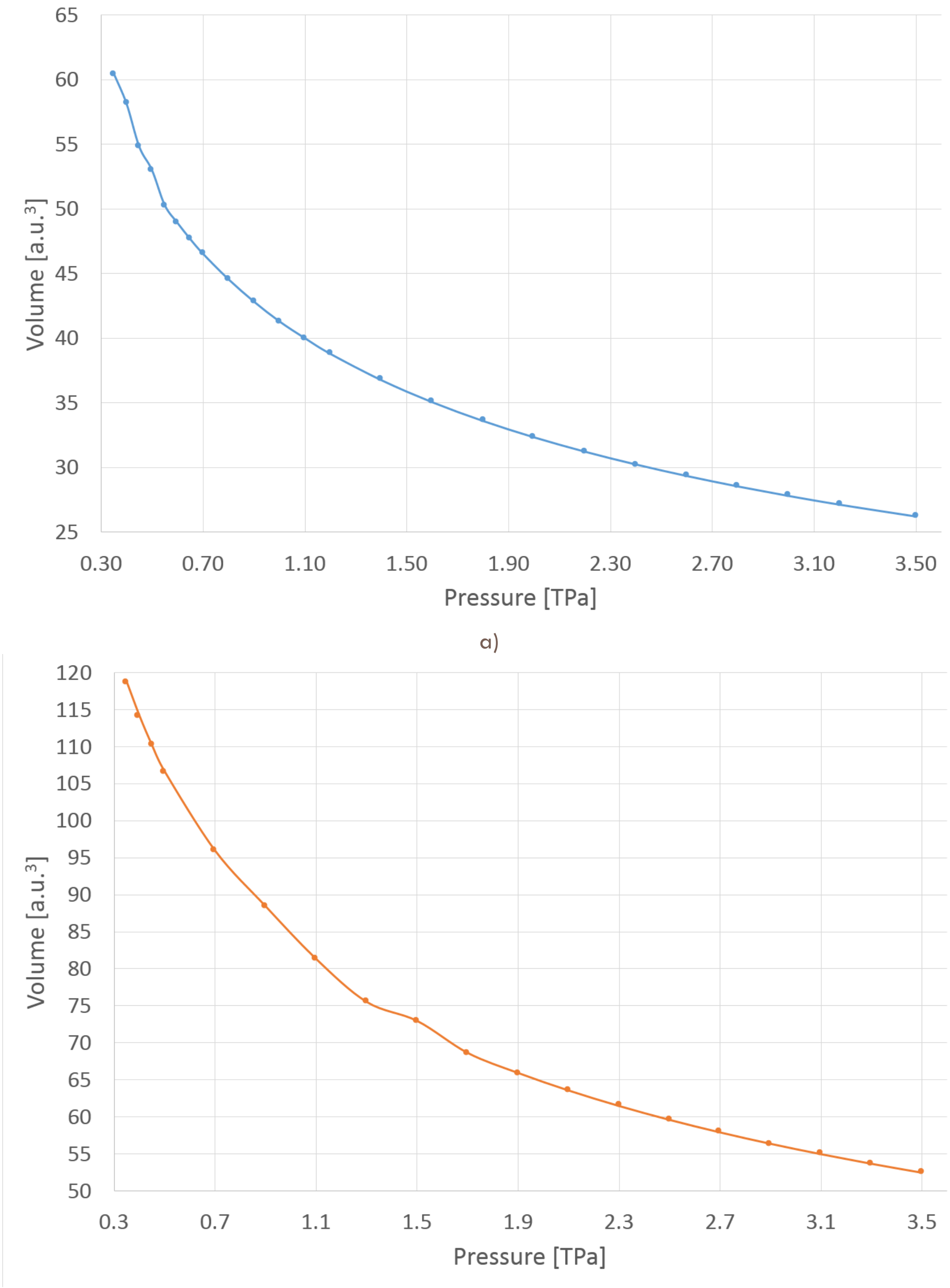

a)

b)

**Figure 2.13.** Volume evolution while pressure increases. a) $O_2$ system. b) $O_4$ system.

As a consequence of the constant fall off of the volume, we observed that distances between first and second neighbors also decrease with pressure, as shown in figure 2.14.

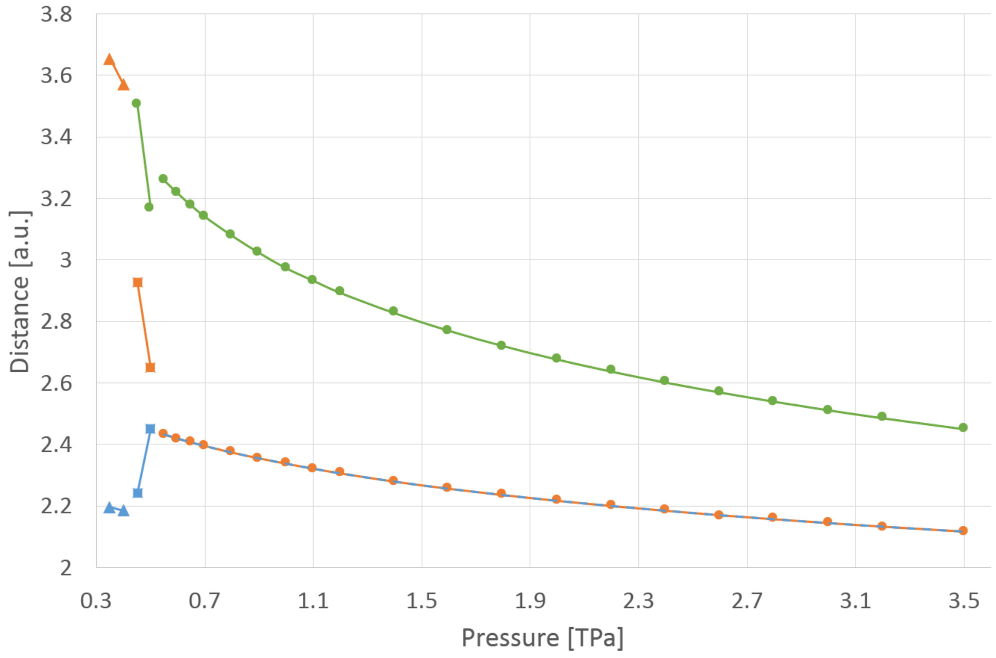

a)

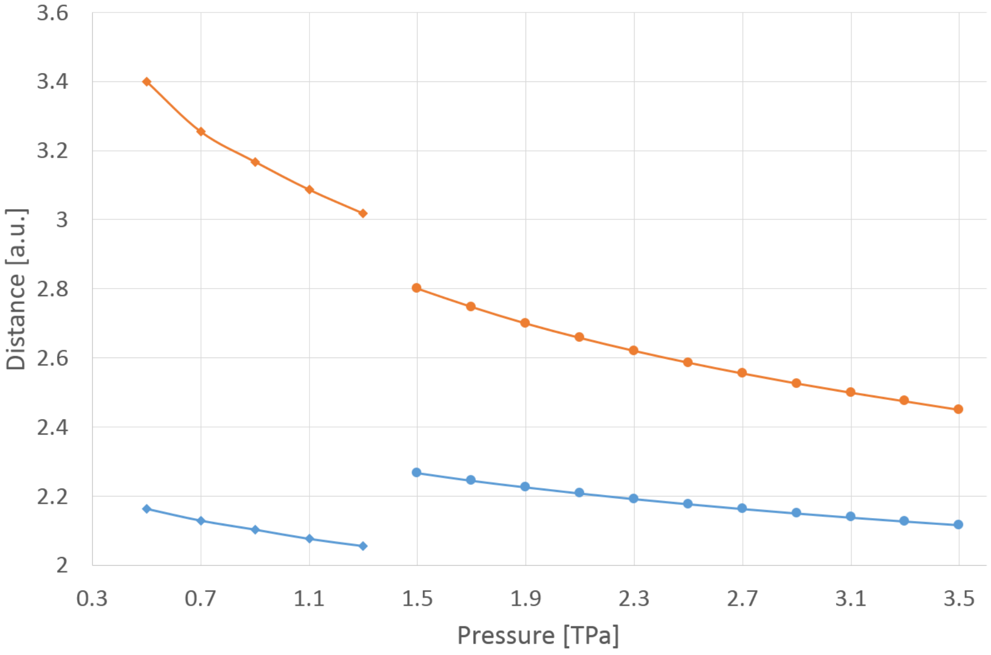

b)

**Figure 2.14.** Evolution of the first (blue), second (orange) and third (green) closest oxygen distances, while pressure increases. a) $O_2$ system structures: P-1 (triangles), C2/m (squares) and Cmcm (circles). b) $O_4$ system structures: Cmma (rhombus) and Cmcm (circles).

## Monoatomic Oxygen (Special Case)

While other diatomic molecules dissociate at pressures below the terapascal regime, we have shown that solid oxygen remains molecular. In fact, a layered monoatomic crystalline phase for oxygen has been predicted to occur only above 9 TPa [28], while other chalcogen elements (elements in group 16 of the periodic table) all take a monoatomic rhombohedral β-Po structure after being compressed: Polonium forms its β structure at zero pressure [50], Tellurium at 11GPa [51], Selenium at 60GPa [52] and Sulfur at 153 GPa [53]. When further compression is applied on Se and Te, a bcc structure is formed after their β-Po-type structure [52] [54] [55]. Given that oxygen exhibits several different structures [28], such as chain-like $I4_1/acd$ at 2 TPa, a Cmcm zigzag structure at 3 TPa, and finally a monoatomic Fmmm structure at 9.3TPa, we intended to complete the picture of oxygen as a chalcogen by making an structural search for monoatomic oxygen up to 8TPa, and then adding a comparison between those structures that we found and the β-Po, bcc and fcc.

For this study we used a slightly different approach in order to make our findings comparable with the results reported in ref. [28]. We used Perdew-Burke-Ernzerhof (PBE) generalized gradient (GGA) exchange-correlation functional, a k-point grid of 20x20x20 due to the very small cells involved and a plane wave kinetic cutoff energy of 60Ry, also, for the most stable structures from the random search, we performed very well converged calculations using hard Norm-Conserving pseudopotentials[3] [56] [57] and nonlinear core corrected PAW, with the same exchange-correlation functional.

The enthalpy values of the monoatomic structures analyzed from 1TPa to 8TPa, are detailed in table 2.6. The enthalpy differences of β-Po, bcc, fcc and the most stable structures from the random search, respect to the Fmmm structure is shown in figure 2.15. We provide some interpretation of these results in the next section.

---

[3] We used the pseudopotentials O.pbe-mt.UPF and O.pbe-hgh.UPF from the Quantum ESPRESSO pseudopotential data base: http://www.quantum-espresso.org/pseudopotential

**Table 2.6.** Enthalpy values for several monoatomic oxygen structures from 1TPa to 8TPa.

| P [TPa] | Random Search Enthalpy [Ry] | BCC Enthalpy [Ry] | FCC Enthalpy [Ry] | β - Po Enthalpy [Ry] | Fmmm Enthalpy [Ry] |
|---|---|---|---|---|---|
| **1** | -39.4635 | -39.4263 | -39.3892 | -39.4193 | -39.4635 |
| **2** | -38.2329 | -38.1736 | -38.1231 | -38.1449 | -38.2329 |
| **3** | -37.2158 | -37.1407 | -37.0745 | -37.0925 | -37.2158 |
| **4** | -36.3216 | -36.2352 | -36.1526 | -36.1710 | -36.3215 |
| **5** | -35.5109 | -35.4176 | -35.3180 | -35.3398 | -35.5122 |
| **6** | -34.7655 | -34.6644 | -34.5477 | -34.5725 | -34.7654 |
| **7** | -34.0669 | -33.9602 | -33.8282 | -33.8550 | -34.0669 |
| **8** | -33.4074 | -33.2954 | -33.1498 | -33.1787 | -33.4072 |

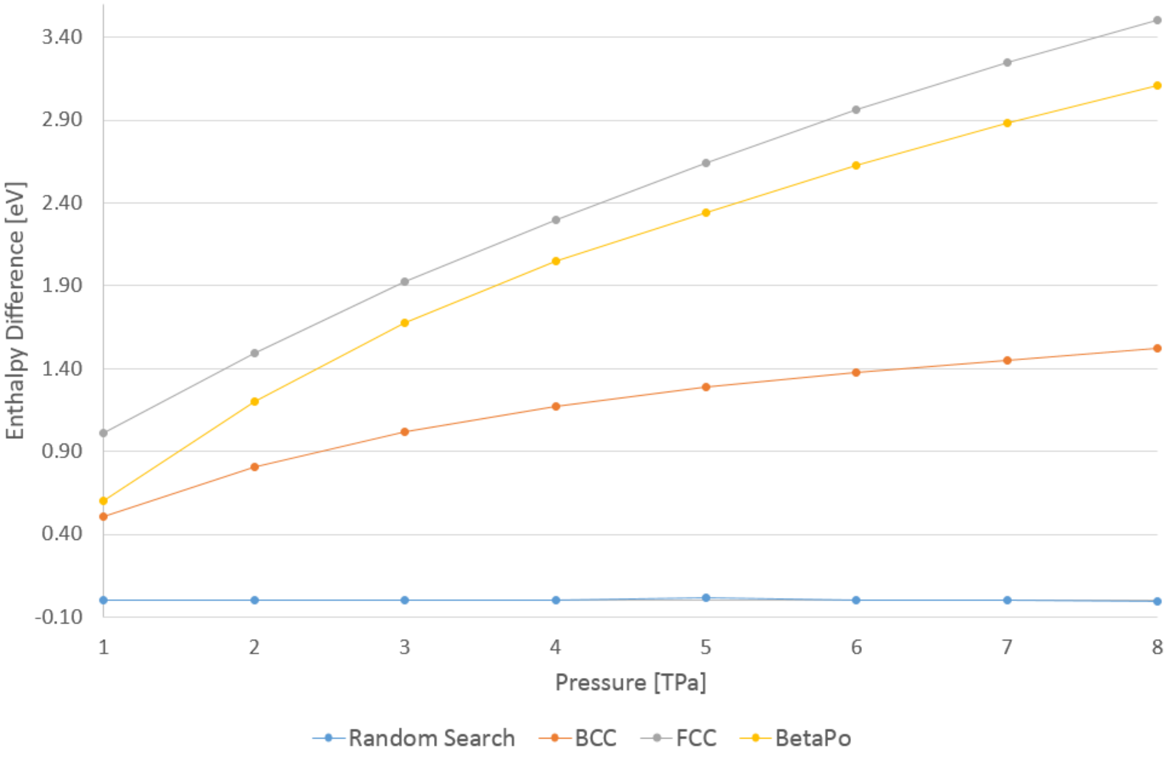

**Figure 2.15.** Enthalpy difference for several monoatomic oxygen structures from 1TPa to 8 TPa. Fmmm structure is the reference.

# DISCUSSION AND CONCLUSIONS

Due to technical limitations, hydrostatic compression experiments can reach pressures up to 300GPa, value that is close to the pressure in the Earth's inner core. At that pressure regime, oxygen would keep its molecular form. Thanks to computational approaches, we can study any chemical systems at pressures that today are impossible to obtain in a laboratory; this limitless scenario was one of the motivations of this work and hence, we were able to probe the solid oxygen system under conditions that are more extreme than those reached so far in the lab.

We were able to establish, with a good level of certainty, the crystal structures that an oxygen system should take for pressures up to 3.50 TPa. From our simulations we found that for pressures above 0.55 TPa for $O_2$ and 1.5 TPa for $O_4$, the most stable structure was the Cmcm which is kept up to 3.50 TPa. This dense Cmcm phase is made up of zigzag chains for both types of unit-cell, as shown in figure 2.16.

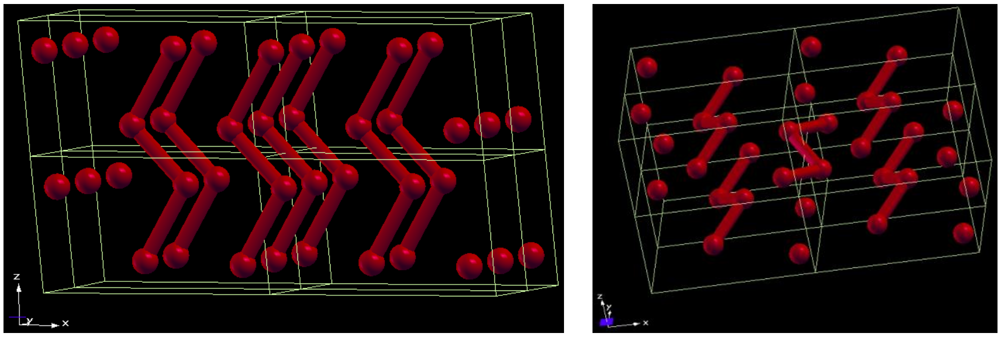

a) b)

**Figure 2.16.** Zigzag chains for a) $O_2$ and b) $O_4$.

The zizgzag formation for the $O_2$ unit-cell was first observed at 0.50 TPa, but at that pressure the bonds are not yet completely symmetric to one another, this behavior is consistent with the first and second nearest neighbors distances found for the $O_2$ system, as shown in figure 2.14.a: at 0.50 TPa the first neighbor increased significantly, while the second decreased. We found that when pressure was increased to 0.55 TPa, the two shortest interatomic distances became symmetrical and the oxygen coordination went from one to two, therefore, the first neighbor and the second neighbor distances (blue and orange lines in Fig. 2.14.a respectively) converge at 0.55 TPa. A similar transition was found at 1.30 TPa for the $O_4$ unit-cell, in both cases much earlier than predicted by other studies [28]. The dramatic changes found for pressures below to 1.50 TPa were also observed by Sun *et al.* [28], therefore more detailed studies around this pressure are necessary for a better understanding of the structural and physical changes that occur under those conditions.

For both unit-cell sizes the stable structure at higher pressures is Cmcm, however for the $O_4$ unit-cell this symmetry group shows up at higher pressures than for the $O_2$ unit-cell. Due to the smaller amount of degrees of freedom available to the $O_2$ system, the only arrangement that it can achieve is the Cmcm at 0.55 TPa. The $O_4$ unit cell instead, having more atoms available to explore possible configurations, remains with the Cmma structure, which seems to be more favorable energetically, until it reaches to 1.50 TPa. By analyzing the enthalpy per atom from 0.35[4] to 1.50 TPa, the enthalpy for the $O_4$ system is lower than for the $O_2$ unit-cell, but from ~1TPa the enthalpy per atom of the $O_2$ is better by a few hundredth electron-volts, as shown in figure 2.17.

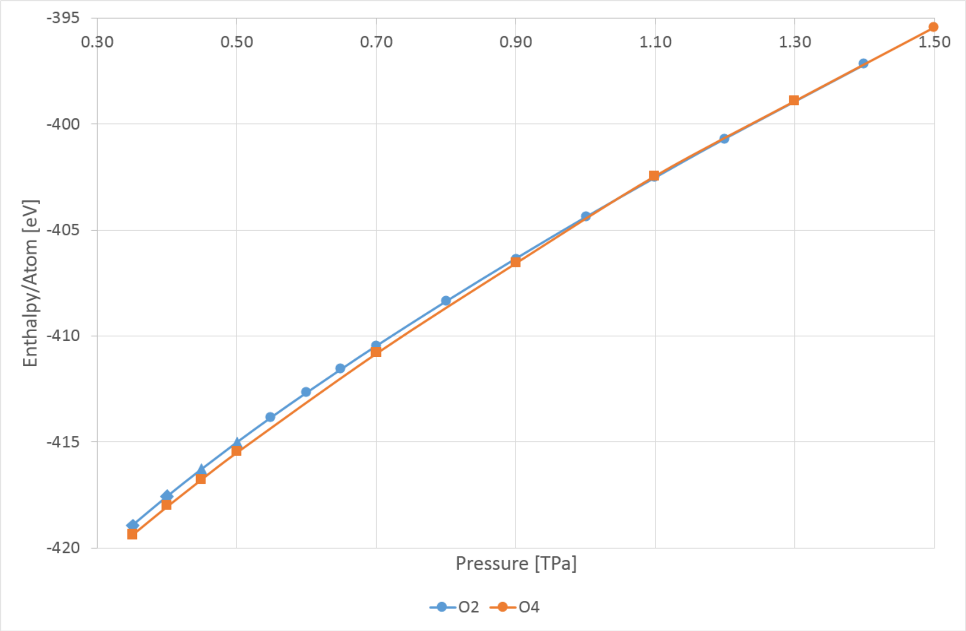

**Figure 2.17.** Enthalpy per atom of the most stables structures of $O_2$ and $O_4$ systems from 0.35 to 1.50 TPa. The symmetry groups are labeled as: Cmma (squares), P-1 (rhombus), C2-m (triangles), and Cmcm (circles).

---

[4] We performed some additional calculations for the $O_4$ unit-cell, in order to establish the enthalpy of the systems for 0.35, 0.40 and 0.45 TPa.

According to the nearest neighbor distances, it is expected that for much higher pressures the coordination number of oxygen will increase, due to the observed fact that the difference in distances between first and second neighbors tend to decrease while pressure increases. Nevertheless, we found a quasi-layered structure for $O_2$ at 1.20 TPa and at 1.50 TPa for $O_4$, we say that it is quasi-layered in the sense that the oxygen atoms are connected with four neighbors forming layers but strictly speaking there are two bonds that are shorter than the other two and given the lack of symmetry for the four bonds the coordination number for oxygen remains as two like in the zig-zag chains. However, we expect that the symmetrization of the four bonds is achieved at pressures above the limit of our studies, i.e. above 3.5 TPa, and the resulting structure perhaps converges to the Fmmm structure reported above 9 TPa by Ref. [28].

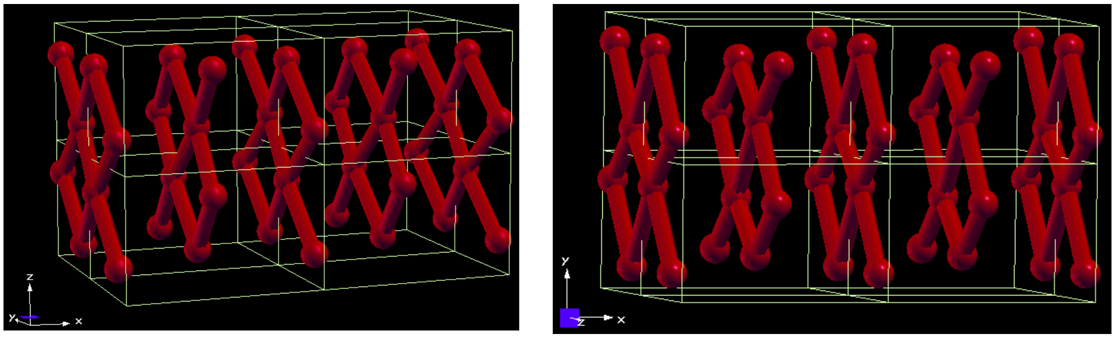

a) b)

**Figure 2.18.** Layered structure for a) $O_2$ and b) $O_4$.

Going forward we think that it is necessary to make more accurate calculations, i.e., with a hard norm-conserving pseudopotential or using PAW, in order to make new studies that can be used to establish similarities and possible differences with previous results in the TPa regime.

We found for monoatomic oxygen that for pressures above 1TPa, the most stable structure is Fmmm. In fact, it is evident that for higher pressures the enthalpy difference increases for all the other structures analyzed. On the other hand, while for Te and Se the bcc structure was observed as a post-$\beta$-Po phase [52] [54] [55], in the case of oxygen the change still occurs for those same two phase although they are metastable, as shown in figure 2.15. We made some additional calculations in order to establish the pressure at which the transition from $\beta$-Po to bcc takes place, and we found that it is slightly above of 0.9 TPa. Even when this pressure is much higher than the ones determined for Te and Se, it is clear that oxygen follows that same trend and therefore at some level it has something in common with other chalcogen elements.

## REFERENCES

[1] Y. A. Freiman and H. J. Jodl, "Solid oxygen," *Physics Reports,* vol. 401, no. 1 - 4, pp. 1 - 288, 2004.

[2] S. Block and G. Piermarini, "The diamond cell stimulates high-pressure research," *Physics Today,* vol. 29, no. 9, p. 44, 1976.

[3] G. Weck, S. Desgreniers, P. Loubeyre and M. Mezouar, "Single-Crystal Structural Characterization of the Metallic Phase of Oxygen," *Physical Review Letters,* vol. 102, no. 25, p. 255503, 2009.

[4] R. A. Alikhanov, "Structure of α Modification of Oxygen," *JETP Letters,* vol. 5, no. 12, p. 349, 1967.

[5] C. S. Barret, L. Meyer and J. Wasserman, "Antiferromagnetic and Crystal Structures of Alpha-Oxygen," *Journal of Chemical Physics,* vol. 47, no. 2, pp. 592 - 597, 1967.

[6] J. E. Cahill and G. E. Leroi, "Raman Studies of Molecular Motion in Condensed Oxygen," *Journal of Chemical Physics,* vol. 51, no. 1, pp. 97 - 104, 1969.

[7] R. J. Meier and R. B. Helmholdt, "Neutron-diffraction study of α- and β-oxygen," *Physical Review B,* vol. 24, no. 3, pp. 1387 - 1393, 1984.

[8] E. M. Hörl, "Structure and structure imperfections of solid β-oxygen," *Acta Crystallographica,* vol. 15, no. 9, pp. 845 - 850, 1962.

[9] D. Schiferl, D. T. Cromer, L. A. Schwalbe and R. L. Mills, "Structure of 'orange' 18O2 at 9.6 GPa and 297 K," *Acta Crystallographica Section B,* vol. 39, no. 2, pp. 153 - 157, 1983.

[10] F. A. Gorelli, M. Santoro, L. Ulivi and M. Hanfland, "Crystal structure of solid oxygen at high pressure and low temperature," *Physical Review B,* vol. 65, no. 17, p. 172106, 2002.

[11] I. N. Goncharenko, O. L. Makarova and L. Ulivi, "Direct Determination of the Magnetic Structure of the Delta Phase of Oxygen," *Physical Review Letters,* vol. 93, no. 5, p. 055502, 2004.

[12] M. Nicol, K. R. Hirsch and W. B. Holzapfel, "Oxygen phase equilibria near 298 K," *Chemical Physics Letters,* vol. 68, no. 1, pp. 49 - 52, 1979.

[13] K. Syassen and M. Nicol, in *Physics of solids under high pressure: proceedings of the International Symposium on the Physics of Solids under High Pressure*, J. S. Schilling and R. N. Shelton, Eds., New York, North-Holland Pub. Co., 1981, p. 419.

[14] M. Nicol and K. Syassen, "High-pressure optical spectra of condensed oxygen," *Physical Review B,* vol. 28, no. 3, pp. 1201 - 1206, 1983.

[15] Y. Akahama, H. Kawamura, D. Häusermann, M. Hanfland and O. Shimomura, "New High-Pressure Structural Transition of Oxygen at 96 GPa Associated with Metallization in a Molecular Solid," *Pysical Review Letters,* vol. 74, no. 23, pp. 4690 - 4693, 1995.

[16] S. Desgreniers and K. Brister, in *High Pressure Science and Technology - World Scientific*, W. A. Treciakowski, Ed., Singapore, 1996.

[17] G. Weck, P. Loubeyre and R. LeToullec, "Observation of Structural Transformations in Metal Oxygen," *Physical Review Letters,* vol. 88, no. 3, p. 035504, 2002.

[18] S. W. Johnson, M. Nicol and D. Schiferl, "Algorithm for sorting diffraction data from a sample consisting of several crystals enclosed in a sample environment apparatus," *Journal of Applied Crystallography,* vol. 26, no. 3, pp. 320 - 326, 1993.

[19] F. A. Gorelli, L. Ulivi, M. Santoro and R. Bini, "The ε Phase of Solid Oxygen: Evidence of an O4 Molecule Lattice," *Physical Review Letters,* vol. 83, no. 20, pp. 4093 - 4096, 1999.

[20] L. F. Lundegaard, G. Weck, M. McMahon, S. Desgreniers and P. Loubeyre, "Observation of an O8 molecular lattice in the ε phase of solid oxygen," *Nature,* vol. 443, no. 7108, pp. 201 - 204, 2006.

[21] H. Fujihisa, Y. Akahama, H. Kawamura, Y. Ohishi, O. Shimomura, H. Yamawaki, M. Sakashita, Y. Gotoh, S. Takeya and K. Honda, "Cluster Structure of the Epsilon Phase of Solid Oxygen," *Physical Review Letters,* vol. 97, no. 8, p. 085503, 2006.

[22] M. Bartolomei, J. Pérez-Rios, E. Carmona-Novillo, M. I. Hernández, J. Campos-Martínez and R. Hernández-Lamoneda, "Can density functional theory methods be used to simulate the ∊ phase of solid oxygen?," *Chemical Physics Letters,* vol. 592, pp. 170 - 174, 2014.

[23] F. Gorelli, L. Ulivi, M. Santoro and R. Bini, "Spectroscopic study of the ε phase of solid oxygen," *Physical Review B,* vol. 63, no. 10, p. 104110, 2001.

[24] M. Santoro, F. A. Gorelli, L. Ulivi, R. Bini and H. J. Jodl, "Antiferromagnetism in the high-pressure phases of solid oxygen: Low-energy electronic transitions," *Physical Review B,* vol. 64, no. 6, p. 064428, 2001.

[25] J. B. Neaton and N. W. Ashcroft, "Low-Energy Linear Structures in Dense Oxygen: Implications for the ε Phase," *Physical Review Letters,* vol. 88, no. 20, p. 205503, 2002.

[26] Y. Crespo, M. Fabrizio, S. Scandolo and E. Tosatti, "Collective spin 1 singlet phase in high-pressure oxygen," *Proceedings of the National Academy of Sciences,* vol. 111, no. 29, pp. 10427 - 10432, 2014.

[27] Y. Ma, A. R. Oganov and C. W. Glass, "Structure of the metallic ζ-phase of oxygen and isosymmetric nature of the ε-ζ phase transition: Ab initio simulations," *Physical Review B,* vol. 76, no. 6, p. 064101, 2007.

[28] J. Sun, M. Martínez-Canales, D. D. Klug, C. J. Pickard and R. J. Needs, "Persistence and Eventual Demise of Oxygen Molecules at Terapascal Pressures," *Physical Review Letters,* vol. 108, no. 4, p. 045503, 2012.

[29] C. J. Pickard and R. J. Needs, "Structure of phase III of solid hydrogen," *Nature Physics,* vol. 3, no. 7, pp. 473 - 476, 2007.

[30] Y. Fujii, K. Hase, Y. Ohishi, H. Fujihisa, N. Hamaya, K. Takemura, O. Shimomura, T. Kikegawa, Y. Amemiya and T. Matsushita, "Evidence for molecular dissociation in bromine near 80 GPa," *Physical Review Letters,* vol. 63, no. 5, pp. 536 - 539, 1989.

[31] K. Takemura, S. Minomura, O. Shimomura and Y. Fujii, "Observation of Molecular Dissociation of Iodine at High Pressure by X-Ray Diffraction," *Physical Review Letters,* vol. 45, no. 23, pp. 1881 - 1884, 1980.

[32] M. I. Eremets, R. J. Hemley, H.-k. Mao and E. Gregoryanz, "Semiconducting non-molecular nitrogen up to 240 GPa and its low-pressure stability," *Nature,* vol. 411, no. 6834, pp. 170 - 174, 2001.

[33] Y. Ma, A. R. Oganov, Z. Li, Y. Xie and J. Kotakoski, "Novel High Pressure Structures of Polymeric Nitrogen," *Physical Review Letters,* vol. 102, no. 6, p. 065501, 2009.

[34] S. Serra, G. Chiarotti, S. Scandolo and E. Tosatti, "Pressure-Induced Magnetic Collapse and Metallization of Molecular Oxygen: The ζ- O2 Phase," *Physical Review Letters,* vol. 80, no. 23, pp. 5160 - 5163, 1998.

[35] L. Zhu, Z. Wang, Wang Yanchao, G. Zou, H.-k. Mao and Y. Ma, "Spiral chain O4 form of dense oxygen," *Proceedings of the National Academy of Sciences,* vol. 109, no. 3, pp. 751 - 753, 2012.

[36] T. Ishikawa, K. Mukai and K. Shimizu, "First-principles study on superconductivity of solid oxygen," *High Pressure Research: An International Journal,* vol. 32, no. 4, pp. 457 - 463, 2012.

[37] F. Datchi and G. Weck, "X-ray crystallography of simple molecular solids up to megabar pressures: application to solid oxygen and carbon dioxide," *Zeitschrift für Kristallographie – Crystalline Materials,* vol. 229, no. 2, pp. 68 - 168, 2014.

[38] C. J. Pickard and R. J. Needs, "Ab initio Random Structure Searching," *Journal of Physics: Condensed Matter,* vol. 23, no. 5, p. 053201, 2011.

[39] C. J. Pickard and R. J. Needs, "High-Pressure Phases of Silane," *Physical Review Letters,* vol. 97, no. 4, p. 045504, 2006.

[40] C. J. Pickard and R. J. Needs, "When is H2O not water?," *Journal of Chemical Physics,* vol. 127, no. 24, 2007.

[41] C. J. Pickard and R. J. Needs, "Metallization of aluminum hydride at high pressures: A first-principles study," *Physical Review B,* vol. 76, no. 14, p. 144114, 2007.

[42] C. J. Pickard and R. J. Needs, "Stable phases of iron at terapascal pressures," *Journal of Physics: Condensed Matter,* vol. 21, no. 45, p. 452205, 2009.

[43] C. J. Pickard and R. J. Needs, "High-Pressure Phases of Nitrogen," *Physical Review Letters,* vol. 102, no. 12, p. 125702, 2009.

[44] C. J. Pickard and R. J. Needs, "Dense Low-Coordination Phases of Lithium," *Physical Review Letters,* vol. 102, no. 14, p. 146401, 2009.

[45] A. J. Morris, C. J. Pickard and R. J. Needs, "Hydrogen/silicon complexes in silicon from computational searches," *Physical Review B,* vol. 78, no. 18, p. 184102, 2008.

[46] P. Giannozzi, S. Baroni, N. Bonini, M. Calandra, R. Car, C. Cavazzoni, D. Ceresoli, G. L. Chiarotti, M. Cococcioni, I. Dabo, A. Dal Corso, S. de Gironcoli, S. Fabris, G. Fratesi, R. Gebauer, U. Gerstmann, C. Gougoussis, A. Kokalj, M. Lazzeri, L. Martin-Samos, C. Sbraccia, S. Scandolo, G. Sclauzero, A. P. Seitsonen, A. Smogunov, P. Umari and R. M. Wentzcovitch, "QUANTUM ESPRESSO: a modular and open-source software project for quantum simulations of materials," *Journal of Physics: Condensed Matter,* vol. 21, no. 39, p. 395502,

2009.

[47] J. P. Perdew, K. Burke and M. Ernzerhof, "Generalized Gradient Approximation Made Simple," *Physical Review Letters,* vol. 77, no. 18, pp. 3865 - 3868, 1996.

[48] H. J. Monkhorst and J. D. Pack, "Special points for Brillouin-zone integrations," *Physical Review B,* vol. 13, no. 12, pp. 5188 - 5192, 1976.

[49] H. T. Stokes and D. M. Hatch, "FINDSYM: program for identifying the space-group symmetry of a crystal," *Journal of Applied Crystallography,* vol. 38, no. 1, pp. 237 - 238, 2005.

[50] R. J. DeSando and R. C. Lange, "The structures of polonium and its compounds—I α and β polonium metal," *Journal of Inorganic and Nuclear Chemistry,* vol. 28, no. 9, pp. 1837 - 1846, 1966.

[51] J. C. Jamieson and D. B. McWhan, "Crystal structure of tellurium at high pressures," *The Journal of Chemical Physics,* vol. 43, no. 4, pp. 1149 - 1152, 1968.

[52] Y. Akahama, M. Kobayashi and H. Kawamura, "Structural studies of pressure-induced phase transitions in selenium up to 150 GPa," *Physical Reiew B,* vol. 47, no. 1, pp. 20 - 26, 1993.

[53] O. Degtyareva, E. Gregoryanz, H. K. Mao and R. J. Hemley, "Crystal structure of sulfur and selenium at pressures up to 160 GPa," *High Pressure Research,* vol. 25, no. 1, pp. 17 - 33, 2005.

[54] F. El Haj Hassan, A. Hijazi, M. Zoater and F. Bahsoun, "Structural and electronic properties of BCC tellurium under high pressure," *Physica B,* vol. 363, no. 1 - 4, pp. 82 - 87, 2005.

[55] M. Otani and N. Suzuki, "Structural and superconducting transition in selenium at high pressure," *Physical Review B,* vol. 63, no. 10, p. 104516, 2001.

[56] S. Goedecker, M. Teter and J. Hutter, "Separable dual-space Gaussian pseudopotentials," *Physical Review B,* vol. 54, no. 3, pp. 1703 - 1710, 1996.

[57] C. Hartwigsen, S. Goedecker and J. Hutter, "Relativistic separable dual-space Gaussian pseudopotentials from H to Rn," *Physical Review B,* vol. 58, no. 7, pp. 3641 - 3662, 1998.

# Chapter 3

## STUDY CASE: COPPER CLUSTERS IN VACUUM

### OVERVIEW ON CLUSTERS

After atoms, clusters represent the most elemental building blocks in nature. Generally, clusters are aggregates of atoms and molecules which display intermediate properties between isolated atoms or molecules, and the bulk matter. They are characterized by their size and they can be classified in small, medium, and large clusters, as shown in table 3.1.

**Table 3.1** Classification of clusters according to size. *N* is the number of atoms, *D* is the diameter (for a cluster of sodium atoms) and *$F_S$* is the fraction of surface atoms. Taken from [1].

| | **Small** | **Medium** | **Large** |
|---|---|---|---|
| **N** | $\leq 10^2$ | $10^2 - 10^4$ | $>10^4$ |
| **D/nm** | $\leq 1.9$ | $1.9 - 8.6$ | $>8.6$ |
| **$F_S$** | $\geq 0.86$ | $0.86 - 0.19$ | $\leq 0.19$ |

The quantity of atoms on the surface of a cluster is highly related to its properties; therefore, the surface chemistry is extremely important in a cluster. As the cluster's size gets smaller, both the valence and the conduction bands change from a continuous density of states into a discretized set of energy levels. As a consequence, the properties of the cluster vary dramatically when its shape and size are modified.

Due to their own intrinsic characteristics, clusters have become an interesting topic of research, not only for the wide range of particle sizes (from molecular to microcrystalline), but also for the evolution of the geometric and electronic structures and how the physical and chemical properties are related to them. Of course, how large should a cluster be before its properties resemble those of the bulk element will depend on the property of interest being studied and the nature of the component atoms. Now, clusters can be made of identical particles, leading to homo-atomic or homo-molecular clusters, $A_a$, or be composed by two or more different species, obtaining hetero-atomic or hetero-molecular clusters, $A_aB_b$. The atomic species that can form clusters are most of the elements of the periodic table, and they can be subdivided as metal clusters, semiconductor clusters, ionic clusters, rare gas clusters, molecular clusters and cluster molecules [1]. Since we are dealing with copper clusters, we are going to focus in metallic clusters.

## TRANSITION METAL CLUSTERS

### Shell effects and magic numbers

Copper is a transition metal with electronic configuration $[Ar]3d^{10}s^1$. Given that the *d* shell is filled with 10 electrons and the valence shell contains a single *s* electron, is normal to expect some similarities between copper clusters (or noble metal clusters, $Cu_n$, $Ag_n$ and $Au_n$, in general) and alkali metal clusters. For instance, Knight *et al.* [2] reported that for sodium clusters $Na_n$ ($n = 4 - 100$), they found a spectra that shows well defined peaks at $n = 8, 20, 34, 40, 58$ and $92$. On the other hand, Katakuse *et al.* [3] found the same behavior for positive copper clusters at $n = 3, 9, 19, 21, 35, 41, 59, 92$ and $139$, and for negative copper clusters: $n = 7, 17, 19, 33, 39, 57, 91$ and $137$. Then, the shell-closing numbers ($n_s$) for positive clusters ($n_p = ns + 1$) were $n_s = 2, 8, 18, 20, 34, 40, 58, 91$ and $138$, and for negative ($n_n = n_s - 1$) clusters were: $n_s = 8, 18, 20, 34, 40, 58, 92$ and $138$. Going beyond the similarity between the transition and alkali metals, those numbers mean that clusters with these amounts of atoms are relatively more stable than the others, and they are known as ***magic numbers***. In one of those special cases, one could reason that according to the Jellium model [1] eight free electrons completely fill the 1s and 1p energy states, thus forming a complete valence shell, therefore making $Cu_8$ cluster very stable.

## Clusters Band-Gap

A consequence of still being in the quantum-size region is that metal clusters stay in a mesoscopic state between the atomic (non-metallic) and bulk (metallic) regimes. Also, metal clusters display a sizable HOMO[1]-LUMO[2] band gap that is similar to that for semiconductors. This behavior is very significant for possible applications, i.e. doping semiconductors, as shown in figure 3.1.

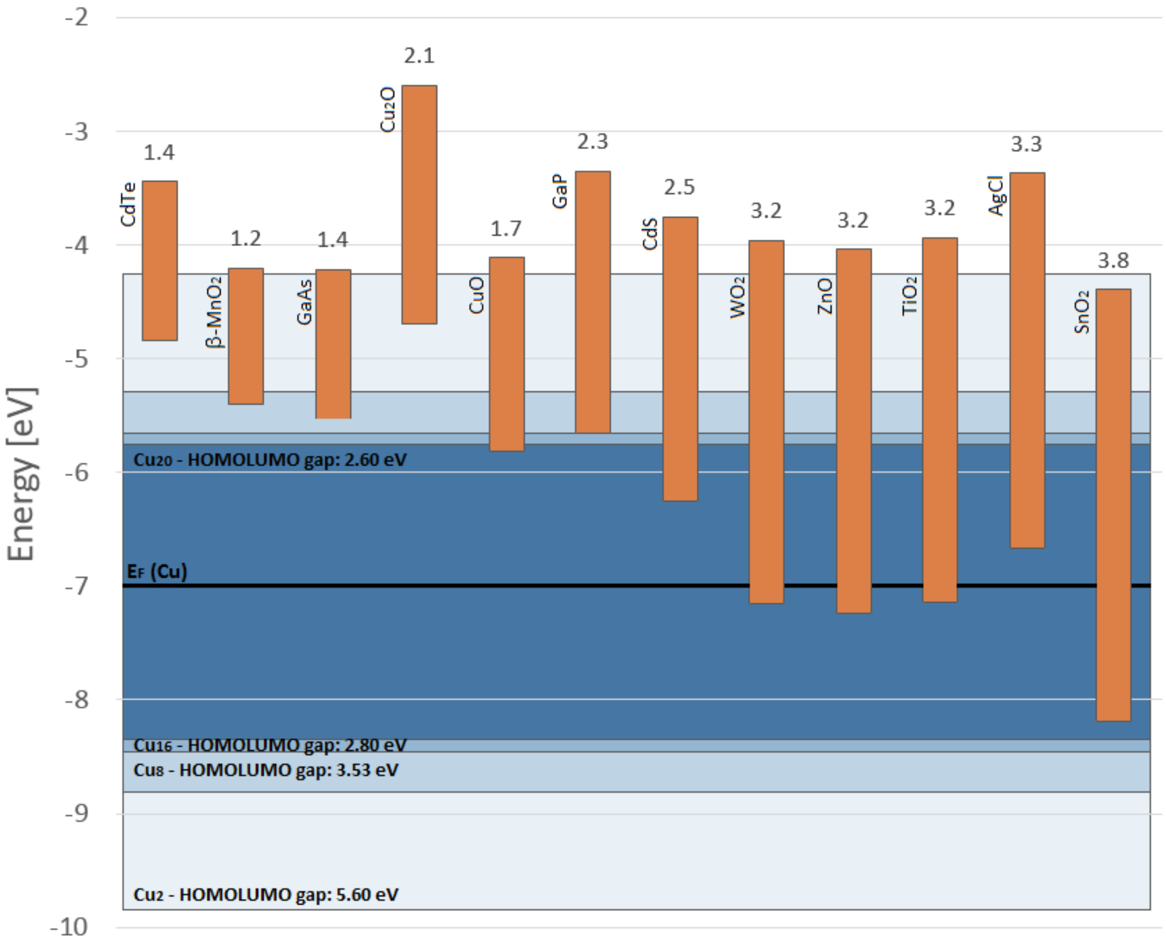

**Figure 3.1.** Schematic comparison between band gaps of different sizes of copper clusters (blue tones) and several semiconductors (orange bars). [4]

---

[1] Highest occupied molecular orbital

[2] Lowest unoccupied molecular orbital

In figure 3.1, for copper the Fermi level was calculated as $\varepsilon_F = \frac{-50.1eV}{(r_s/a_0)^2}$ [5], with $r_s$ = 1.41Å and $a_0$ = 52.9Å, leading to $\varepsilon_F$=-7.0519 eV. The band gap was calculated using the spherical Jellium model: $E_G = \varepsilon_F/N^{1/3}$ [1]. According to this expression, the HOMO-LUMO gap is proportional to $N^{-1/3}$, so the gap gets smaller while the cluster size increases and eventually this separation will transform into the gap between the valence (called before HOMO) and the conduction (called before LUMO) bands. However, this trend is not monotonous due to electronic shell effects, for instance the gap difference between n=2 and n=8 is 2.07eV, while for n=8 and n=16 (with a size twice larger) is only 0.73eV.

Since we are dealing with clusters of size n≤20, the calculations made with a simple Jellium model have a good agreement with DFT, thus there is no need to use a correction due to anharmonicities observed in larger clusters [4].

## STATE OF THE ART

Metallic clusters, especially clusters of coinage metals Cu, Ag and Au, play a central role in nanotechnology [6] [7] [8] and catalysis [9] [10] [11] [12], where catalyst must be very selective for certain chemical reactions. Noble metal clusters have shown this high selectivity, therefore, in order to improve the known catalysts and design new ones, it is important to know and understand their structural and electronic properties, which have been studied widely.

As already mentioned, noble metal clusters are expected to exhibit certain similarities with alkali metal clusters, due to their closed *d* shell and the single *s* valence electron:

- Cu: [Ar] $3d^{10}$ $4s^1$
- Ag: [Kr] $4d^{10}$ $5s^1$
- Au: [Xe] $5d^{10}$ $6s^1$

However, experimental studies [13] [14] [15] [16] have shown that the localized *d* electrons of the noble metals have also a major role in their geometrical and electronic structures.

Copper clusters are quite different from the others coinage metal clusters, because Cu's Fermi level is very different from silver and gold, and can be expected that its catalytic behavior will be also different [17]. Neutral, anionic and cationic copper clusters, have been studied experimentally using several techniques such as Electron Spin Resonance [18], Photoelectron Spectra [19] [20] and Collision-Induced Dissociation [21] [22]. Theoretically, several studies have reported possible structures for copper clusters using a wide range of techniques, for instance Massobrio *et al.* [23] used the Car Parinello method within the Local Density Approximation of Density Functional Theory for $Cu_n$ (n = 2, 3, 4, 6, 8, 10). Kabir *et al.* studied small clusters for $n \leq 9$ using Full-Potential Muffin-Tin Orbitals [24] and Tight-Binding Molecular Dynamics [25]. Configuration Interaction was used by Akeby *et al.* [26] for Cu clusters anions of up to 10 atoms. Li *et al.* [27] examined neutral and anion clusters of copper, $Cu_n$ (n = 3 – 11), using Real Space Pseudopotentials constructed within the Local Density Approximation. Finally, Böyükata and Belchior [28] performed Molecular Dynamics simulations via an empirical potential, to investigate geometries, growing patterns, structural stabilities, energetics and magic sizes of copper clusters, $Cu_n$ (n = 2 – 45).

## Isomers

Given the difference between clusters and bulk material, it is necessary to emphasize one last scenario. Let's take a molecule and compare it with a cluster: a molecule has a definite composition and structure, while a cluster differ in both, due to this they can be composed of any number of atoms (or molecules). As a consequence, the most stable geometrical structure will depend on the number of atoms into it. Nevertheless, it is possible that for a given cluster, several stable local structures appear with a different spatial arrangement of atoms and bonding, that not necessarily share similar properties among them [29]. These structures are called *isomers*, and the number of them tends to increase with the cluster size. Therefore, properties beyond structure like: binding energy, relative stability, or bonding, also depend strongly on the number of atoms (or molecules) that constitute the cluster.

For the amount of atoms that we studied in this work, the isomers and their characteristics are gathered in the following tables.

**Table 3.2.** Symmetry group of $Cu_n$ clusters (n = 3 – 7)

| Cun | Ref. [23] | Ref. [25] | Ref. [27] | Ref. [28] |
|---|---|---|---|---|
| **n = 3** | $C_{2v}$ | 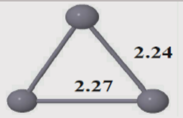 <br>$C_{2v}$<br>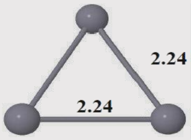 <br>$D_{3h}$<br>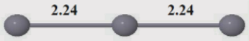 <br>$D_{\infty h}$ | 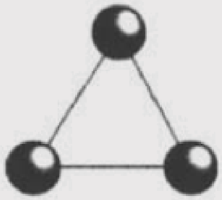 | 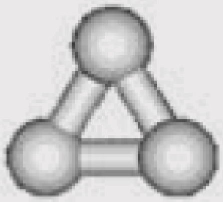 |
| **n = 4** | $D_{2h}$ | 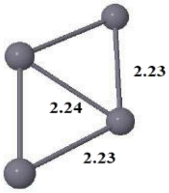 <br>$D_{2h}$<br>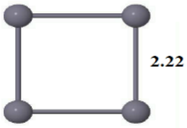 <br>$D_{4h}$<br>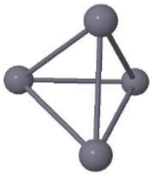<br>$T_d$ | 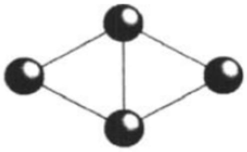 | 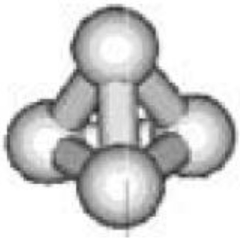 |
| **n = 5** | Not reported | 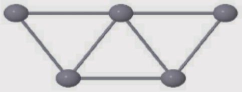<br>$C_{2v}$<br>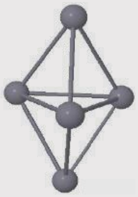<br>$D_{3h}$ | 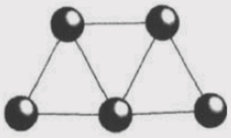 | 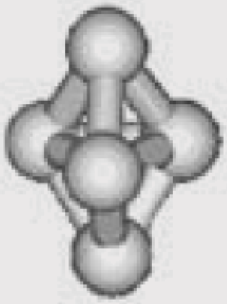 |

**Table 3.2.** Symmetry group of $Cu_n$ clusters (n = 3 – 7). (Cont.)

| $Cu_n$ | Ref. [23] | Ref. [25] | Ref. [27] | Ref. [28] |
|---|---|---|---|---|
| **n = 6** | 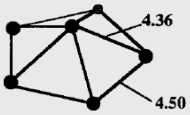 $C_{5v}$<br>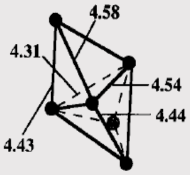  4.58<br>4.31<br>4.54<br>4.44<br>4.43 $C_{2v}$<br>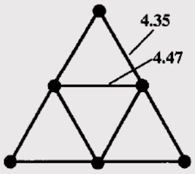 $D_{3h}$ | 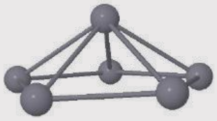 $C_{5v}$<br>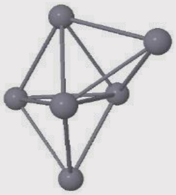 $C_{2v}$<br>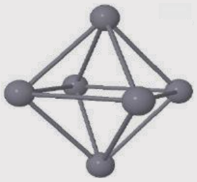 $O_h$ | 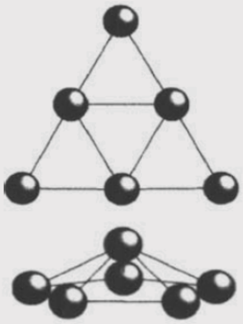 | 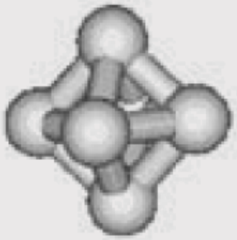 |
| **n = 7** | Not reported | 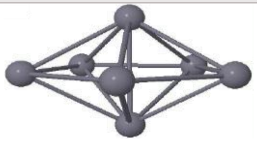 $D_{5h}$<br>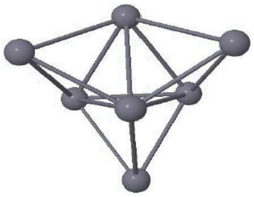 $C_{3v}$(I)<br>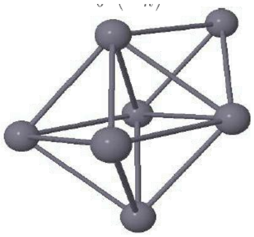 $C_{3v}$(II) | 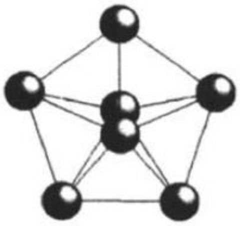 | 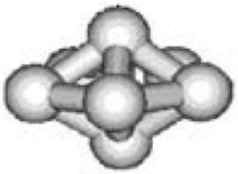 |

**Table 3.3.** Binding energy in [eV/atom] of $Cu_n$ clusters ($n = 3 - 7$).

| $Cu_n$ | Ref. [23] | | | Ref. [25] | | | Ref. [27] | Ref. [28] | Ref. [21] | Ref. [22] |
|---|---|---|---|---|---|---|---|---|---|---|
| **n = 3** | 1.63<br>$C_{2v}$ | | | 1.43<br>$C_{2v}$ | 1.32<br>$D_{3h}$ | 1.13<br>$D_{\infty h}$ | 1.40 | 0.58 | 0.86 | 1.07 |
| **n = 4** | 2.09<br>$D_{2h}$ | | | 2.00<br>$D_{2h}$ | 1.73<br>$D_{4h}$ | 1.46<br>$T_d$ | 1.81 | 0.87 | 0.99 | 1.48 |
| **n = 5** | Not reported | | | 2.24<br>$C_{2v}$ | 2.03<br>$D_{3h}$ | | 1.96 | 1.06 | 1.11 | 1.56 |
| **n = 6** | 2.49<br>$C_{5v}$ | 2.49<br>$C_{2v}$ | 2.49<br>$D_{3h}$ | 2.54<br>$C_{5v}$ | 2.40<br>$C_{2v}$ | 1.98<br>$O_h$ | 2.17 | 1.26 | 1.23 | 1.73 |
| **n = 7** | Not reported | | | 2.63<br>$D_{5h}$ | 2.50<br>$C_{3v}$(I) | 2.30<br>$C_{3v}$(II) | 2.35 | 1.38 | 1.20 | 1.86 |

## METHODOLOGY

To generate a cluster we first estimate the volume of a cubic box to enclose the cluster and then we insert copper atoms at positions generated randomly, fixing one atom at the center of the box and the rest around it. Then, that cubic box is placed inside a much larger unit-cell where periodic boundary conditions are imposed. This unit-cell must be large enough to consider the cluster as isolated, even when the software enforces periodic boundary conditions and replicates the unit-cell in all directions as a solid.

We generated a thousand samples for each number of atoms N that composed the cluster and each sample started with a different configuration; atomic positions were later relaxed until the arrangement reached a local energy minima inside the free-energy landscape. We used the pw.x code from the Quantum ESPRESSO package [30] to perform density functional electronic structure calculations and ionic relaxations for each cluster generated randomly. The atomic positions were then displaced in the direction of the forces that acted on the system, until the structure was in equilibrium, which means that the forces were reduced to a value very close to zero.

Lastly, we looked for the structure with the lowest energy among all in order to determine the most stable arrangement for each cluster. Nevertheless, given the possibility of finding several isomers of the same cluster, we compared all the structures in order to find abrupt energy changes that might indicate the presence of a new isomer.

## TECHNICAL DETAILS

For the calculations we used the Perdew-Burke-Ernzerhof (PBE) generalized gradient (GGA) exchange-correlation functional [31], with ultra-soft pseudo-potentials[3] and the Brillouin-Zone integrations were approximated using the method of Monkhorst and Pack [32]. Given that we performed the calculation assuming the system as isolated, since we were dealing with clusters, we used the Makov-Payne correction to the total energy [33].

For this study case, at the beginning we performed three energy convergence tests in order to determine the following parameters:

- K-point grid
- Plane wave kinetic cutoff
- Volume of the unit cell

We used a three-atom cluster to make those calculations, because the volume occupied by it would be the smallest in the real space and therefore, in the reciprocal space it becomes the largest. It must be well sampled in order to obtain accurate data so that we can extend these parameters to the larger systems. The results of the three tests are plotted in figure 3.2.

---

[3] We used the pseudopotentials Cu.pbe-n-van_ak.UPF from the Quantum ESPRESSO pseudopotential data base: http://www.quantum-espresso.org/pseudopotentials

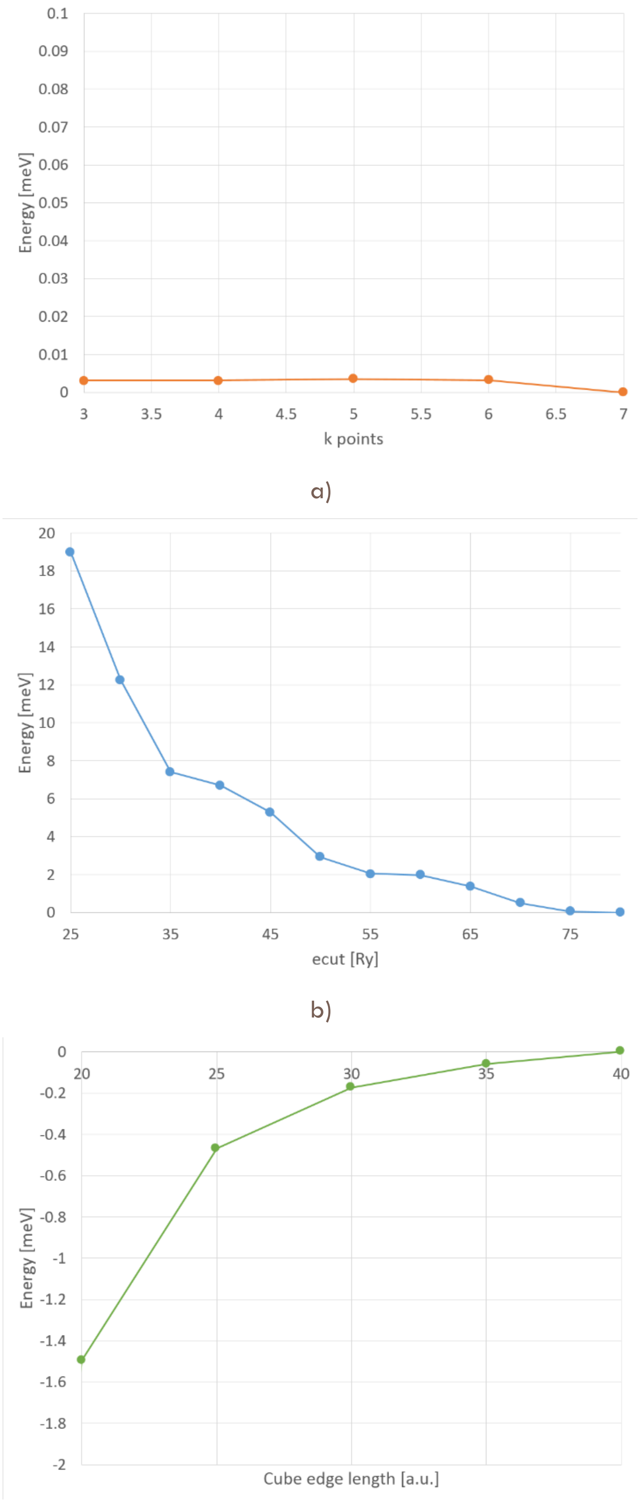

a)

b)

c)

**Figure 3.2.** Total energy convergence for a $Cu_3$ cluster. Varying a) isotropic k-points grid, b) plane wave kinetic cutoff and c) cubic unit-cell edge length.

We are interested in finding isomers for different cluster configurations, so, we performed two calculations: the first one relaxes the starting random arrangement just enough to get close to the final atomic arrangement, and with this result we ran a second relaxation calculation which is more accurate. Therefore, guided by the results obtained with the convergence tests, we used a final calculation k-point grid of 4x4x4, a plane wave kinetic cutoff of 60Ry, and a cubic unit-cell of edge 30 a.u. The main parameters used for both calculations are detailed in table 3.4.

**Table 3.4.** Input parameters used in Quantum ESPRESSO for the copper clusters' structural search.

| Parameter | First calculation | Second calculation |
|---|---|---|
| **ecutwfc** | 25 | 60 |
| **ecutrho** | 200 | 240 |
| **conv_thr** | 5D-7 | 1D-10 |
| **mixing_beta** | 0.48D0 | 0.55D0 |
| **diago_david_ndim** | 8 | 16 |
| **trust_radius_ini** | 2D-1 | 2D-2 |
| **trust_radius_max** | 6D-1 | 2D-1 |
| **trust_radius_min** | 1D-8 | 1D-10 |
| **k_points** | 2 2 2 | 4 4 4 |

## RESULTS

Each group of thousand samples converged into a few local energy minima, which correspond to isomers of the cluster. The total energy varies dramatically when an isomer is found, as shown in figure 3.3.

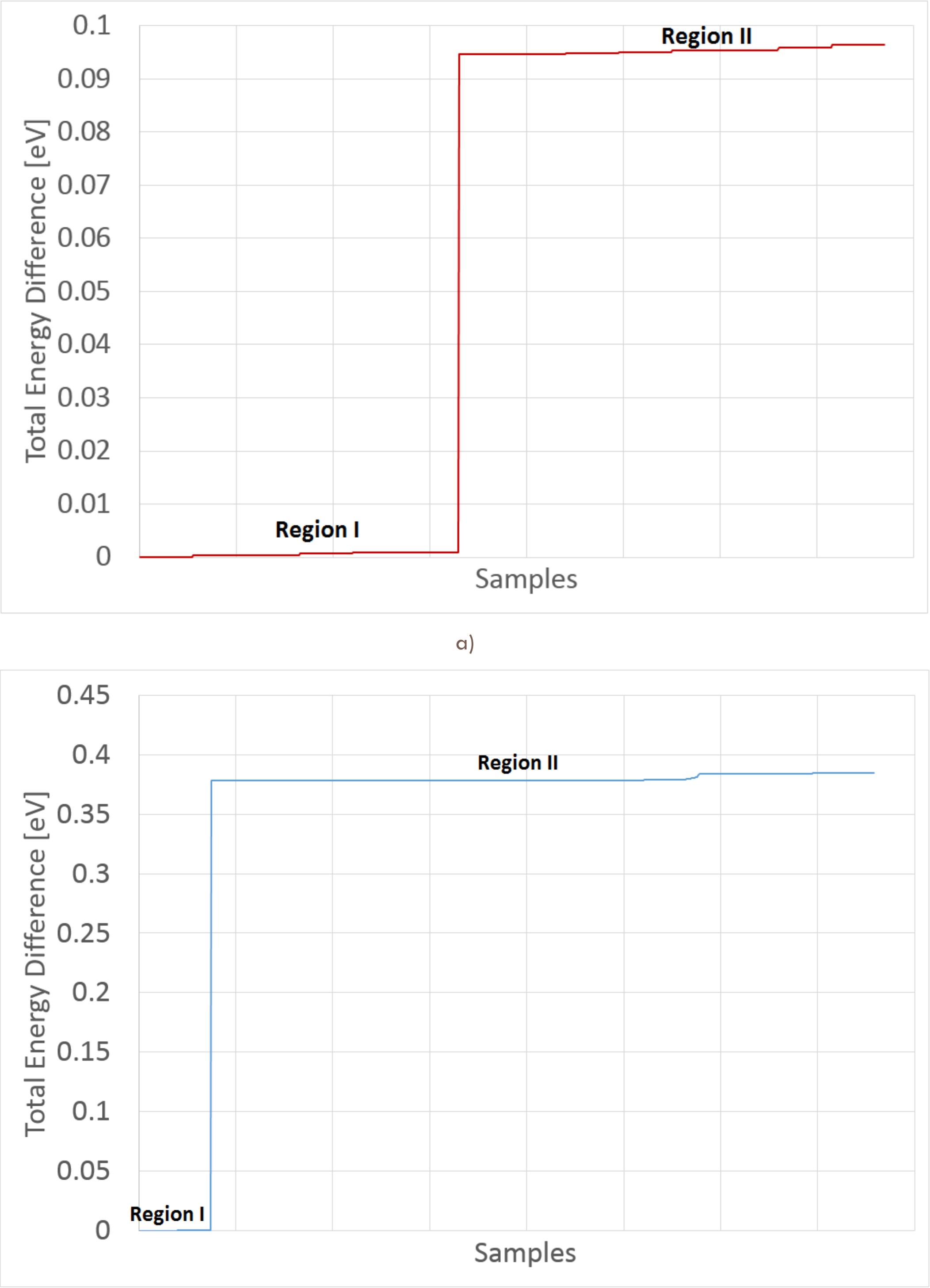

a)

b)

**Figure 3.3.** Energy evolution of: a) $Cu_3$ (red line), b) $Cu_4$ (blue line). For each size, the first region is the ground state structure and energies from region II onwards are associated to new isomers.

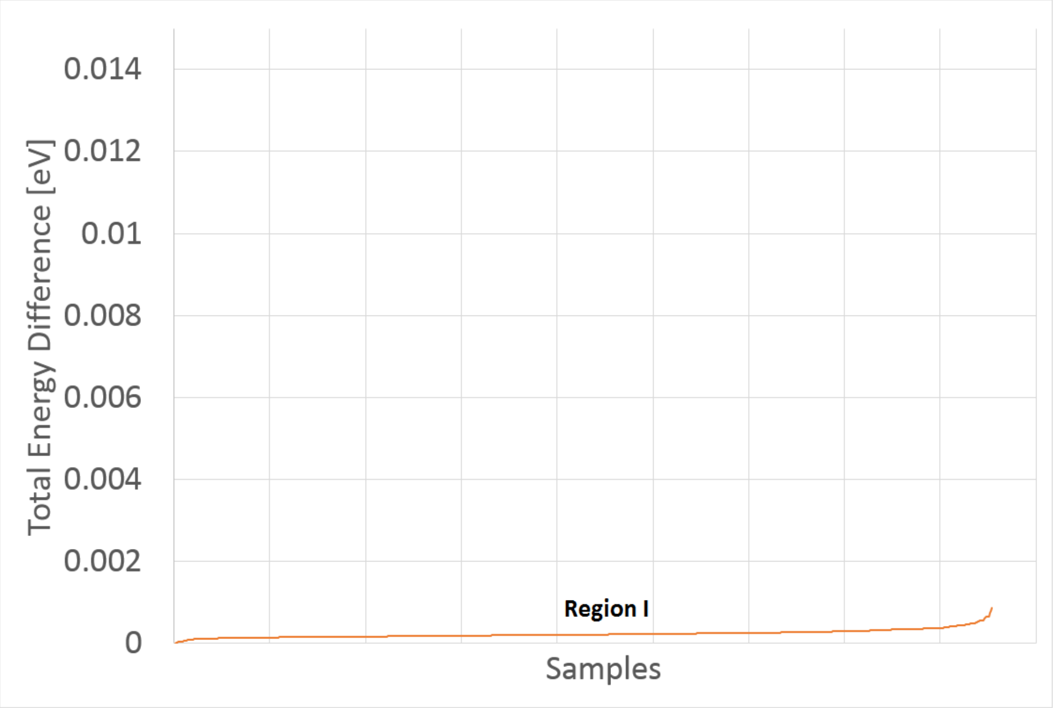

c)

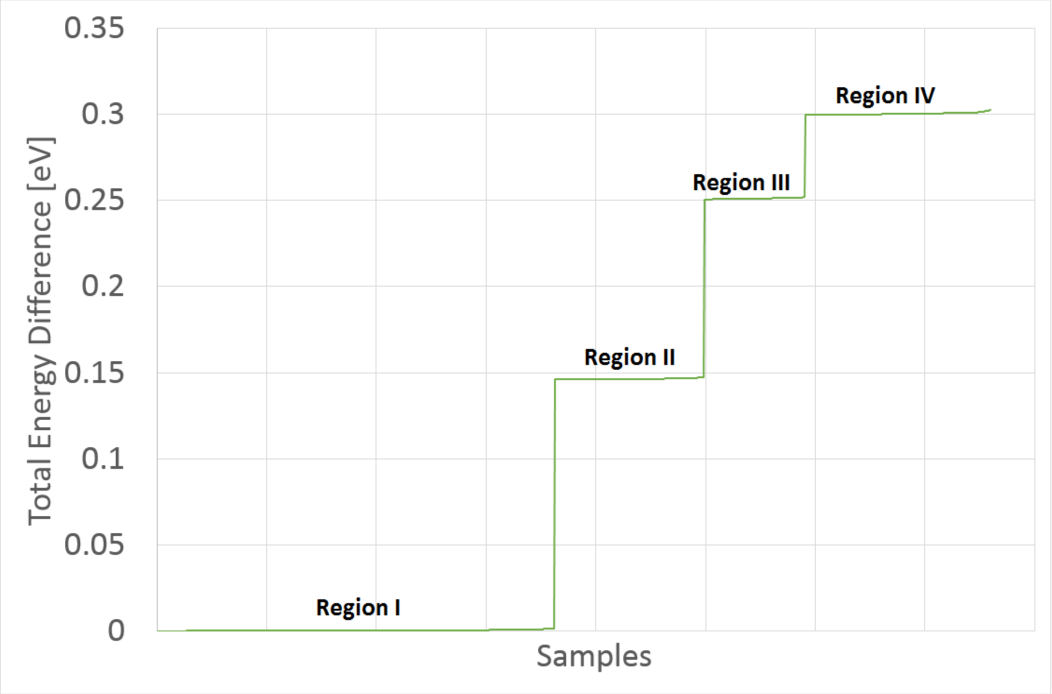

d)

**Figure 3.3.** Energy evolution of: c) $Cu_5$ (orange line), d) $Cu_6$ (green line) and e) $Cu_7$ (yellow line). For each size, the first region is the ground state structure and energies from region II onwards are associated to new isomers. (Cont.)

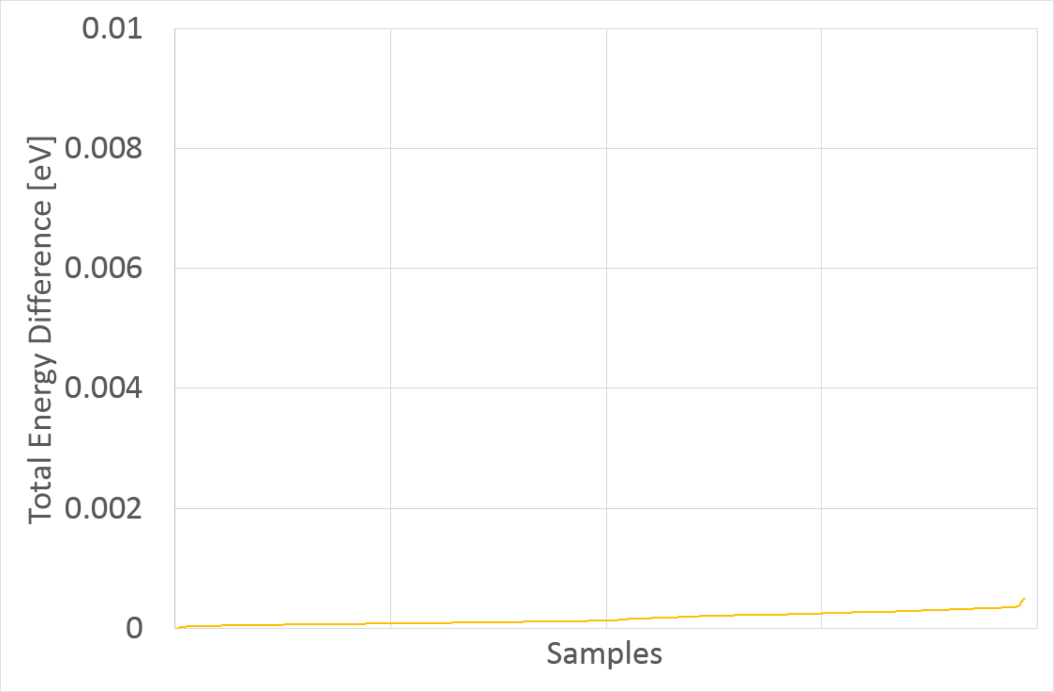

e)

**Figure 3.3.** Energy evolution of: e) $Cu_7$ (yellow line). For each size, the first region is the ground state structure and energies from region II onwards are associated to new isomers. (Cont.)

As mentioned in the methodology section, a thousand samples were generated randomly for each cluster size. However, due to the type of system we are dealing with, several isomers can be formed and we needed to be sure that any given structure found was a real isomer. For each type of structure, that are the regions labeled as I, II, III, etc. on figure 3.3, the energy difference inside the regions is close to zero, producing almost flat lines and the lengths of these lines tell us the proportion of the total samples that were generated randomly and that converged into a particular type of structure. For cluster-sizes where more than one stable structure was found, we obtained a figure that looks like a staircase function, in which we are able to see the energy differences between the different isomers. For each energy region we selected the best cluster's structure, which was the one with the lowest energy among all the samples inside that particular region. We found one isomer for $Cu_3$ and $Cu_4$ and three for $Cu_6$. Those structures are shown in figure 3.4.

$Cu_3$ – Ground State

$Cu_3$ – 1st Isomer

$Cu_4$ – Ground State

$Cu_4$ – 1st Isomer

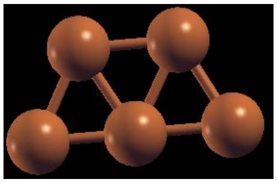

$Cu_5$ – Ground State

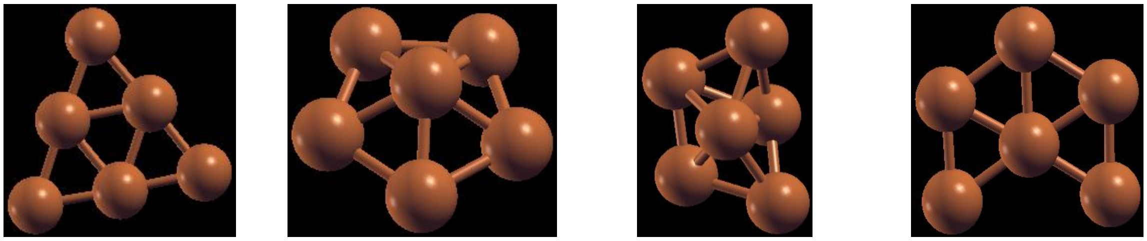

$Cu_6$ – Ground State

$Cu_6$ – 1st Isomer

$Cu_6$ – 2nd Isomer

$Cu_6$ – 3rd Isomer

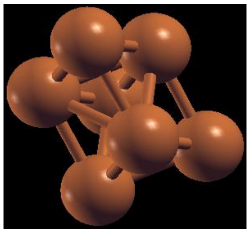

$Cu_7$ – Ground State

**Figure 3.4.** Structures found for $Cu_3$, $Cu_4$, $Cu_5$, $Cu_6$ and $Cu_7$.

Finally, the binding energy per atom ($B_E$) and the difference in binding energy per atoms ($\Delta E$) of the ground state structures and different isomers of copper clusters are calculated as follows:

$$B_E(n) = \frac{nE_1 - E_n}{n}$$

$$\Delta E = B_E(n) - \widetilde{B_E}(n)$$

Where $E_1$ is the energy of one copper atom, which value was -121.121669 Ry, $E_n$ is the total energy of the Cu$_n$ cluster, and finally $B_E(n)$ and $\widetilde{B_E}(n)$ are the binding energy of the ground state and subsequent isomers of the system, respectively. The calculated values are detailed in table 3.5.

**Table3.5.** Binding energy (B$_E$) and difference in binding energy ($\Delta$E) of ground state an isomers of Cu$_n$ (n=3-7)

| | **B$_E$ [eV/atom]** | **$\Delta$E [eV/atom]** |
|---|---|---|
| **Cu$_3$** | 1.436 | 0.000 |
| | 1.404 | 0.032 |
| **Cu$_4$** | 1.851 | 0.000 |
| | 1.756 | 0.095 |
| **Cu$_5$** | 1.964 | 0.000 |
| **Cu$_6$** | 2.178 | 0.000 |
| | 2.153 | 0.024 |
| | 2.136 | 0.042 |
| | 2.128 | 0.050 |
| **Cu$_7$** | 2.246 | 0.000 |

## DISCUSSION AND CONCLUSIONS

### Geometry of ground state and isomers structures

For the Cu$_3$ cluster we found two structures: the most stable was a planar triangle as reported by all the references studied. Also we found and isomer which is not consistent with Kabir *et al.* [25] findings: they found a structure where two copper atoms are bonded to a central atom forming a straight line, while we found a similar structure, but the angle formed by those atoms is not 180°, but 124.116°.

In the case of $Cu_4$ cluster, our calculations predicted a planar rhombus as the most stable structure for this configuration. Also, we found one isomer with the shape of an isosceles triangle with an atom connected to the vertex of the two equal edges. This result is consistent with the findings of references [23], [25] and [27]. The larger angle of the rhombus for our study was $122.949^{a}$, which is in good agreement with the 120° degrees reported by Kabir *et al.* [25] and the predicted by Calaminici *et al.* which was 123° [34].

For the $Cu_5$ cluster, we found only the ground state structure, which is also the most stable structure reported by Kabir *et al.* [25] and Li *et al.* [27]. In our calculations, we found that the trigonal bi-pyramid reported as a ground state structure by Böyükata and Belchior and as an isomer by reference [25], was unstable and relaxed into the $C_{2v}$ structure. This behavior was also observed for the tetrahedron reported in references [25] and [28] for the $Cu_4$, which relaxed into the planar rhombus in our study.

In the case of $Cu_6$ cluster, we found four different structures: the ground state structure and the first isomer were reported in the same sequence by Li *et al.* [27], but they did not report more isomers for this configuration. Massobrio *et al.* [23] and Kabir *et al.* [25] agreed by proposing the capped trigonal pentagon as the most stable structure, while our calculations show that it is the second best structure. Furthermore, Massobrio *et al.* proposed and intermediate structure before the flat structure that is our ground state configuration, while Kabir *et al.* and Böyükata and Belchior [28] didn't report any planar structure for this cluster.

Finally, for the $Cu_7$ cluster we found one structure which agrees again with the structure reported by Li et al. Our result differs with the ground state and isomers reported by references [25] and [28].

## Binding energies

Among all the structures found in our calculations, we now consider only the structures with the highest binding energy, which correspond to the ground state structure. As the cluster size increases, it was observed that the binding energy per atom also increases. In figure 3.5 we compared our results with several reports: theoretical works used Density Functional Theory with

Local Density Approximation [23], Tight Binding [25], Real Space Pseudopotentials constructed within Local Density Approximation [27] and Molecular Dynamics [28]. Experimentally, the binding energies of clusters were derived from Collision-Induced Dissociation [21] [22].

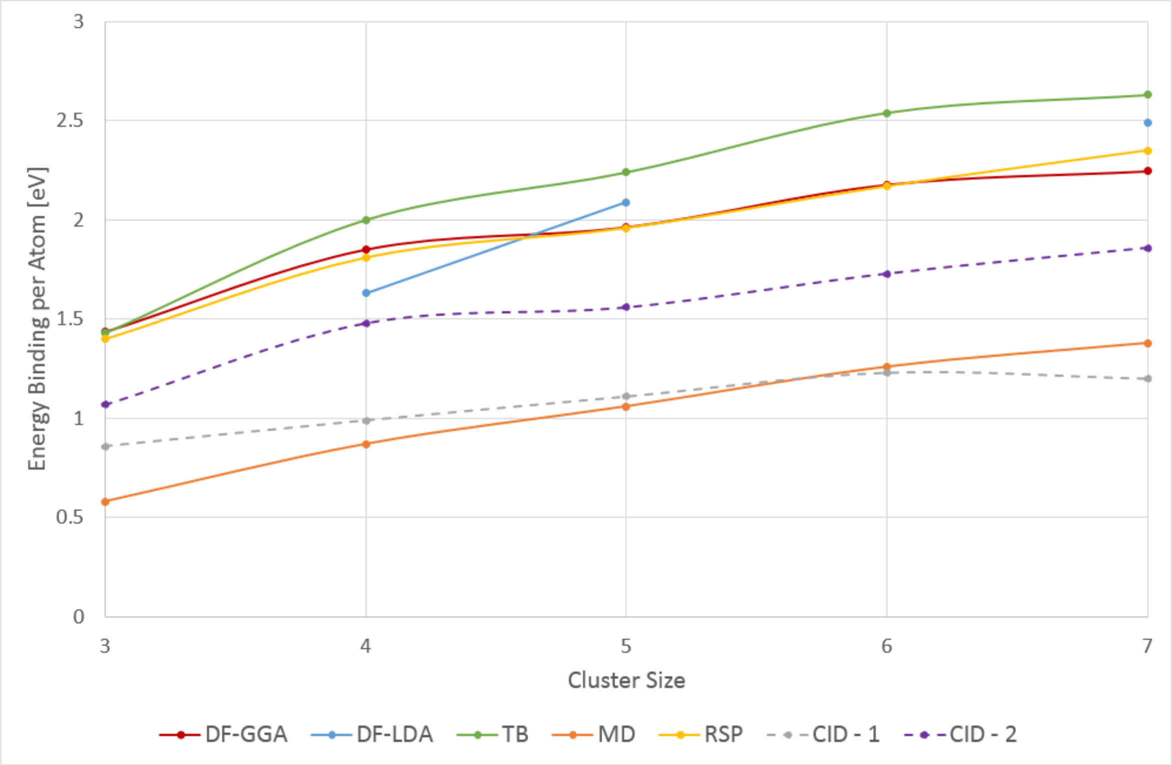

**Figure 3.5.** Comparison of binding energy per atom as a function of cluster size, among: our results using DF-GGA (red), DF-LDA [23] (blue), TB [25] (green), Real Space Pseudopotential [27] (yellow), MD [28] (orange) and two CID experiments [21] [22] (dashed lines grey and violet).

The experimental data obtained by Ingólfsson *et al.* [21] and Spasov *et al.* [22] was lower that our findings, as expected, given the tendency of the approximation used here to overestimate the binding energies. We found that our binding energies are very similar to the reported by Li et al. [27]. The same growing tendency was observed by Kabir *et al.* [25] but they also recognized that their energies are overestimated. Binding energies reported by Böyükata and Belchior [28] are ~1 eV below to the reported by us, this was expected due to instability of the structures that they reported as ground states and their tendency to relax into other structures when we performed relaxation calculations to those structures, as was mentioned before.

## HOMO-LUMO Gap

A way to determine the stability of the cluster is the highest occupied – lowest occupied molecular level (HOMO – LUMO) gap energy. The calculated HOMO – LUMO gap energies are plotted in figure 3.6.

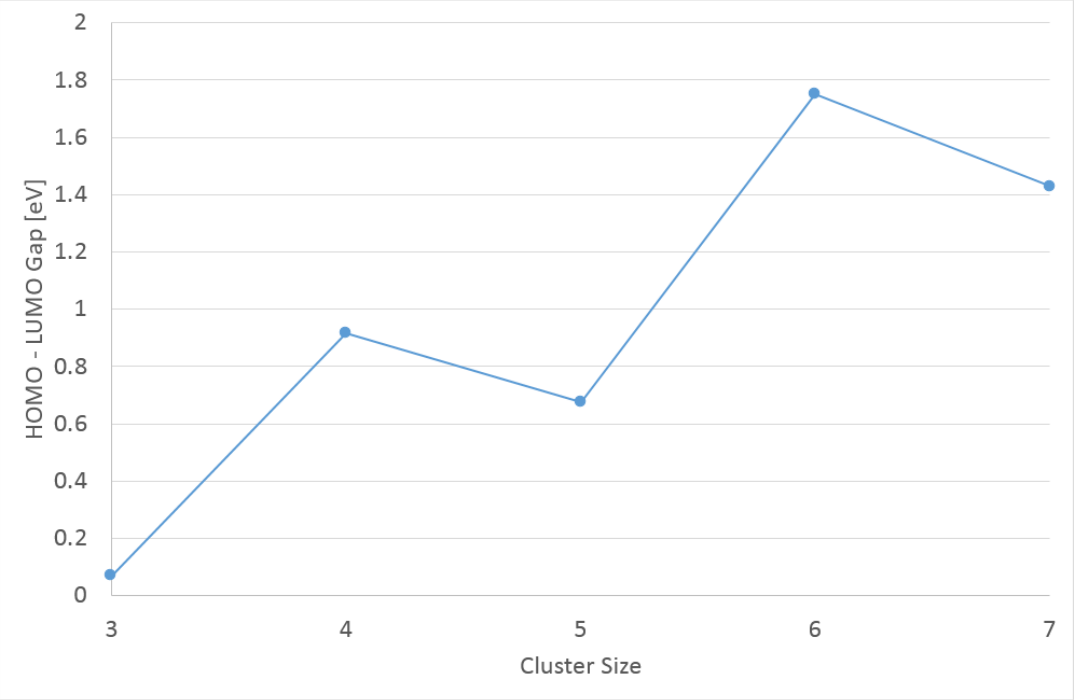

**Figure 3.6.** Evolution of the highest occupied – lowest occupied (HOMO – LUMO) gap energy as the cluster size increases.

An odd – even alternation was observed and this is result of the electron pairing effect: odd (even) sized clusters have HOMO which is singly (doubly) occupied. Therefore even numbered $Cu_n$ clusters show relatively higher energy. In our study we did not find particularly large HOMO – LUMO gap given the cluster sizes analyzed, but this behavior is expected for $Cu_2$ and $Cu_8$ due to electronic shell closing. DFT is not particularly accurate for determining energy band gaps. A more accurate approach will be required in the future in order to find more reliable values for the band gaps and discuss their possible alignments with a wide variety of semiconductors, which would make it possible to think about using Cu clusters in order to avoid fast recombination of e-h pairs in semiconductors.

## REFERENCES

[1] R. L. Johnston, Atomic and molecular clusters, London: Taylor & Francis, 2002.

[2] W. D. Knight, K. Clemenger, W. A. de Heer, W. A. Saunders, M. Y. Chou and M. L. Cohen, "Electronic Shell Structure and Abundances of Sodium Clusters," *Physical Review Letters,* vol. 52, no. 24, pp. 2141 - 2143, 1984.

[3] I. Katakuse, T. Ichihara, Y. Fujita, T. Matsuo, T. Sakurai and H. Matsuda, "Mass distributions of negative cluster ions of copper, silver, and gold," *International Journal of Mass Spectrometry and Ion Processes,* vol. 74, no. 1, pp. 33 - 41, 1986.

[4] N. Vilar Vidal, *Synthesis, Characterization and Properties of Copper Clusters,* Santiago de Compostela: Ph. D. Dissertation, 2012.

[5] N. W. Ashcroft and N. D. Mermin, Solid State Physics, Harcourt College Publishers, 1976.

[6] C. Binns, "Nanoclusters deposited on surfaces," *Surface Science Reports,* vol. 44, no. 1 - 2, pp. 1 - 49, 2001.

[7] S. J. Park, T. A. Taton and C. A. Mirkin, "Nanoparticle Probes," *Science,* vol. 295, no. 5559, pp. 1503 - 1506, 2002.

[8] D. I. Gittins, D. Bethell, D. J. Schiffrin and R. J. Nichols, "A nanometre-scale electronic switch consisting of a metal cluster and redox-addressable groups," *Nature,* vol. 408, no. 6808, pp. 67 - 69, 2000.

[9] M. Valden, X. Lai and D. W. Goodman, "Onset of Catalytic Activity of Gold Clusters on Titania with the Appearance of Nonmetallic Properties," *Science,* vol. 281, no. 5383, pp. 1647 - 1650, 1998.

[10] M. B. Knickelbein, "Reactions of transition metal clusters with small molecules," *Annual Review of Physical Chemistry,* vol. 50, pp. 79 - 115, 1999.

[11] S. H. Joo, S. J. Choi, I. Oh, J. Kwak, Z. Liu, O. Teresaki and R. Ryoo, "Ordered nanoporous arrays of carbon supporting high dispersions of platinum nanoparticles," *Nature,* vol. 412, no. 6843, pp. 169 - 172, 2001.

[12] P. L. Hansen, J. B. Wagner, S. Helveg, J. R. Rostrup-Nielsen, B. S. Clausen and H. Topsøe, "Atom-resolved imaging of dynamic shape changes in supported copper nanocrystals,"

*Science,* vol. 295, no. 5562, pp. 2053 - 2055, 2002.

[13] J. Tiggesbäumker, L. Köller, K.-H. Meiwes-Broer and A. Liebsch, "Blue shift of the Mie plasma frequency in Ag clusters and particles," *Physical Review A,* vol. 48, no. 3, pp. R1749 - R1752, 1993.

[14] G. Apai, J. F. Hamilton, J. Stohr and A. Tompson, "Extended X-Ray—Absorption Fine Structure of Small Cu and Ni Clusters: Binding-Energy and Bond-Length Changes with Cluster Size," *Physical Review Letters,* vol. 43, no. 2, pp. 165 - 169, 1979.

[15] A. Balerna, E. Bernieri, P. Picozzi, A. Reale, S. Santucci, E. Burattini and S. Mobilio, "A structural investigation on small gold clusters by EXAFS," *Surface Science,* vol. 156, no. 1, pp. 206 - 213, 1985.

[16] P. A. Montano, H. Purdum, G. K. Shenoy, T. I. Morrison and W. Schulze, "X-ray absorption fine structure study of small metal clusters isolated in rare-gas solids," *Surface Science,* vol. 156, no. 1, pp. 228 - 233, 1985.

[17] N. Vilar-Vidal, J. Rivas, L and M. A. López-Quintela, "Size Dependent Catalytic Activity of Reusable Subnanometer Copper(0) Clusters," *ACS Catalysis,* vol. 2, no. 8, pp. 1693 - 1697, 2012.

[18] J. A. Howard, R. Sutcliffe and J. S. Tse, "ESR spectrum of Cu5, a trigonal bipyramidal copper cluster," *Chemical Physics Letters,* vol. 94, no. 6, pp. 561 - 564, 1983.

[19] J. Ho, K. M. Ervn and W. C. Lineberger, "Photoelectron spectroscopy of metal cluster anions: Cu− n , Ag− n , and Au− n," *Journal of Chemical Physics,* vol. 93, no. 10, pp. 6987 - 7002, 1990.

[20] K. J. Taylor, C. L. Pettiette--Hall, O. Cheshnovsky and R. E. Smalley, "Ultraviolet photoelectron spectra of coinage metal clusters," *Journal of Chemical Physics,* vol. 96, no. 4, pp. 3319 - 3329, 1992.

[21] O. Ingólfsson, B. Ulrike and S. Ko-ichi, "Energy-resolved collision-induced dissociation of Cun+ (n=2-9): Stability and fragmentation pathways," *Journal of Chemical Physics,* vol. 112, no. 10, pp. 4613 - 4620, 2000.

[22] V. A. Spasov, T.-H. Lee and K. M. Ervin, "Threshold collision-induced dissociation of anionic copper clusters and copper cluster monocarbonyls," *Journal of Chemical Physics,* vol. 112, no. 4, pp. 1713 - 1720, 2000.

[23] C. Massobrio, A. Pasquarello and R. Car, "Structural and electronic properties of small

copper clusters: a first principles study," *Chemical Physics Letters,* vol. 238, no. 4 - 6, pp. 215 - 221, 1995.

[24] M. Kabir, A. Mookerjee, A. Banerjea and A. K. Bhattacharya, "Study of small metallic nanoparticles: an Ab-Initio Full-Potential Muffin-Tin Orbitals based Molecular Dynamics study of small Cu clusters," *International Journal of Modern Physics B,* vol. 17, no. 10, pp. 2061 - 2075, 2003.

[25] M. Kabir, A. Mookerjee and A. K. Bhattacharya, "Structure and stability of copper clusters: A tight-binding molecular dynamics study," *Physical Review A,* vol. 69, no. 4, p. 043203, 2004.

[26] H. Aakeby, I. Panas, L. G. M. Petterson, P. Siegbahn and U. Wahlgren, "Electronic and geometric structure of the copper (Cun) cluster anions (n ≤ 10)," *Journal of Physical Chemistry,* vol. 94, no. 14, pp. 5471 - 5477, 1990.

[27] S. Li, M. M. G. Alemany and J. R. Chelikowsky, "Real space pseudopotential calculations for copper clusters," *Journal of Chemical Physics,* vol. 125, no. 3, p. 034311, 2006.

[28] M. Böyükata and J. C. Belchior, "Structural and Energetic Analysis of Copper Clusters: MD Study of Cun (n = 2 -45)," *Journal of the Brazilian Chemical Society,* vol. 19, no. 5, pp. 884 - 893, 2008.

[29] R. H. Petrucci, F. G. Herring, J. D. Madura and C. Bissonnette, General Chemistry: Principles and Modern Applications, Pearson Prentice Hall, 2010.

[30] P. Giannozzi, S. Baroni, N. Bonini, M. Calandra, R. Car, C. Cavazzoni, D. Ceresoli, G. L. Chiarotti, M. Cococcioni, I. Dabo, A. Dal Corso, S. de Gironcoli, S. Fabris, G. Fratesi, R. Gebauer, U. Gerstmann, C. Gougoussis, A. Kokalj, M. Lazzeri, L. Martin-Samos, C. Sbraccia, S. Scandolo, G. Sclauzero, A. P. Seitsonen, A. Smogunov, P. Umari and R. M. Wentzcovitch, "QUANTUM ESPRESSO: a modular and open-source software project for quantum simulations of materials," *Journal of Physics: Condensed Matter,* vol. 21, no. 39, p. 395502, 2009.

[31] J. P. Perdew, K. Burke and M. Enrzerhof, "Generalized Gradient Approximation Made Simple," *Physical Review Letters,* vol. 77, no. 18, pp. 3865 - 3868, 1996.

[32] H. J. Monkhorst and J. D. Pack, "Special points for Brillouin-zone integrations," *Physical Review B,* vol. 13, no. 12, pp. 5188 - 5192, 1976.

[33] G. Makov and M. C. Payne, "Periodic boundary conditions in ab initio calculations," *Physical*

*Review B,* vol. 51, no. 7, pp. 4014 - 4022, 1995.

[34] P. Calamanici, A. M. Köster, N. Russo and D. R. Salahub, "A density functional study of small copper clusters: Cu n (n⩽5)," *Journal of Chemical Physics,* vol. 105, no. 21, pp. 9546 - 9556, 1996.

[35] H. T. Stokes and D. M. Hatch, "FINDSYM: program for identifying the space-group symmetry of a crystal," *Journal of Applied Crystallography,* vol. 38, no. 1, pp. 237 - 238, 2005.

# Closing Remarks

We have shown with this work, that using ab-initio DFT methods with a random search algorithm is a very accessible, yet powerful way to address the crystal structure prediction problem. We used this conjunction of methods in two cases of different areas of physics: a molecular system submitted to a very high pressure, and a copper cluster system in vacuum.

The random sampling approach required us to relax a large number of initial samples on both cases. One thousand samples were generated each time taking into account several constraints that depended on the specifics features of the studied system. Having that in mind, we were able to make random structures in a systematic way which included some restrictions in order to avoid generating non-physical structures. For instance, in the case of solid oxygen we avoided needle-like cell structures, by restricting the cell angles, and for copper clusters we placed the initial atomic positions in a pre-defined volume in order to concentrate the atoms at the center of the unit-cell, thus keeping the system isolated. We also took care of avoiding the random generation of overlapping atoms, which can cause the DFT calculation to crash.

The large populations sizes (N=1000) that are required in order to have a proper sampling of the configurations space and the fact that the forces were calculated using DFT, imply that in principle these calculations tend to take a very long time for large systems; this is the reason why we are only advising the use of this tool in cases with a few degrees of freedom, where it is very effective. However, by dividing the relaxation procedure into two, we made a trade between computing time and accuracy: the first one is a loose calculation, where we wanted to reach quickly into a structure which is closer to the final one, while the second calculation is much more accurate, meaning that the computing time might increase, but by starting from a structure that is already relaxed, the computing resources are optimized. Thus, we obtained accurate final structures in a very reasonable time.

For systems in which it is very important to find the relative positions of atoms, this approach is ideal and it has two major advantages: the first one, is due to its simplicity, we showed that this methodology can be easily applied to different types of physical systems dealing with very diverse problems, therefore is expected that this method can and will make an impact in various branches of science, because it allows us to explore and characterize physical systems and compare directly with experimental results, as well as study those that are beyond of our experimental limits. The second advantage is that the available computer resources can be used in an efficient while still keeping a final good accuracy in our findings. From here we could proceed in two ways: we can work on much larger systems generating enormous databases that can be further analyzed by using data mining techniques, or we can keep dealing with small systems running the DFT calculations in our laptops, relatively fast, thanks to the methodology implemented here.

# Appendix A

## DIRAC'S NOTATION AND SECOND QUANTIZATION

In the Dirac's bra-ket notation, a given many-body state function is represented by a state vector $|\Phi\rangle$, which real-state form can be obtained by projecting it onto the vector $\langle \boldsymbol{r}|$, for instance: $\langle \boldsymbol{r}|\Phi\rangle = \Phi(\boldsymbol{r})$. Therefore, the expectation value of an operator $\hat{A}$ in a state $|\Phi\rangle$ is given by:

$$\langle\Phi|\hat{A}|\Phi\rangle = \int \Phi^*(\boldsymbol{r})\hat{A}\Phi(\boldsymbol{r})d\boldsymbol{r} \quad (A.1)$$

Where the integral is a 3N-dimensional one in the electronic variables **r**.

So far, we only have experimental evidence that in nature there are just two types of particles: bosons and fermions, which states are completely symmetric and anti-symmetric, respectively. Their symmetries are closely related to their spins: bosons' spins have integer values, while fermions have half-integer spin value, such as electrons that are spin $1/2$ particles.

Inside the quantum many-body theory, we will consider a non-relativistic system made of a very large number of indistinguishable fermions, and in order to represent this system, the formalism known as Second Quantization was developed. This formalism is constructed within the Fock Space and in this scheme the creation and annihilation operators[1] are introduced:

$$a_i^\dagger = |\dots, n_i, \dots\rangle = (1 - n_i)(-1)^{\sum_{j<i} n_j}|\dots, n_i + 1, \dots\rangle \quad (A.2.a)$$

---

[1] The operators defined are for fermions. The creation and annihilation operators for bosons are slightly different.

$$a_i = |\dots, n_i, \dots\rangle = n_i(-1)^{\sum_{j<i} n_j}|\dots, n_i - 1, \dots\rangle \qquad (A.2.b)$$

These operators increase or decrease the occupation number of the state $|i\rangle$ by one. Also, in the case of fermions, the definition of the operator has to take into account the Pauli Exclusion Principle, which establishes that two identical fermions must not occupy the same state.

Once we have set the creation and annihilation operators for fermions, we can define the one- and two-body density matrices, which are related with the creation and annihilation of one or two electrons at different positions of the space, and are defined as follows:

$$\rho_1(\boldsymbol{r}, \boldsymbol{r}') = \sum_{\sigma} \langle \Phi | \hat{\psi}_\sigma^\dagger(\boldsymbol{r}) \hat{\psi}_\sigma(\boldsymbol{r}') | \Phi \rangle \qquad (A.3.a)$$

$$\rho_2(\boldsymbol{r}, \boldsymbol{r}') = \frac{1}{2} \sum_{\sigma,\sigma\prime} \langle \Phi | \hat{\psi}_\sigma^\dagger(\boldsymbol{r}) \hat{\psi}_{\sigma\prime}^\dagger(\boldsymbol{r}') \hat{\psi}_{\sigma\prime}(\boldsymbol{r}') \hat{\psi}_\sigma(\boldsymbol{r}) | \Phi \rangle \quad (A.3.b)$$

Where the field operators $\hat{\psi}_\sigma^\dagger(\boldsymbol{r})$ and $\widehat{\psi}_\sigma(\boldsymbol{r}')$, creates and annihilates an electron of spin $\sigma$ in the position eigenstate $|\boldsymbol{r}\rangle$. They are defined by:

$$\hat{\psi}_\sigma^\dagger(\boldsymbol{r}) = \sum_i \varphi_{i,\sigma}^*(\boldsymbol{r}) a_i^\dagger \quad (A.4.a)$$

$$\hat{\psi}_\sigma(\boldsymbol{r}) = \sum_i \varphi_{i,\sigma}(\boldsymbol{r}) a_i \quad (A.4.b)$$

These operators obey the following commutation relations:

$$\left[\hat{\psi}_\sigma(\boldsymbol{r}), \hat{\psi}_{\sigma'}(\boldsymbol{r}')\right]_\pm = 0 \qquad (A.5.a)$$

$$\left[\hat{\psi}_\sigma^\dagger(\boldsymbol{r}), \hat{\psi}_{\sigma'}^\dagger(\boldsymbol{r}')\right]_\pm = 0 \qquad (A.5.b)$$

$$\left[\hat{\psi}_\sigma(\boldsymbol{r}), \hat{\psi}_{\sigma'}^\dagger(\boldsymbol{r}')\right]_\pm = \delta_{\sigma\sigma'} \delta^{(3)}(\boldsymbol{r} - \boldsymbol{r}') \quad (A.5.c)$$

The upper sign apply for fermions, and the lower one, not used here, is for bosons.

Finally, we can define the two-body direct correlation function $g(\boldsymbol{r},\boldsymbol{r}')$ as follows:

$$\rho_2(\boldsymbol{r},\boldsymbol{r}') = \frac{1}{2}\rho_1(\boldsymbol{r},\boldsymbol{r})\rho_1(\boldsymbol{r}',\boldsymbol{r}')g(\boldsymbol{r},\boldsymbol{r}')$$

$$\rho_2(\boldsymbol{r},\boldsymbol{r}') = \frac{1}{2}\rho(\boldsymbol{r})\rho(\boldsymbol{r}')g(\boldsymbol{r},\boldsymbol{r}') \quad (A.6)$$

Where $\rho(\boldsymbol{r})$ and $\rho(\boldsymbol{r}')$ are the diagonal elements of $\rho_1(\boldsymbol{r},\boldsymbol{r})$ and $\rho_1(\boldsymbol{r}',\boldsymbol{r}')$, respectively and represent the electronic density.